MODELLING AND EXPERIMENTAL STUDY OF TITANOSILICATE ETS-10: APPLICATION FOR SOLAR CELLS

A THESIS SUBMITTED TO
THE GRADUATE SCHOOL OF NATURAL AND APPLIED SCIENCES
OF
MIDDLE EAST TECHNICAL UNIVERSITY

MEHMET KOÇ

IN PARTIAL FULFILLMENT OF THE REQUIREMENTS
FOR
THE DEGREE OF MASTER OF SCIENCE
IN
MICRO AND NANOTECHNOLOGY

AUGUST 2013

Approval of the thesis:

MODELLING AND EXPERIMENTAL STUDY OF TITANOSILICATE ETS-10: APPLICATION FOR SOLAR CELLS

submitted by **MEHMET KOÇ** in partial fulfillment of the requirements for the degree of **Master of Science in Micro and Nanotechnology Department, Middle East Technical University** by,

Prof. Canan Özgen
Dean, Graduate School of **Natural and Applied Sciences**

Prof. Tayfun Akın
Head of Department, **Micro and Nanotechnology**

Assoc. Prof. Burcu Akata Kurç
Supervisor, **Micro and Nanotechnology**

Assoc. Prof. Hande Toffoli
Co-supervisor, **Physics**

Examining Committee Members:

Prof. Macit Özenbaş
Materials Engineering and Metallurgy Department, METU

Assoc. Prof. Burcu Akata Kurç
Micro and Nanotechnology Department, METU

Assoc. Prof. Hande Toffoli
Physics Department, METU

Prof. Hayrettin Yücel
Central Laboratory, METU

Assist. Prof. Yunus Eren Kalay
Materials Engineering and Metallurgy Department, METU

Date:

I hereby declare that all information in this document has been obtained and presented in accordance with academic rules and ethical conduct. I also declare that, as required by these rules and conduct, I have fully cited and referenced all material and results that are not original to this work.

Name, Last Name: MEHMET KOÇ

Signature :

ABSTRACT

MODELLING AND EXPERIMENTAL STUDY OF TITANOSILICATE ETS-10: APPLICATION FOR SOLAR CELLS

Koç, Mehmet
M.S., Department of Micro and Nanotechnology
Supervisor : Assoc. Prof. Burcu Akata Kurç
Co-Supervisor : Assoc. Prof. Hande Toffoli

August 2013, 133 pages

Density functional theory (DFT) calculations within the gradient-corrected approximation (GGA) have been carried out on three models of ETS-10 with the aim to elucidate the effect of ion exchange on the structural, electronic and vibrational properties of the Ti–O–Ti quantum wire. Our data are reveal the presence of two inequivalent Ti–O bonds along the chain in the ETS-10 sodium form, in agreement with past theoretical and experimental studies. The nature and spectral position of the ligand-to-metal charge transfer transition experimentally observed at 4.02 eV is also well accounted for by our DFT calculations. Partial and full exchange of Na^+ cations with alkaline, earth-alkaline and transition metal ions affect both structural, electronic and vibrational properties of the quantum wire. The theoretical results have been rationalized and compared with recent experimental data.

In order to clarify the theoretical data revealed from DFT studies, experimental setup was arranged. Experimental data show significant similarities with simulation results. Effect of ion-exchange at ETS-10 was discussed both experimentally and theoretically. Effects of different cations with very broad range of physical properties were discussed. In the guidance of theoretical and experimental analyses, solar cell studies were discussed. Important variances in the application part, which is very challenging to explain experimentally, was tried to reveal. Theoretical studies and solar cell results reveal that ETS-10 has a tunable band gap with ion exchange process, while charge cycle of ETS-10 in DSSC geometry should be improved.

Keywords: ETS-10, ion exchange, DSSC, solar cell, dye, DFT, solid modelling, nanoparticle, nanowire, zeolite

ÖZ

MODELLEME VE DENEYSEL OLARAK TİTANOSİLİKAT ETS-10 ARAŞTIRMASI: GÜNEŞ PİLLERİ UYGULAMALARI ARAŞTIRMALARI

Koç, Mehmet
Yüksek Lisans, Mikro ve Nanoteknoloji Bölümü
Tez Yöneticisi : Doç. Dr. Burcu Akata Kurç
Ortak Tez Yöneticisi : Doç. Dr. Hande Toffoli

Ağustos 2013 , 133 sayfa

Bu tezde Titanosilikat ETS-10'in üç farklı model ile yoğunluk fonksiyoneli teorisi kullanılarak, GGA(gradient-corrected approximation) yaklaşımı ile iyon değişiminin Ti–O–Ti kuantum zincirleri üzerindeki yapısal, elektroniksel ve vibrasyonel etkisi araştırılmıştır. Sonuçlar ETS-10'in sodyumlu formunda tek-atomluk titanyumoksit zincirlerinde iki eşit olmayan Ti–O bağının varlığına işaret ediyor, literatürdeki deneysel ve teorik çalışmalarla örtüşür bir biçimde. Deneysel olarak gözlemlenmiş olan 4.02 eV'lik bant yapısı ve ligand-metal yük transferinin yapısı ve spektrali DFT hesaplarıyla da gösterilmiştir. Na^+ atomlarının alkali, toprak-alkali ve geçiş metalleriyle kısmi ve tamamen değişimi kuantum zincirlerinin fiziksel yapısını, elektronik yapısını ve vibrasyonel yapısını etkilemektedir. Teorik sonuçlar incelendi ve mevcut deneysel çalışmalarla karşılaştırıldı.

DFT sonuçlarının destekleyici kanıtlarla sağlanması için deneyler gerçekleştirildi. Deneysel sonuçlar simulasyonlarla ciddi benzerlikler gösterdi. İyon değişiminin deneysel ve teorik etkisi tartışıldı. Farklı katyonların ETS-10 üzerindeki her türlü fiziksel etkisi geniş kapsamlı olarak incelendi. Elde edilen deneysel ve teorik bilgi ışığında güneş enerjisi araştırmaları gerçekleştirildi. Uygulama kısmındaki deneysel olarak açıklaması çok zor olan bir takım önemli değişimler teorik olarak tartışıldı. Teorik çalışmalar ve güneş enerjisi araştırmaları göstermektedir ki ETS-10 iyon değişimi ile değiştirilebilir bant yapısına sahiptir bunun yanında ETS-10 ile oluşturulmuş boya duyarlı güneş hücrelerindeki yük döngüsünün geliştirilmesi gerekmektedir.

Anahtar Kelimeler: ETS-10, iyon değişimi, boya duyarlı güneş hücresi, güneş hücresi, boya, DFT, katı modelleme, nanoparçacık, nanotel, zeolit

In the most Merciful and the most Generous name of God

ACKNOWLEDGMENTS

I am very grateful to my supervisor Assoc. Prof Burcu Akata Kurç for her guidance and support during my study, and her great attention and patience in the every step of my study.

I am very thankful to my co-supervisor Assoc. Prof. Hande Toffoli for her great attention and guidance during this work.

It is a great pleasure to thank Prof. Macit Özenbaş from Materials Engineering and Metallurgy Department, METU.

I am very grateful to my colleagues Salih Kaan Kirdeciler, Sezin Galioğlu, Melda İşler and Kerem Çağatay İçli.

I want to thank to Prof. Hayrettin Yücel and METU Central Laboratory for their great opportunities during every analysis and in this work.

I am very thankful to TÜBİTAK ULAKBİM for their great research opportunities during this work.

I want to thank GÜNAM METU for their contributions to solar cell studies of this work.

I am very grateful to Assoc. Prof. Danielle Toffoli for his contributions to my study.

I want to thank Assoc. Prof. Yunus Eren Kalay for his guidance in cooperative studies during this work.

Finally, I want to thank to my family for every stage of my life.

TABLE OF CONTENTS

CHAPTERS

APPENDICES

LIST OF TABLES

TABLES

LIST OF FIGURES

FIGURES

LIST OF ABBREVIATIONS

A	An abbreviation
AA	Another abbreviation
LONGESTABBRV	Longest Abbreviation is used to balance the columns of list of abbreviations

CHAPTER 1

INTRODUCTION

1.1 Material

1.1.1 Zeolite

Zeolites are crystalline inorganic aluminasilicates that are also known as molecular sieves. They have interconnected building units of AlO_4 or SiO_4 tetrahedra, which creates 3-dimensional (3D) frameworks with linked channel systems and well-defined micropores Fig. 1.1 [Adapted from [1], [2]]. Zeolites have high surface area due to their microporosity. The database of the International Zeolite Association (IZA) gives structural information and crystallographic data of more than 170 framework types [3]. So far, about 17 of these structures such as zeolite A, beta, X, Y have been determined to be of commercial interest [3].

The chemical composition of a zeolite is important to define its unique properties. Usually, the following sum formula is given [4].

$$M^{m+}_{\frac{y}{m}}[(SiO_2)_x \cdot (AlO_2^-)_y] \cdot zH_2O \tag{1.1}$$

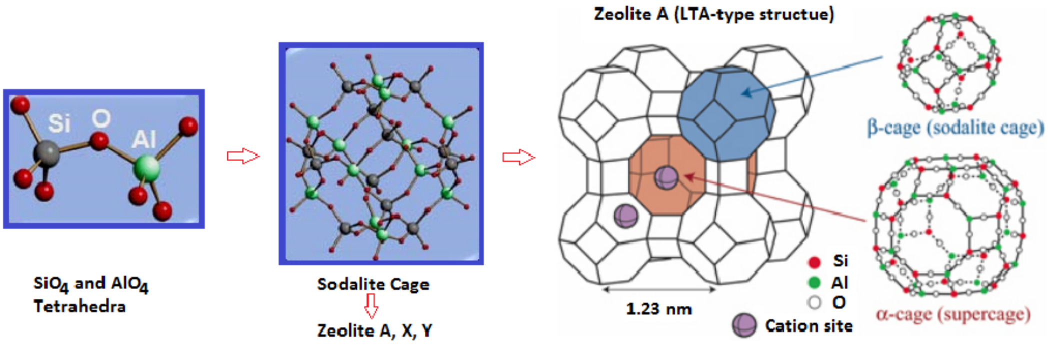

Figure 1.1: Zeolite framework structure.

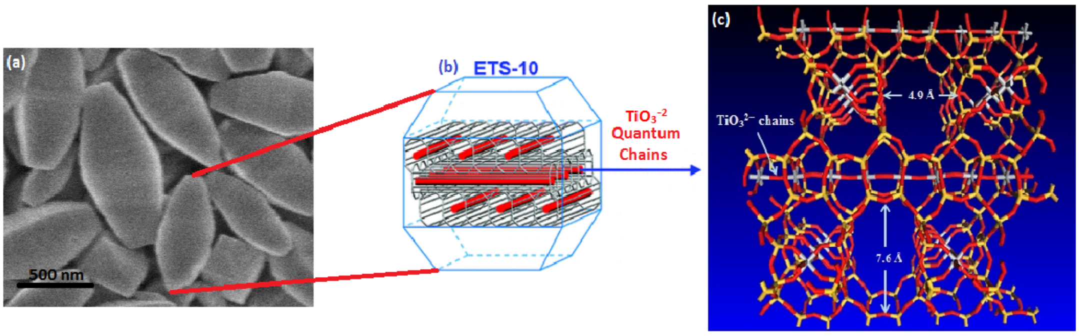

Figure 1.2: (a) SEM image of truncated ETS-10 crystals, (b) illustration of quantum wires in ETS-10 crystals , (c) structural illustration of ETS-10.

where, M denotes a cation with charge m.
Each tetrahedrally coordinated aluminum Al^{3+} gives a negative charge to the framework as can be seen in Eq. 1.1. For neutralization, this charge is compensated by y/m cations M^{m+}, which are called extra framework cations. These cations are electrostatically bound to the framework and mobile along the channels [5]. Consequently, zeolites are excellent ion exchangers. Moreover, zeolites are used in several chemical reactions as a catalyst since the aluminum ions act as highly acidic sites. The content of mobile cations and the amount of acidic centers per unit cell is defined by silicon to aluminum ratio (i.e., x/y). Zeolites have superior intrinsic properties; additionally, they can be modified in a post synthesis step, i.e., ion exchange, by incorporating metal ions such as Ag, Au, Pt, Fe, or Cu. Due to their unique properties zeolites are used in numerous industrial applications such as ion exchangers for water purification [6, 7], molecular sieves and separation membranes [8–11], absorbents for organic vapors [12], or catalyst beds in the petrochemical industry or in the synthesis of several chemicals [13–15].

1.1.2 Zeo-Type Materials: Titanosilicate

Zeo-type materials are similar to zeolites but different in the sense that the AlO_4 units are replaced with TiO_6 (i.e. titanosilicates). Engelhard titanosilicate (ETS-10) is a synthetic microporous crystalline material, which contains building units of corner-sharing TiO_6 octahedra and SiO_4 tetrahedra linked through bridging oxygen atoms with pore dimensions of 4.9 and 7.6 Å as shown in Fig. 1.2 [16, 17]. These building units are exceptionally organized to form -Ti-O-Ti- chains with the estimated diameter of around 0.67 nm running through the [110] and [110] directions in the crystal Fig. (1.2 b [18] and c (Adapted from [19])). These chains are surrounded with a silica matrix [17], and considered as a 1-D quantum-confined form of titania with a band gap energy, which was revealed to be related to the size of the ETS-10 crystals along [110] direction [18].

Each ETS-10 has a stoichiometry of $(Na,K)_2TiSi_5O_{13}$. TiO_3^{-2} unit include two negative charges each, similar to zeolite crystals for neutralization that are compensated by extra framework charge-balancing cations Na^+ and K^+ in the as-synthesized materials [16]. ETS-10 has high ion-exchange capacity with respect to other zeolites, and it has unique monatomic, orthogonal, linear, non-intersecting, and semiconducting -Ti-O-Ti- quantum chains. Therefore, ETS-10 has drawn attention to be used as ion-exchanger [20], photocatalyst [21], and adsorbent [22]. It is also an efficient material for the photocatalytic removal of organic pollutants [23] and selective removal of harmful heavy-metal ions [24–26]. The –Ti-O-Ti- chains have been investigated both in its structural properties, especially by Raman spectroscopy [27] as well as for its potential application fields as quantum wires (i.e. solar cells, photocatalysts [28, 29]). It is currently of interest to create nanoparticles within the ETS-10 matrix for such investigations [30]. Although there have been several attempts to investigate the local destruction caused by nanoparticle inclusion into ETS-10 structure, the effect of ion-exchange and inclusion of NPs have never been investigated by theoretical calculations. It is of great interest to gain more insightful information on the local changes occurring in ETS-10 matrix, and particularly –Ti-O-Ti- quantum wires as a function of ion-exchange and incorporated NPs.

Furthermore, ETS-10 has also been tested as a material for dye sensitized solar cells [31]. Due to unique -Ti-O-Ti- quantum chains , the local structure of ETS-10 has been examined through Raman spectroscopy [27, 32–34]. To better understand the effect of ion-exchange or ion-substitution on local structure of ETS-10 crystals, an atomistic level investigation with a quantum mechanical approach is necessary. In this thesis density function theory is employed in order to get better and accurate determination.

1.2 Theoretical Background

1.2.1 The Density Functional Theory

The Density Functional Theory(DFT) was presented in two papers in 1964 and 1965 by Hohenberg-Kohn and Kohn-Sham. DFT has proven to be one of the most promising theoretical approaches for determining the electronic properties of many-particle system. DFT is applicable for the whole range of systems including atoms, molecules, solids, nuclei, quantum and classical fluids. In the DFT approach, the focus of the problem is shifted from the wave function to the electronic density. Ionization energies, electrical properties, optical properties, magnetic properties, reaction paths, molecular structure, vibrational properties and more can be computed using DFT approach.

The goal in quantum mechanics and quantum chemistry is to solve the non-relativistic, time-independent Schrödinger equation.

$$H\psi_i(x_1, x_2, ..., x_N, R_1, R_2, ..., R_M) = E\psi_i(x_1, x_2, ..., x_N, R_1, R_2, ..., R_M) \tag{1.2}$$

where H is Hamiltonian, N is electron index and M is nuclei

$$H = -\frac{1}{2}\sum_{i=1}^{N}\nabla^2{}_i - \frac{1}{2}\sum_{I=1}^{M}\frac{1}{M_I}\nabla^2{}_I - \sum_{I=1}^{N}\sum_{I=1}^{M}\frac{Z_I}{r_{iI}} - \sum_{i=1}^{N}\sum_{j>i}^{N}\frac{1}{r_{ij}} + \sum_{I=1}^{M}\sum_{J>I}^{M}\frac{Z_I Z_J}{R_{IJ}} \tag{1.3}$$

Further actual kinetic energy terms of nuclei and electron are nuclei-nuclei, electron-nuclei and electron-electron relation.

Born-Oppenheimer Approximation

Nuclei have much larger masses relative to electrons and as a result they move much slowly. As a result, their kinetic energy can be ignored and electrons can be assumed to react instantaneously to changes in nuclear positions. Accordingly, an electronic Hamiltonian can be introduced;.

$$H = -\frac{1}{2}\sum_{i=1}^{N}\nabla^{2}{}_{i} - \sum_{I=1}^{N}\sum_{I=1}^{M}\frac{Z_I}{r_{iI}} - \sum_{i=1}^{N}\sum_{j>i}^{N}\frac{1}{r_{ij}} = T + V_{Ne} + V_{ee} \qquad (1.4)$$

where H is Hamiltonian, N is electron index and M is nuclei
In order to access the ground state wave-function and energy, wave-function based method often employ the variation principle where the expectation value is minimized by the ground state wave-function.

$$E[\psi] = \frac{<\psi|H|\psi>}{<\psi|\psi>} \qquad (1.5)$$

where

$$<\psi|H|\psi> = \int \psi^{*}H\psi, \mathrm{d}x \qquad (1.6)$$

According to the variational principle, result of predicted ground-state energy is always larger than true ground-state energy E_0, which certainly bounds the upper limit of the ground state energy. True ground-state of the system and ground state energy of the system E_0 can be calculated with minimization of the functional $E[]$ with respect to all N-electrons wave functions, which is;

$$E_0 = min_{\psi\rightarrow N}E[\psi] = min_{\psi\rightarrow N}<\psi|T + V_{Ne} + V_{ee}|\psi> \qquad (1.7)$$

The variational principle is generalized to obtain the ground state wave function of a system with N electrons and nuclear potential V_{ext}, energy of ground state and other information can be collected from this wave function.

The electron density is the key variable in the density functional theory. It is obtained from the many-particle wave-function using:

$$\rho(r) = N\int\cdots\int|\psi(r, r_2, \cdots, r_N)|^2\mathrm{d}_{r_2}\mathrm{d}_{r_3}\cdots\mathrm{d}_{r_N} \qquad (1.8)$$

Definition of the electron density is simply finding an electron of N electrons in the volume dr. It is depends on three spatial coordinates, an is a non-negative function.

The Hohenberg-Kohn Theorem

Consider two different external potentials with the same electron density function. Two different external potentials give two different Hamiltonians, H and H'. Even though electron densities are same, ground state wave functions should be different. The variational principle dictates that the ground state energy is lower than the expectation value $< \psi'|H|\psi >$.

$$E_0 < \langle\psi'|H|\psi'\rangle = \langle\psi'|H'|\psi'\rangle + \langle\psi'|H - H'|\psi'\rangle = E_0' + \int \rho(r)|V_{ext}(r) - V_{ext}'(r)|\mathrm{d}r \quad (1.9)$$

Similarly,

$$E_0' < \langle\psi'|H'|\psi'\rangle = \langle\psi'|H|\psi'\rangle + \langle\psi'|H' - H|\psi'\rangle = E_0 + \int \rho(r)|V_{ext}(r) - V_{ext}'(r)|\mathrm{d}r \quad (1.10)$$

Adding Eq. 1.9 and Eq.1.10, one obtains $E_o + E_o' < E_o + E_o'$, which is a contradiction. Thus both must have the same external potential that give the same ground state. Hence, all properties of the ground state can be determined from the electron density function $\rho(r)$ since N and $V_{ext}(r)$ are related to the same electron density. Therefore total energy can be written as:

$$E[\rho] = E_{Ne}[\rho] + T[\rho] + E_{ee}[\rho] = \int \rho(r)V_{Ne}(r)\mathrm{d}r + F_{HK}[\rho]. \quad (1.11)$$

$$F_{HK}[\rho] = T[\rho] + E_{ee}[\rho] \quad (1.12)$$

Electron-electron interaction, which is one of the most challenging part of the approximations, and the kinetic energy term as its stated in the Eq. 1.12 are contained in the $F_{HK}[\rho]$. The disadvantage of this functional is that its explicit form is a total unknown. The electron-electron interaction energy can be seperated into two parts:

$$E_{ee}[\rho] = \frac{1}{2}\int\int \frac{\rho(r_1)\rho(r_2)}{r_{12}}\mathrm{d}r_1\mathrm{d}r_2 + E_{XC} \quad (1.13)$$

where E_{ee} is electron-electron interaction energy, ρ is electron density and E_{XC}.
The second theorem of Hohenberg-Kohn states that any trial density selected $\rho(r)$ related with some external potential V_{ext}, which obeys conditions that are integral of the density gives the particle number N will give a total energy that is always bigger than true ground state energy. This means that a functional minimization of the energy with respect to ρ via $\frac{\delta E}{\delta \rho} = 0$ should yield the ground state density.

In order to apply the minimization procedure mentioned above,

$$E_0 = min_{\rho \to N}(F[\rho] + \int \rho(r)V_{Ne}\mathrm{d}r) \quad (1.14)$$

Kohn and Sham proposed an ansatz for the density [35] as;

$$\rho(r) = \sum_i^N |\psi_i(r)|^2 \quad (1.15)$$

where $\psi_i(r)$ are single-particle orbitals to be determined. ψ_i's orbitals that belong to an auxiliary non-interacting system. In this form ψ_i's kinetic energy, T_S , is not the real kinetic energy of the true system and may be written as:

$$T_S[\rho] = -\frac{1}{2}\sum_i < \psi_i|\nabla^2|\psi_i > \tag{1.16}$$

In order to make this function accountable, Kohn and Sham presented the exchange-correlation energy:

$$F[\rho] = T_S[\rho] + J[\rho] + E_{XC}[\rho] \tag{1.17}$$

$$E_{XC}[\rho] = (T[\rho] - T_S[\rho]) + (E_{ee}[\rho] - J[\rho]) \tag{1.18}$$

The total energy in terms of Kohn-Sham orbitals can be written as:

$$\begin{aligned} E[\rho] &= T_S[\rho] + \frac{1}{2}\int\int \frac{\rho(r_1)\rho(r_2)}{r_{12}}\mathrm{d}r_1\mathrm{d}r_2 + E_{XC}[\rho] + \int V_{Ne}\rho(r)\mathrm{d}r \\ &= -\frac{1}{2}\sum_i^N\langle\psi_i|\nabla^2|\psi_i\rangle + \frac{1}{2}\sum_i^N\sum_j^N\int\int|\psi_i(r_1)|^2\frac{1}{|r_1 - r_2|}|\psi_j(r_2)|^2|\mathrm{d}r_1\mathrm{d}r_2 \\ &+ E_{XC}[\rho] - \sum_i^N\int\sum_A^M\frac{Z_A}{|r_i - r_A|}|\psi_i(r_1)|^2\mathrm{d}r_1 \end{aligned} \tag{1.19}$$

In order to minimize the energy with constraints $\langle\psi_i|\psi_j\rangle = \delta_{ij}$, the variational principle leads to the choice of the orbitals ψ_i. The minimization of E with respect to ψ_i via $\frac{\delta E}{\delta\psi_i} = 0$ yields

$$\left(-\frac{1}{2}\nabla^2 + \int\frac{\rho(r_2)}{r_{12}} + V_{XC}(r_1) - \sum_A^M\frac{Z_A}{r_{1A}}\right)\psi_i = \psi_i(r_1) = \epsilon_i\psi_i(r_1) \tag{1.20}$$

where ϵ_i are the eigenvalues of the system of equation, usually refered to as Kohn-Sham energies.

Kohn-Sham orbitals have no physical meaning and significance. They are pure mathematical functions except for ϵ_{max}, whose negative equals the exact ionization energy. V_{XC} is the derivative of exchange-correlation energy with respect to density, ρ.

$$V_{XC} = \delta E_{XC}/\delta\rho \tag{1.21}$$

If exchange-correlation potential and the exchange-correlation energy exactly known, then Kohn-Sham equations would give the exact energy of the real system. The nonlinear nature of the total potential demands self consistent solutions. The density obtained through iterative solutions is the ground state density.

The Local Density Approximation (LDA)

The exchange-correlation energy described above must be approximated , rather carefully. The first and simplest approximation is local density approach(LDA). The central idea of the local density approximation is imitating a uniform neutral electron gas model. Assumption of the LDA can be summarized as:

$$E_{XC}^{LDA}[\rho] = \int \rho(r)\epsilon_{XC}(\rho(r))\mathrm{d}r \tag{1.22}$$

where $\epsilon_{XC}(\rho(r))$ is the exchange-correlation energy per volume per particle of the electron gas.
Exchange-correlation term can be separated as:

$$\epsilon_{XC}(\rho(r)) = \epsilon_X(\rho(r)) + \epsilon_C(\rho(r)) \tag{1.23}$$

ϵ_X is the exchange energy of single particle uniform electron gas model, which was presented by Bloch and Dirac [36]. It could be expressed as:

$$\epsilon_X = -\frac{3}{4}(\frac{3\rho(r)}{\pi})^{1/3} \tag{1.24}$$

ϵ_C is the correlation energy and is not an explicitly known term, while it has precise mathematical information with computer simulation approximated for uniform electron gas model [37].

The Generalized Gradient Approximation (GGA)

Advances in the DFT researches bring the idea of the generalized gradient approximation, GGA. The generalized gradient approximation uses gradient of the charge density in addition to LDA approach. It can be expressed as:

$$E_{XC}^{GGA}[\rho_\alpha, \rho_\beta] = \int f(\rho_\alpha, \rho_\beta, \nabla_{\rho_\alpha}, \nabla_{\rho_\beta})\mathrm{d}r \tag{1.25}$$

where ρ can take several forms. In this thesis, we use the PBE flavor developed by Perdew, Burke and Ernzerhof [38].

1.3 Solar Cell

Dye-sensitized solar cells and Grätzel cells are commemorated together due to first presentation and significant potential of the Grätzel cell. Dye sensitized solar cells are considered as second generation in the solar cell classifications due to combination of the organic and inorganic materials in the cell structure. First presentation of this type of solar cell was at 1991 by Grätzel with quantum efficiencies about 7% [39]. Currently reported efficiency values for the dye sensitized solar cells are about 12% again by Grätzel et al. [40].

Structure of DSSC

Porous semiconductor layer coated conductive glass as an anode/photoanode and a counter electrode with high conductivity form the electrodes of the solar cell. There should be a mediator between these parallel layers of metal oxide and conductive electrode, in most common cases it's a liquid electrolyte. Briefly described design is first presented by Grätzel [41], which can be seen in the Fig. 1.3. Electrolyte works as charge separator by creating an interface between semiconductor similar to interfaces of the multijunction solar cells and interfaces of the organic solar cells which separates the hole conductive material and electron conductive material. Dye sensitized solar cells have a sensitizer unit as a major difference which can be clued from the name. Dyes are generally large molecules that are adsorbed on the surface of the porous semiconductor and absorption of the incident solar radiation from these dyes are the first step of the photoelectric conversion process of solar cell device. Semiconductors are coated on a conductive, transparent substrate so that incident light is allowed to pass through the cell without major reflectance or scattering and this substrate should supply transfer between circuitry and cell so it should be highly conductive. In the most common cases fluorine doped tin oxide and indium doped tin oxide layers coated glasses are used as substrate. Another important design demand for the solar cell structure is conductivity of the counter electrode to minimize the efficiency losses caused by the resistance at the counter electrode. In most of the cases platinum, gold coatings are used. Instead of the complex charge cycle mechanism of the manufacturing of the DSSCs are relatively much easier than first generation silicon type solar cells and less expensive manufacturing costs.

Materials Used in DSSC Structure

There exists very wide range of different metal oxide semiconductors which creates great attraction to find an better alternative for the titanium dioxide in the dye sensitized solar cell structure. NiO, ZnO, SnO_2, Nb_2O_5, $SrTiO_3$ are some of the wide gap semiconductor alternatives used in this type of solar cells. Even though some electronic properties of these semiconductors, for example electron mobility [42], are much better than TiO_2, still the final efficiency of the conventional DSSC configuration is surprisingly higher. P-type semiconductor NiO based dye sensitized solar cell configuration has nearly same efficiency value with n-type TiO_2 based DSSC [43]. Second important alternative search is the sensitizer replacement, which is in the first configuration dye molecule. Sensitizer absorbs incident light and excited electron is transferred from LUMO of the sensitizer to conduction band of the semiconductor. Existence of the sensitizer is based on the wide bandgap of the semiconductor and narrow gap of the sensitizer. Sensitizers should be selected with some design criteria such that optimized efficiency values could be reached. HOMO and LUMO levels of the sensitizer should be such that LUMO level of the sensitizer should be at a higher level relative to conduction band of the semiconductor and HOMO level should be at a higher level respect to valance band of semiconductor. Oxidization and redox of the sensitizer molecule could be invertible in order to complete charge cycles and generate a stable design. Up to this point, the

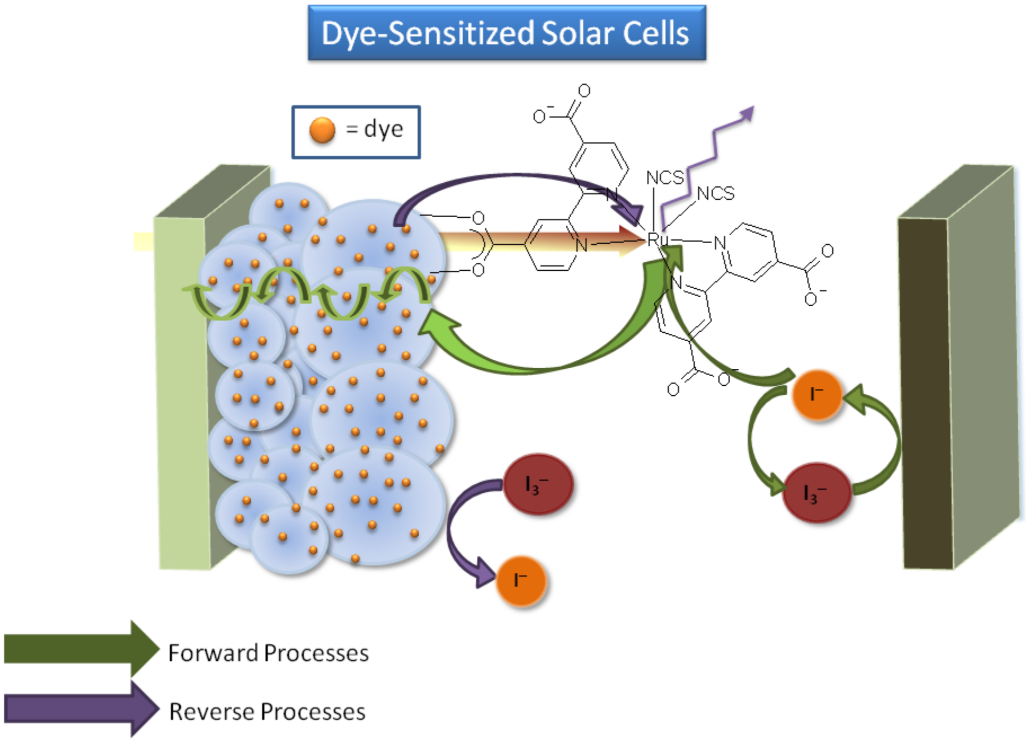

Figure 1.3: DSSC Design Schematic

most efficient design has been done with Ruthenium based organometallic dye sensitizers. Ruthenium based dyes have very wide absorption spectrum respect to optimized band gap and they have very rapid charge injection profile [44]. Another important element in the solar cell design is the electrolyte decision. Role of the electrolyte is as essential as sensitizer and semiconductor. Electrolyte performs as a medium between sensitizer/semiconductor complex and counter electrode. It completes charge cycle between counter electrode and sensitizer molecule by transferring incoming charge of counter electrode through circuitry to HOMO level of the sensitizer molecule. This configuration enables infinite charge cycle with unlimited sources of charge in theory. One of the most important challenges in electrolyte decision is thermally and chemically stable material decision. Due to scattering of the non-absorbed incident photon and excess energy carrying highly energetic photons, cell temperature elevates. Electrolyte material should stay unchanged under these thermally and chemically challenging conditions. Second important challenge for the electrolyte is the physical problem which is leakage/evaporation problem, in order to overcome that challenge solid or aerogel forms of electrolyte materials are popular research topics [45]. Hence, electrolyte should not absorb any incident photon in theory, and in practice it should absorb minimum amount of incident photon in order to preserve maximum energy potential for conversion at dye/semiconductor interface. Porous structure of semiconductor is very important at this step due to encapsulation of the electrolyte in the pores of the semiconductor will help incident photons to travel through device without absorbed by electrolyte. Currently, most popularly studied redox couples are are I^-/I_3^-, Br^-/Br_2, SCN^-/SCN_2, and metal ion based complexes [40, 46–48]. Solid state electrolyte material researches are promising about overcoming leakage and evaporation problems. However, weak contacts at the interfaces are significant problems reducing efficiency [49].

Operation Principles

The most fundamental operation principle of the dye-sensitized solar cell can be understood by band gap correlation of the materials. Incident photon reaches the device through transparent anode, monolayer adsorbed dye molecule (sensitizer) on the surface of the semiconductor absorbs the photons and dye molecule is converted into excited form. Electrons are injected from the excited dye molecules into the conduction band (CB) of semiconductor, and dye becomes oxidized. Electrons travel through the porous semiconductor and reach the transparent anode. After transparent anode, electron passes through external circuitry and comes to the counter electrode. The mediator which is the redox couple in the electrolyte transfers electrons from counter electrode to oxidized sensitizer (dye) molecule, this will reduce oxidized dye molecule to neutral state. This configuration is a complete charge cycle and until a next photon absorption device stays in the initial situation. An important limitation for the DSSCs is the theoretical maximum limit of the open-circuit voltage is formed by the energy difference of the semiconductor and electrolyte material.

CHAPTER 2

COMPUTATIONAL, EXPERIMENTAL AND APPLICATION DETAILS

2.1 Modelling and Computational Details

The calculations presented in this work were performed using plane-wave pseudopotential density functional theory [35, 50] with the gradient-corrected approximation (GGA) and ultrasoft pseudopotentials [51]. The Perdew-Becke-Ernzerhof [52] exchange-correlation functional as implemented in the Quantum-Espresso distribution [53] was used in all calculations. The open-source program, XCrysDen [54], was used for visualization and to produce the figures. During the BFGS geometry optimizations, a force threshold per atom of 0.025 eV/Å was used and all atomic coordinates were allowed to relax. The plane-wave basis set used is characterized by a kinetic energy cutoff of 35 Ryd, while the charge density cutoff is 350 Ryd. For both models of ETS-10 considered in the present study, atomic positions and the a cell parameter have been taken from the experimental data of Anderson et al. [17], corresponding to polymorph A (cell parameters $a = b$ =14.85 Å and c=27.08 Å). The two models are reported in 2.1. Model I is similar to the corresponding Model I used by Damin et al. [55], with two Ti atoms in the repeting unit and the surrounding Si atoms. Model II is instead characterized by a larger number of framework atoms in the repeting unit; it is similar to Model II used by Damin et al. [55] with the important difference that the repeting unit is twice that used in ref. [55]. The minimum distance between periodic images is about 12 Å. For both models the extraframework Na^+ cations are explicitly included for charge neutrality, therefore both models aim at reproducing the (Na,Na)-ETS-10. Geometry optimizations and total energy calculations have been performed with a $1\times8\times1$ Monkhorst-Pack [56] k-point mesh, marzari-vanderbilt smearing occupations with degauss parameter 0.01. Löwdin partial charges are computed with a spilling parameter of 0.0123 and phonon calculations are completed with a convergence threshold of 1.0D-9.

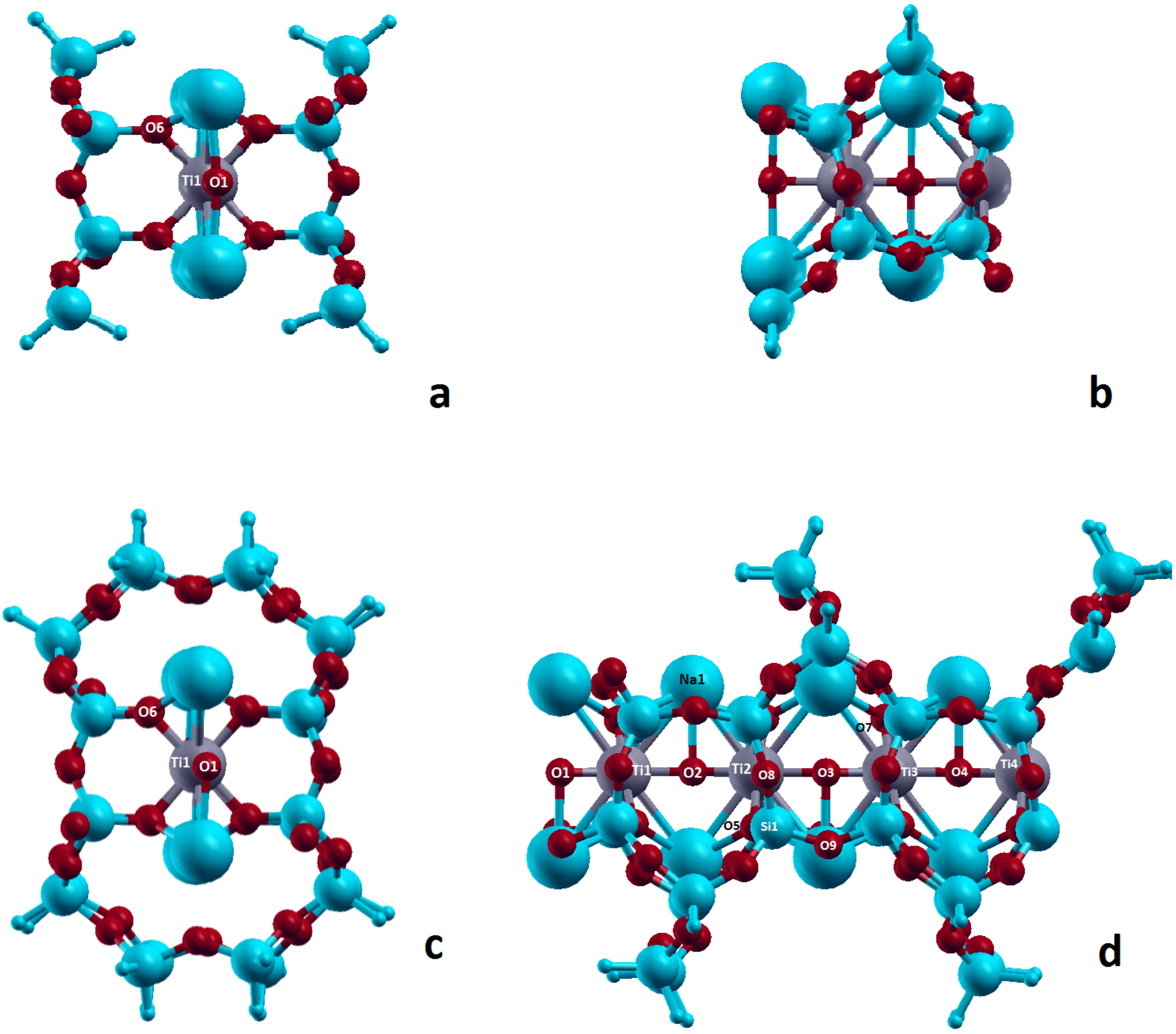

Figure 2.1: Models of the ETS-10 used in the present work. Model I(a, and b) and Model II (c and d)

2.2 Experimental Details

2.2.1 General

All commercially obtained compounds used in synthesis and modification are as indicated below: $AgNO_3$, $AuCl_3$, $RuCl_3$, TiO_2 (P25, 76 wt.% anatase and 24 wt.% rutile, Degussa), $NaSiO_2$ were obtained from Sigma-Aldrich. NaCl (99.0%), KCl (99.0%), and H_2SO_4 (96.5%) were received from J.T. Baker. Zinc sulphate heptahydrate and calcium chloride were received from Merck. Deionized water was double distilled by water purification system. All chemicals used in this study are in reaction grade.

2.2.2 Analytical Procedures and Equipment

Morphological and structural properties of the all ETS-10 samples were observed by field emission scanning electron microscope (FE-SEM, FEI Quanta 400). Phase identification of all samples was carried out by X-ray powder diffraction (XRD) through Rigaku-Ultima IV XRD. The diffraction peaks were scanned between 5 and 40 with scan speed of 1/min. Raman microscope was utilized as Renishaw type in the Raman spectroscopy analyses. The excitation wavelength at 532 nm and a power of 0.5-1mW were chosen for the analysis. All analysis were performed at METU Central Laboratory.

2.2.3 Synthesis of Titanosilicate ETS-10

ETS-10 crystals were synthesized by using the molar composition of 3.4 Na_2O:1.5 K_2O:TiO_2:5.5 SiO_2:150 H_2O [34]. The hydrothermal synthesis of ETS-10 is explained elsewhere [32]. NaCl and KCl were dissolved in deionized water. For Si precursor solution sodium silicate solution was added. In another bottle, H_2SO_4 was added to deionized water for preparation of the Ti precursor solution. Later, P25 TiO_2 was added to this bottle. The Ti precursor solution was poured into the Si precursor solution. After measuring the pH (pH = 10.6 - 10.8) the mixture was transferred into Teflon-lined stainless steel autoclaves. The static synthesis was conducted for 3 days at 230 °C. The products were cooled to room temperature, centrifuged, washed with deionized water, and dried overnight in ambient air at 70 °C.

2.2.4 Ion-exchange of Titanosilicate ETS-10

The ion-exchanged-ETS-10 samples were produced by adding 400 mg of as-synthesized ETS-10 crystals to a 100 mL aqueous $AgNO_3$, $RuCl_3$, $AuCl_3$, $ZnSO_4 \cdot 7H_2O$, $CaCl_2 \cdot 2H_2O$ solution of a given concentration, i.e., full ion-exchange capacity. The solution was stirred vigorously for 24 h. After ion exchange, the samples were washed several times by centrifugation and dried at 70 °C under ambient air, and collected as a powder material.

2.3 Application Details: Solar Cell Manufacturing

Paste Preparation

Thick films of ETS-10 nanocrystals were deposited on transparent, conducting substrates by screen printing and doctor blade technique. Choice of transparent, conducting substrate is flourine doped tin dioxide doped glasses. In order to deposit ETS-10 crystals as a thin film on FTO, presence of a binder with large viscosity paste is essential. ETS-10 crystals were dispersed in anhydrous alpha-terpineol (Fluka) and ethyl cellulose (Aldrich) mixture. Alpha-terpineol works as required medium for ETS-10 crystals to be dispersed uniformly, and ethyl cellulose works as organic binder for the ETS-10 and FTO substrate. In order to prevent aggregation, synthesized ETS-10 powders were pounded in the mortar. Dispersed and uniformed ETS-10 powders were added into an ethanol solution of 100 ml. Ethanol/ETS-10 mixture was ultra-sonicated for 15 minutes. After sonication, anhydrous alpha-terpineol was added to ethanol/ETS-10 mixture and stirred for about 15 minutes with magnetic stirrer. After stirring process, mixture was ultra-sonicated about 15 minutes. Ethyl cellulose and ethanol solution was prepared and mixed with ethanol/ETS-10 solution. Final solution was ultra-sonicated for 15 minutes and then it was stirred in the magnetic stirrer at 50 °C for 6-7 days. The duration for stirring depends on the viscosity of the paste in order to fulfil good quality thin film deposition on the substrate. Final mixture can be summarized as 0.5gr of ethyl cellulose, 3.5gr of alpha-terpineol and 1gr of ETS-10 powder.

Substrate Cleaning

Working with clean substrate is essential regarding cell efficiency, adsorption of ETS-10 on FTO substrate and semiconductor/dye interface. Ultrasonication of FTO coated glasses in deionized water solution were applied a few times for 15-20 minutes in order to eliminate contamination. Afterwards, same treatment was applied using acetone for 20 minutes and finally with ethanol solution for 20 minutes.

Paste Deposition

Prepared paste was applied on the surface of FTO coated glass by screen printing and doctor blade methods. Thickness of the films were controlled by first observing the viscosity of the paste and secondly the thickness of the frame material of screen in the screen printing method. In the doctor blade method, the thickness depends on the thickness of the duck tape. 5mm× 5mm square frames were studied, according to the SEM cross section analysis, the desired thickness was reached after applying four layers of scotch tape. Observed film thickness was about 4μm. After doctor blade application, applied pastes were heated to 130° for 15 minutes to start the first step of the deposition by obtaining dry and contaminant free surfaces. Following the first 15-minute heating, prepared paste/FTO glass complexes were heated to

450° for 1 hour in order to finalize the deposition of paste on FTO glass and eliminate the unwanted organic compounds.

Dye Adsorption

The following step is the adsorption of dye onto the prepared ETS-10 films. In order to achieve this step, ETS-10 deposited FTO glasses were kept in 50 mM dye solution which was dissolved in the anhydrous acetonitrile solution. ETS/FTO glasses were arranged parallel to the ground in order to ease the adsorption of dye molecules on the surface of substrate. Selected dye molecule in this work is commercially purchased N719. Duration of the dye adsorption process varies from 1-3 days, in order to achieve the desired adsorption. In order to eliminate unwanted contamination, a controlled environment was prepared in a glove box. After dye adsorption step, substrates were washed with anhydrous acetonitrile and color change was observed in the applied ETS-10 films.

Counter Electrode

DSSC has a typical sandwich design which is shown in the Fig. 2.2. In order to complete this design, counter electrode needs to be prepared in synchronization with active region substrate. Counter electrode is a highly conductive transparent metal/FTO glass while these metal/FTO glass substrates have one or two holes depending on the application procedure and are drilled before metal deposition. These holes are channels for introducing electrolyte into the system. In our work, only one hole was drilled. Selected metal was platinum. Platinum precursor solution was dropped on the FTO coated glass substrates. Solution drops were spread to desired areas with a clean, glass tip. Platinum deposition was completed by 45 minutes of heat treatment at 450°.

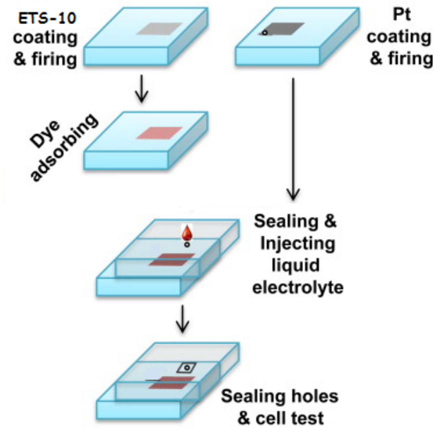

Figure 2.2: Manufacturing Process of DSSC

Reunite of Electrodes

Binding of Pt coated counter electrode and ETS-10/dye/FTO coated glass substrates was accomplished by Surlyn polymer which melts easily at 110° with a thickness of 25μ. Surlyn layers were prepared with windows of same dimensions with ETS-10 films in order to supply direct interaction of electrolyte and ETS-10 and prevent electrolyte leakage from side walls. Combination was done at heater to melt polymer easily. Electrodes were kept about 2-4 minutes until desired adherence achieved.

Electrolyte Addition and Cell Characterization

Electrolyte solution was dropped on to the hole of the cell in the vacuum chamber. System was taken into vacuum and held that way until desired influx of electrolyte solution into the hole was fulfilled. If desired amount of electrolyte influx was not achieved, This procedure was repeated. Afterwards, hole of the counter electrode was sealed with a melting polymer and glass, which prevented electrolyte leakage and also did not affect the solar radiation passing through the counter electrode. Finally silver contacts were prepared on the edges of both electrodes with silver paste. Silver contacts were kept in UV light for a few minutes in order to complete the deposition process. Cell characteristics were analysed with AM 1.5 standards solar simulator.

CHAPTER 3

RESULTS AND DISCUSSIONS

3.1 Modelling Results

Engelhard titanosilicate (ETS-10) is a synthetic microporous crystalline material (pore dimensions 4.9 and 7.6 Å) whose framework structure results from chains of corner-sharing TiO_6 octahedra and SiO_4 tetrahedra linked through bridging oxygen atoms [17, 57] generating a 12-membered ring pore structure. Although the material is crystalline, its structural determination has proven to be challenging [58]. ETS-10 structure can be described in terms of two ideal polymorphs; polymorph A has a tetragonal lattice (space group $P4_1$ and $P4_3$) while polymorph B belongs to the monoclinic system (space group C2/c). The main difference between the two polymorphs is the stacking sequence of the unit cell along the [001] direction: polymorph A has zigzag channels while polymorph B structure is characterized by a diagonal stacking arrangement [55, 59]. In the real material, an intergrowth of both polymorphs is responsible for its disorder such as stacking faults and line defects. An intriguing characteristic of the ETS-10 is related to the fact that TiO_6 octahedra are linked together to form -Ti-O-Ti-O-Ti- wires that run in the crystal in [100] and [010] directions [17]. These linear chains are effectively insulated by the silica matrix, and can be regarded as a 1-D quantum-confined form of titania [60] whose band gap is related to the length of the crystals along the [110] direction [18].

In the as synthesized material ($(Na,K)_2TiSi_5O_{13}$ [17, 58]), extra-framework Na^+ and K^+ cations compensate the two negative charges of each TiO_6^{2-} unit. Several theoretical studies focused on the location of the extra-framework cations. According to an earlier *ab-initio* investigation by Ching et al. [61] the Na^+ cations are likely to be located only in the seven-member rings cavities, at different distances from the titanium atoms. In the work of Grillo and Carrazza [62] four different cation sites have been identified for both Na^+ and K^+ cations; the sites are distributed along the Ti–O–Ti wire, surrounded by silicon five-rings and between two vicinal Ti atoms of the wire. In a subsequent joint theoretical and experimental NMR study, Anderson et al. [63] identified five different cations sites, of which sites I, II and III are in agreement with the corresponding of Grillo et al. [62]. The Hartree-Fock (HF) and periodic Density Functional Theory (DFT) calculations of Damin et al. [55] also agree with the results of Grillo et al. which is concerned the position of the Na^+ cations. These cations can be exchanged with other cations through ion exchange in aqueous solutions; the ion exchange is however responsible for local damage of the ETS-10 structure. [20,32,64].

Due to its high cation-exchange capacity [20,32,64–66] and the presence of unique - Ti-O-Ti-wires, ETS-10 has been used as an ion- exchanger [20, 32, 64, 66] , and as active catalyst for several reactions [67–69]. Recently ETS-10 has found promising applications in the removal of harmful heavy-metal ions [70], in photocatalysis, for dye sensitized solar cells [31] and for photochromism.

Over the last two decades, several theoretical and experimental studies have been devoted to the elucidation of the structural, electronic, and vibrational properties of ETS-10. [33, 55, 58–61, 71–76]. The UV-vis spectrum of ETS-10 (sodium form) is characterized by two intense absorption bands, with maxima at 4.4 and 5.8 eV [77]. Both bands have been assigned to ligand-to-metal charge transfer (LMCT) transitions, which differ by the types of oxygen ligands involved. The LMCT transition at 5.8 eV involves the oxygens in the plane perpendicular to the quantum wire, and is therefore localized in a single TiO_6 unit, while the transition at 4.4 eV (with an inflection point at 4.02 eV [77]) is delocalized in the quantum wire [60, 72, 77].

Theoretical estimates of the ETS-10 band-gap vary between different sources. First-principle calculations performed by Ching et al. give a band gap value of 2.33 eV [61] while a value of 3.95 eV, in rather good agreement with the experiment, has been reported by Bordiga et al. [72] in the local density approximation (LDA) and by using a simplified model of ETS-10. On the basis of their QM/MM studies, Zimmerman et al. reported an estimated optical band-gap of about 3.0 eV [59], while Damin et al. [55] report a value of 3.22 eV by using the LDA approximation and the VWN exchange correlation potential. All these studies agree for which concern the major atomic orbital contributions of the top of the valence band (Oxygen $2p$ orbitals) and the bottom of the conduction band (Ti $3d$ orbitals), therefore supporting the earlier study of Borello et al. [77]. This band is blue-shifted, due to quantum confinement effects, by about 0.8–1.0 eV with respect to the correspondent E_g value of bulk rutile (3.02 eV) and anatase (3.18 eV). Furthermore, the band-gap energy is not appreciably affected by cation exchange (maximum variation of the order of 5% [60]). We note that discrepancies in the predicted band-gap energy from different sources are due to both the use of simplified model structures and well known deficiencies of DFT in predicting band-gap energies accurately.

Raman spectroscopy is a valuable tool for the study of structural defects of the Ti-O-Ti quantum wire in ETS-10. [32, 64, 65, 73, 78]. A strong band at about 725 cm^{-1} dominates the experimental Raman spectrum [78–80] and has been assigned to Ti–O–Ti stretching in the wire [55, 80]. Its position and width is related to the average lenght of the Ti–O–Ti chains (and therefore to the concentration of defects in ETS-10 samples), and is therefore used to investigate structural changes following ion-exchange studies [32, 64, 73]. A general consensus is that the octahedral arrangements of the Oxygen ligands around each Ti^{4+} center is distorted. The distance between Ti atoms and the four oxygens bridging Ti and Si atoms (Oeq) is in the range of 2.00–2.10 Å [74, 75]. Some conflicts still exist, for which concern the Ti–O bond lengths along the quantum wire. In an earlier study, Sankar et al. [74], were able to obtain a satisfactory fit of their EXAFS data with a model characterized by two inequivalent Ti–O bonds along the chain (with Ti–O distances of 1.71 and 2.11 Å), and with a Ti–O–Ti bond angle of 165°, in disagreement with other experimental [58, 75] and theoretical studies [55], all of which suggest equivalent Ti–O bond lengths along the chain, together with a Ti–O–Ti bond angle much closer to 180°.

In modelling part of this work a comprehensive study of the structural, electronic, and vibrational properties of ETS-10 (sodium form) and ion-exchanged ETS-10, M^+-ETS-10 (M^+ = K^+, Ca^{2+}, Ag^+, Zn^{+2}, Ru^{3+}, and Au^{3+}) by using DFT on three ETS-10 model systems is carried out. The effect of nature of the extra-framework cations on the band gap, the vibrational modes and the electronic structures are investigated in detail. In addition to that silver nanoparticles and dye molecules are modelled and their structural and electronic properties are investigated. The aim underlying the modelling part of this work is estimating the changes occurring in ETS-10 upon inserting dye molecules or nanoparticles, which is quite challenging due to lack of of existing experimental data. Understanding, or at least estimating the structural and electronic variations occurring in a unique crystalline material with TiO_2 quantum wire upon outside forces like ion-exchange, nanoparticle and dye insertion can be essential for real application studies, such as solar cells. In order to create more supporting information, in addition to the ions mentioned above, B, Cd, Cu and Pb exchanged ETS-10 computations have been successfully completed and presented as well.

3.1.1 Na-ETS-10 Models

Until receiving an optimized ETS-10 model, several different attempts had been tried. Fixing frame atoms and hydrogen atoms was another option in order to get stable outputs. Selected geometrical parameters for the two models of ETS-10 considered in this work are reported in Table 3.1 and compared with experimental [58,74,75] and theoretical values [55,59] from the literature. Focusing first to the two models investigated, we clearly see that their optimized structure is very similar concerning the quantum wire and the insulating silica matrix. In particular, the optimized O–Ti–O angles of the quantum wire are close to linearity while the Ti–O–Ti angle deviates appreciably from 180°. The optimized value of 165° found for both models falls in between the theoretical estimates of Zimmerman et al. [59] (158°) and Damin et al. [55] (173°) and in perfect agreement with the value quoted by Sankar et al. [74]. It is also worth noticing that both models predict a sequence of alternating long and short Ti–O bonds, and therefore in broad agreement with the EXAFS study of Sankar et al. [74]; the predicted bond length difference is however less marked (about 0.20 Å as compared to a value of about 0.40 Å as reported in Ref. [74]). In this respect our findings compare favourably with those of Zimmerman et al. and are in disagreement with those of Damin et al. [55].

Table3.1: Selected structural parameters of the optimized structures of the two models of ETS-10 employed in the present study, and comparison with theoretical and experimental data from the literature. Bond lengths in Å and angles in degrees respectively. For the atomic labeling we refer to Fig. 2.1.

	EXAFS [74]	XRD [58]	EXAFS [75]	QM/MM [59]	*ab-initio* [55]	Model I	Model II
Ti1-Ti2	3.73	-	3.76	3.71	3.76	3.71	3.75
Ti2-O2	1.87	1.87	1.73	1.86	1.88	1.79	1.78
Ti2-O3	-	-	2.11	1.96	1.88	1.96	2.00
Na1-O2	-	-	-	-	2.4-2.6	2.4-2.5	2.4
Ti1-O2	-	-	-	1.89	-	1.96	2.00
Ti1-O1	-	-	-	1.92	-	1.79	1.78
Ti3-O3	-	-	-	1.89	-	1.96	2.00
Ti3-O4	-	-	-	1.92	-	1.79	1.78
Ti2-O5	2.05	1.99	2.02	1.91-2.13	2.00	2.02	2.03
Ti1-O6	-	-	-	1.92-2.11	-	2.02	2.03
Ti3-O7	-	-	-	1.92-2.11	-	2.02	2.03
Ti2-O8	3.78	3.74	-	3.56	3.5	3.6	3.5
Ti2-O6	4.10	4.17	-	4.16-4.40	4.05-4.15	4.07-4.31	4.31
Ti2-O9	4.22	4.23-4.25	-	3.92-4.40	4.18-4.33	4.09	4.10
Ti2-Si1	3.32	3.27	3.31	3.27-3.32	3.26-3.27	3.30	3.25
Ti1-Na1	3.05	-	3.07	3.07-3.14	-	3.03-3.10	3.05
O5-Si1	1.60	1.70-1.71	-	1.64-1.65	1.61-1.62	1.63	1.63
Ti1-O2-Ti2	180	178	165	158	173	165	165
O2-Ti2-O3	-	180	-	-	180	179	180
Ti2-O5-Si1	132	-	130	122-129	129-130	128-130	130
O2-Ti2-O5	-	-	-	-	-	88.27	92.78

Concerning the geometry of the TiO_6 unit, the present results for both models support earlier findings of Damin et al. [55], with similar deviations from the ideal octahedral geometry. In particular, for model I, of the four O_{eq}–Ti–O_{eq} angles two are of about 84° and two of about 96°, with a similar pattern in model II, while the O_{eq}–Ti–O_{ap} angles are about 87° (see Table 3.1) . For both models, the Ti–O_{eq} bonds are in the range of 2.01-2.03 Å, in good agreement with previous results. The location of the Na^+ cations is instead in agreement with previous studies [62].

In Table 3.2 we report the partial charge on selected atoms for Model II of ETS-10, resulting from a Löwdin population analysis. Ti atoms are positively charged (1.63–1.64 units of charge) while the oxygen atoms directly bonded to it have negative charge in the range -0.77–-0.89 $|e|$ with the O_{ap} atoms slightly less negatively charged than O_{eq}. The alternating long and short Ti–O bond nature characterizing the wire does not affect the electron density distribution. The variation of the negative partial charges on all other O atoms of the framework is very narrow (see Table 3.2).

Table3.2: Löwdin population analysis for selected atoms of Model II of ETS-10.

	Partial Charge
Atom type	Model II
Ti	[1.63-1.64]
O_{ap}	[-0.77,-0.78]
O_{eq}	[-0.88,-0.89]
Orest	[-0.80,-0.82]
Na	[0.77,0.82]
Si_{eq}	[1.76,1.77]
Si_{frame1}	1.58
Si_{frame2}	1.28

The Si atoms directly bonded to each TiO_6 unit have a larger positive charge, around 1.8 $|e|$ which should be compared with a positive charge of about 1.28–1.58 $|e|$ characterizing the other Si atoms of the framework. This can be easily understood considering that there are two different types of Si atoms for both models. The Si atoms directly bonded to the TiO_6 unit are directly bonded to four O atoms in a tetrahedral arrangement, while all the other Si atoms of the framework are bonded to two O atoms and two H atoms which are used to saturate dangling bonds. The extraframework Na^+ cations are arranged in two different sites, and as a result the computed partial positive charge for these two positions are different, even if the difference is not large.

In Fig. 3.1 we report the total and partial density of states (PDOS) near the Fermi level for Model II. The calculated band gaps are of about 3.26 eV for model I and about 3.34 eV for model II and this value is consistent with the DFT and TDDFT results of Zimmerman et al [59] who quoted a band gap value of about 3.10 eV, and a LDA-VWN gap of 3.22 eV reported by Damin et al. [55]. All these DFT calculations underestimate by about 1.0 eV the experimental band-gap (4.02 eV) [60]; the underestimation of the band-gap by DFT calculations is a well known characteristic of ground-state DFT, and well documented in the literature [81]. In good agreement with the previous PDOS calculations [55, 59, 61, 72], the top of the valence band show major contributions from the $2p$ orbitals of O_{ap} and O_{eq} atoms while the bottom of the conduction band is composed almost exclusively by contributions from the Ti $3d$ orbitals.

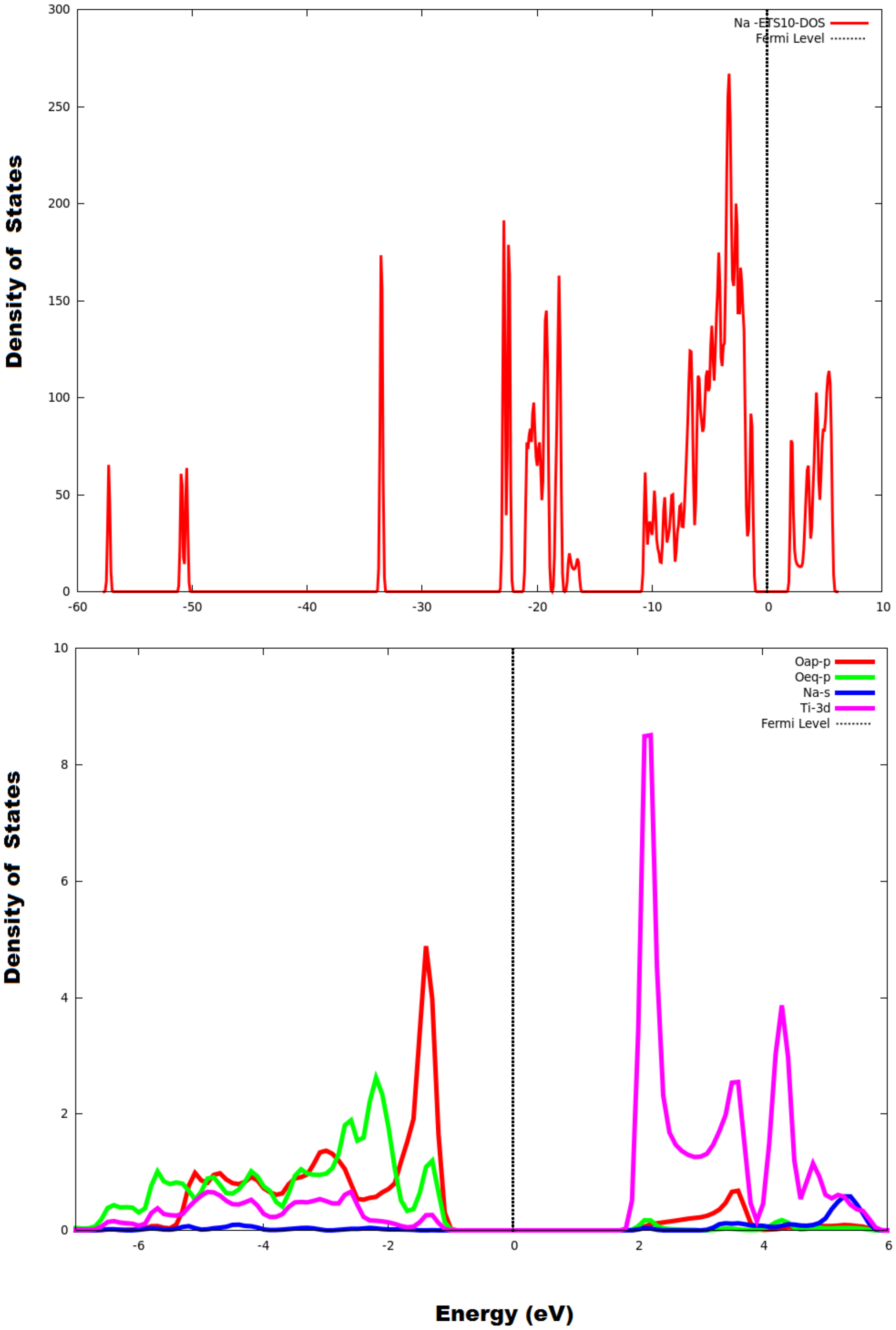

Figure 3.1: Total density of states (DOS) and partial density of states near the Fermi level for both models of ETS-10.

3.1.1.1 Quantum Wire Calculations

In order to clarify the optimized models and Model I and Model II results, a third model Model III is developed. Model III has only 24 atoms, which can be accepted as quiet small with respect to Model I and Model II. Model III has only -O-Ti-O-Ti-O- chain and first neighbouring atoms around quantum wire. Model III can be seen in the Fig 3.2. Maximum 0.12 Å bond difference and 4° of bond angle suggest that all models converge to approximately same results. In the model III, Ti-O-Ti angle was observed as 178° which is in consistent with results of Damin et al. [55], while one long and one short Ti-O bond distance in the quantum wire was preserved. Variance from 165° in the model III can be explained by the lack of frame atoms. Frame atoms forces the quantum wire geometry to make a small zigzag pattern instead of fully linear geometry. Succesful convergence of all three model with different atom number and variance in the frame atoms and quantum wire repetition unit gives supporting information in the ion exchange chapter. Effect of the frame atoms on the cations and quantum wire shift could be more easily seen with these models.

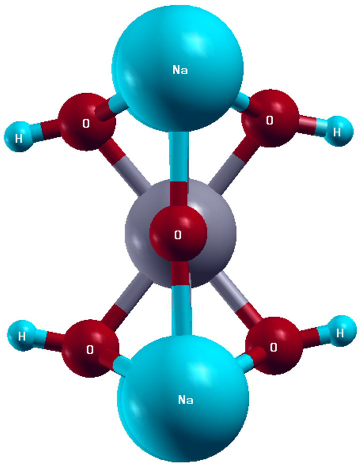

Figure 3.2: Na-ETS-10 Model III

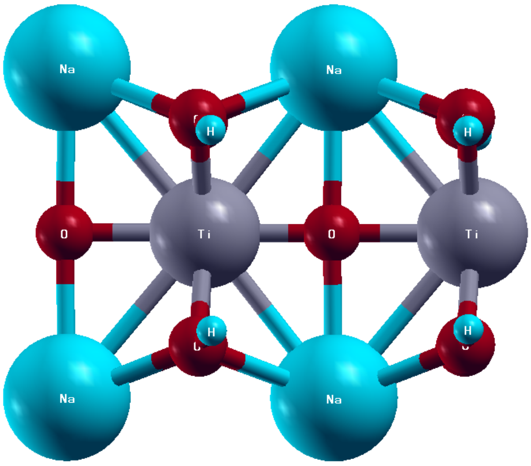

Figure 3.3: Na-ETS-10 Model III side

Table3.3: Selected structural parameters of the optimized structures of the three models of ETS-10. For the atomic labeling we refer to Fig. 2.1. Represented bond distance units are Å.

	Model I	Model II	Model III
Ti1-Ti2	3.71	3.75	3.75
Ti2-O2	1.79	1.78	1.78
Ti2-O3	1.96	2.00	1.97
Na1-O2	2.4-2.5	2.4	2.32
Ti1-O2	1.96	2.00	1.97
Ti1-O1	1.79	1.78	1.78
Ti3-O3	1.96	2.00	1.97
Ti3-O4	1.79	1.78	1.78
Ti2-O5	2.02	2.03	2.05
Ti1-O6	2.02	2.03	2.05
Ti3-O7	2.02	2.03	2.05
Ti2-O6	4.07-4.31	4.31	4.20
Ti1-Na1	3.03-3.10	3.05	3.02
Ti1-O2-Ti2	165°	165°	178°
O2-Ti2-O3	179°	180°	180°
O2-Ti2-O5	88.27°	92.78°	86.84°

3.1.2 Ion-exchanged (M)-ETS-10 Model

In this section we examine the structural and electronic properties of the ion-exchanged ETS-10 models. Two different cases are considered: a partial cation exchange ($\frac{1}{8}$ of the available cationic sites), and full cation exchange. The results are compared and contrasted to the case of the sodium form considered above. To aid the following discussion, we collected in Table 3.4 the electronegativities (Pauling and Allen scale) and atomic and ionic radius of the extraframework species, taken from the literature [82–85].

We report in Fig. 3.4 the optimized geometry of the fully exchanged M^+-ETS-10 (M^+ = Na^+,K^+, Ca^{2+}, Ag^+, Zn^{+2}, Ru^{3+}, and Au^{3+}), together with the corresponding PDOS around the Fermi level, while the corresponding structures and PDOSs for the partially (1/8) exchanged forms are reported in Fig. 3.5. We will consider the results obtained from Model II in the following.

Table3.4: Pauling (Allen) electronegativity (EN), atomic and ionic radius of the extraframework cations considered in this work. Atomic and ionic radii are in Å.

Element	EN	atomic radius	ionic radius
K	0.82 (0.73)	2.27	(+1) 1.37
Na	0.93 (0.87)	1.86	(+1) 1.00
Ca	1.00 (1.03)	1.80	(+2) 1.06
Zn	1.65 (1.59)	1.35	(+2) 0.68
Ag	1.93 (1.87)	1.60	(+1) 1.00
Ru	2.2 (1.54)	1.30	(+3) 0.68,(+4) 0.62
Au	2.54 (1.92)	1.35	(+1) 1.37,(+3) 0.68

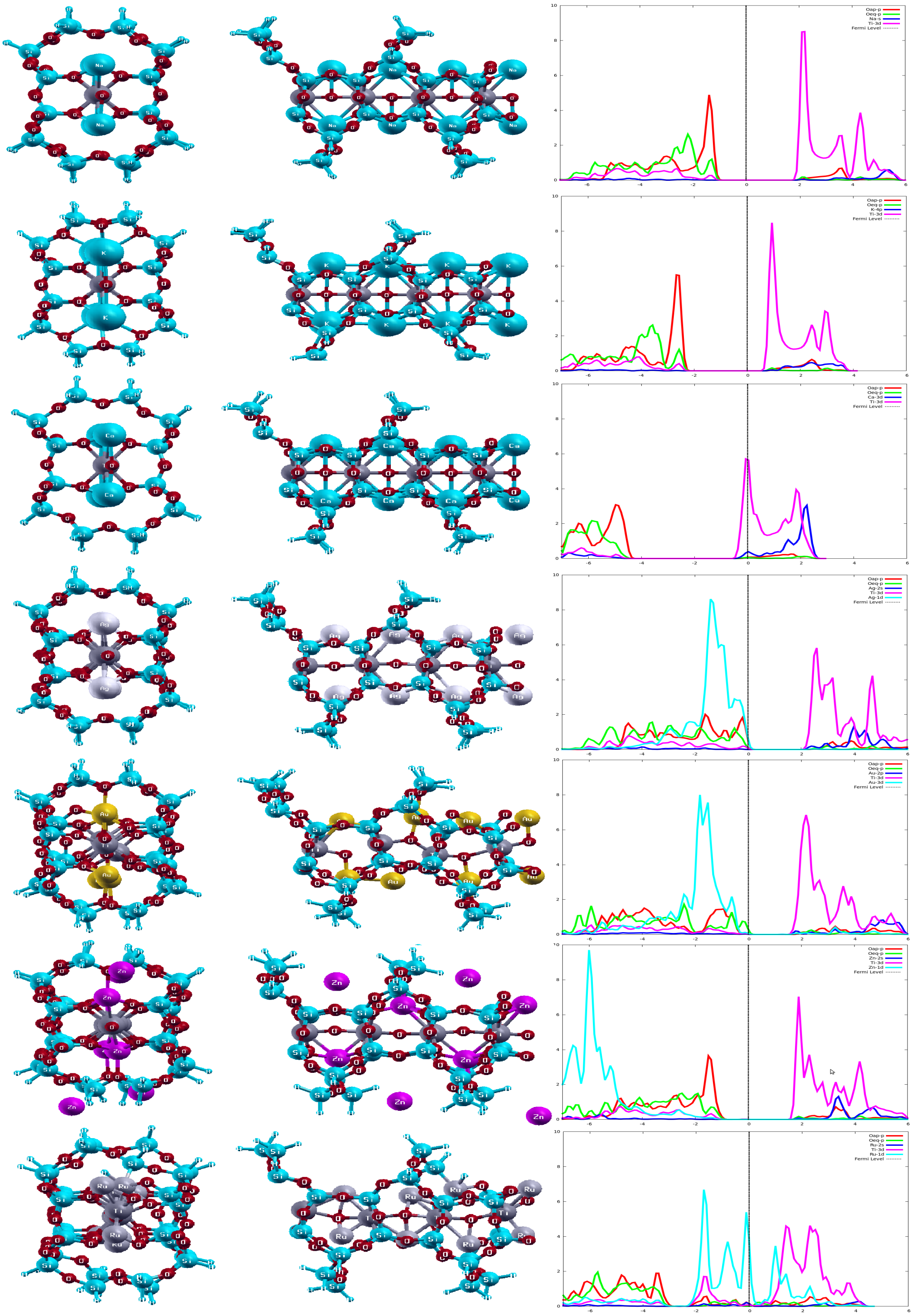

Figure 3.4: Optimized structures (left) and PDOS (right) of the fully exchanged M-ETS10 Model II. Results are ordered as Na, K, Ca, Ag, Au, Zn, Ru exchanged M-ETS-10 models respectively.

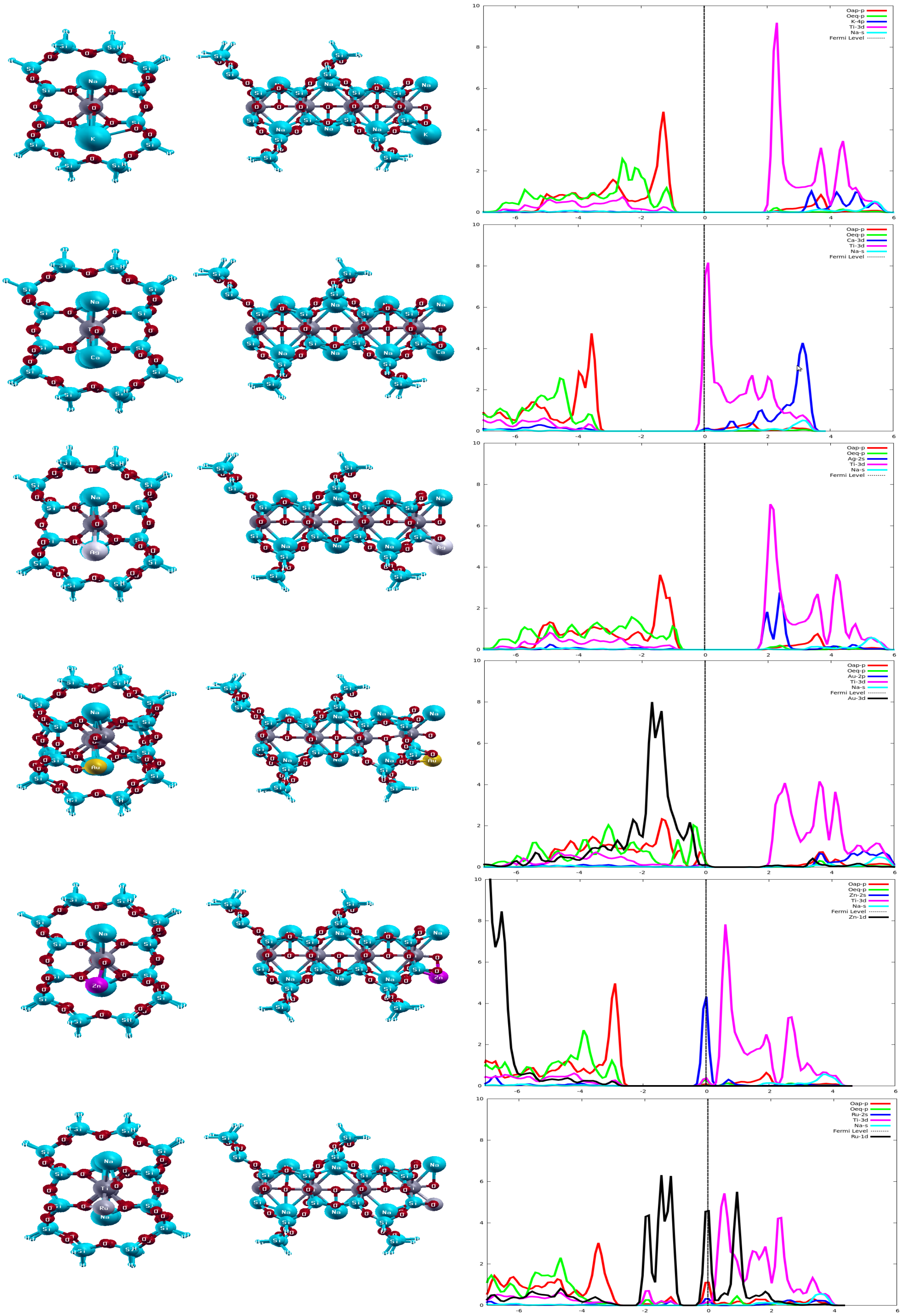

Figure 3.5: Optimized structures (left) and PDOS (right) of the partially exchanged (1/8) M-ETS10 Model II. Results are ordered as K, Ca, Ag, Au, Zn, Ru exchanged (Na, M)-ETS-10 models respectively.

Let us first analyse the cation site locations in the case of full cation exchange ; these are very important in determining the catalytic properties of the ETS-10 material [62]. The site locations of K, Ca, Ag, and Au extraframework cations in the optimized structures are very similar to the corresponding sodium form, as can be seen from Fig. 3.4 and Fig. 3.6-3.12. A markedly different situation characterize the Zn and Ru forms. Of the two independent sites occupied by Zn species, one is well outside the region of the quantum wire, while in the second site Zn interacts with two O_{ap} atoms, four O_{eq} and two Ti atoms. This can be rationalized by the results of a population analysis, and reported in Table 3.6, which reveals that the Zn atom far from the titania wire is neutral (0.04 $|e|$) while a partial charge of 1.48 $|e|$ characterizes the Zn atom interacting with the TiO_6 units. When Na extraframework cations are replaced by Ru atoms, the optimized cation positions strongly differ from those in the sodium form. Their inclusion affect significantly the geometric properties of both the Ti and O atoms of the quantum wire and of the surrounding framework, as can be seen for selected geometric parameters in Table 3.5. A population analysis reveals that the partial positive charge on the Ru atoms varies between 0.01–0.33 $|e|$ (see Table 3.6). Finally, in the case of the Au species, the site locations in the optimized structure are similar to the sodium form, but the increased ionic size compared to Na^+ causes a rearrangement of the O_{eq} and O_{ap} positions, as can be inferred from the results collected in Table 3.5.

Table3.5: Structural properties of the quantum wire in the ion-exchanged M+-ETS10, model II.

M-ETS10	Na	NaK	K	NaCa	Ca	NaAg	Ag	NaAu	Au	NaZn	Zn	NaRu	Ru
O1-Ti1	1.79	1.78	1.76	1.91	1.89	1.79	1.81	1.77	1.81	1.83	1.78	1.91	1.91
O2-Ti1	1.96	1.97	1.97	1.83	1.89	1.95	1.98	1.92	2.22	1.92	1.98	1.93	2.09
O2-Ti2	1.79	1.78	1.76	1.91	1.89	1.79	1.80	1.81	1.81	1.82	1.81	1.84	2.01
O3-Ti2	1.96	1.96	1.97	1.86	1.89	1.96	1.94	2.03	2.07	1.95	1.95	1.95	1.97
O3-Ti3	1.79	1.79	1.76	1.86	1.89	1.79	1.80	1.79	1.82	1.79	1.82	1.84	2.05
O4-Ti3	1.96	1.94	1.97	1.91	1.89	1.96	1.97	2.06	2.29	1.98	1.99	1.95	1.97
O4-Ti4	1.79	1.80	1.76	1.83	1.89	1.78	1.80	1.77	1.85	1.78	1.82	1.84	2.10
O1-Ti1-O2	180	179	178	172	180	174	179	139	175	168	177	158	145
Ti1-O2-Ti2	165	166	167	164	159	164	158	152	149	160	163	173	167
O2-Ti2-O3	179	178	178	179	180	178	156	177	125	178	159	179	168
Ti2-O3-Ti3	165	163	166	163	158	162	167	175	126	161	170	170	158
O3-Ti3-O4	179	178	179	179	180	179	176	175	160	179	169	177	170
Ti3-O4-Ti4	165	166	167	162	159	166	165	165	137	161	156	168	156

Table3.6: Löwdin charges for selected atoms in the fully exchanged M_{q+}-ETS10, model II (M=Na,K,Ca,Ag,Zn,Ru, and Au). Values are in unit of |e|.

Atoms	Na-ETS10	K-ETS10	Ca-ETS10	Ag-ETS10	Au-ETS10	Zn-ETS10	Ru-ETS10
Ti	1.63	1.73	1.34	1.62, 1.64	1.68, 1.74	1.61	1.57, 1.60
O_{ap}	-0.77	-0.70, -0.94	-0.75	-0.75	-0.58, -0.60	-0.72, -0.78	-0.44, -0.57
O_{eq}	-0.88	-0.85,-0.86	-0.80,-0.81	-0.85,-0.88	-0.68,-0.76	-0.80,-0.94	-0.57,-0.69
Orest	-0.80	-0.79,-0.82	-0.80,-0.81	-0.80,-0.83	-0.69,-0.81	-0.80,-0.84	-0.68,-0.81
M	0.77,0.82	0.41,0.57	0.71,0.82	0.71,0.73	-0.01,0.09	0.04,1.49	0.01,-0.33
Si_{eq}	1.76	1.78	1.76	1.75,1.77	1.79	1.77,1.79	1.78
Si_{frame1}	1.58	1.58	1.56	1.58	1.59	1.58	1.59
Si_{frame2}	1.28	1.30	1.24	1.29	1.28	1.25	1.30

When only 1/8 of the Na^+ cations are exchanged, the sites of the new host species are similar to the one obtained in the case of full exchange, and examined above. After geometry optimizations, the positions of the K, Ca, Ag, and Au species converge to nearly the same position characterizing the Na cations of the sodium form ETS-10 model II, which can be seen in the Fig. 3.13-3.18 and Fig. 3.5. The species acquire a charge of 0.72 $|e|$ for Zn exchanged case, which is nearly half of the partial charge of the Zn atoms located in the vicinity of the quantum wire in the fully-exchanged sample. This explains why the Zn atoms are not expelled from the region of the quantum-wire when only a partial exchange takes place. Moreover, the location of the Zn cations do not differ substantially from those of the remaining Na cations. In the case of Au and Ru, their presence again cause a sizeable deviation of the geometrical parameters of the TiO_6 units from those of the sodium form, as can be seen from the results collected in Table 3.5. From the results of Table 3.7, we conclude that the extraframework atoms acquire a small negative charge of -0.11 and -0.22 $|e|$ for Au and Ru respectively, so that the sizeable perturbation of the quantum wire caused by their presence can be related to steric effects due to the increased ionic radius.

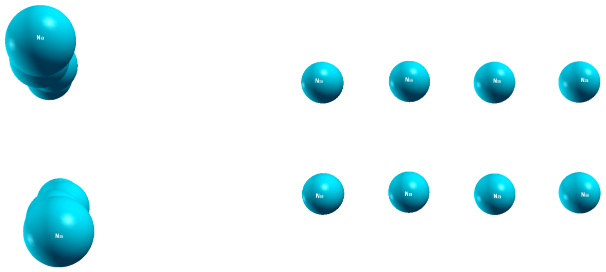

Figure 3.6: Cation Sites Na-ETS-10

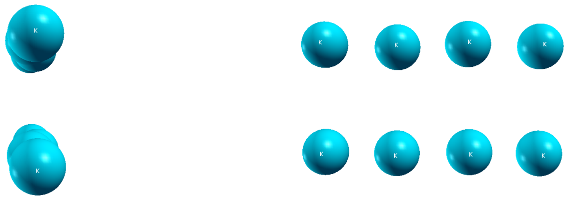

Figure 3.7: Cation Sites K-ETS-10

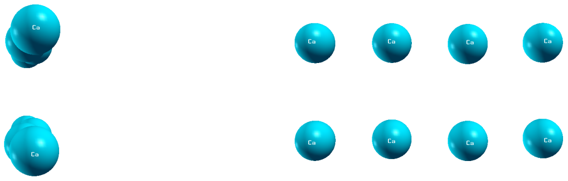

Figure 3.8: Cation Sites Ca-ETS-10

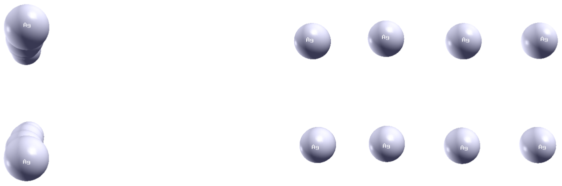

Figure 3.9: Cation Sites Ag-ETS-10

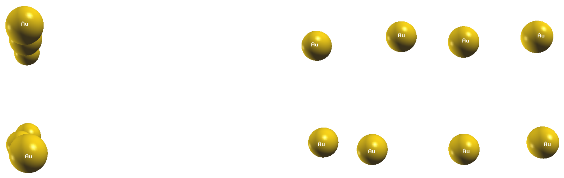

Figure 3.10: Cation Sites Au-ETS-10

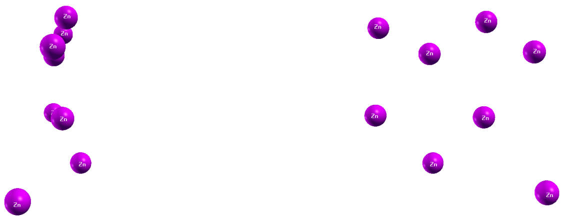

Figure 3.11: Cation Sites Zn-ETS-10

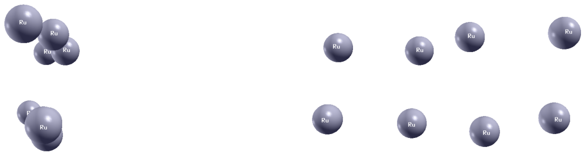

Figure 3.12: Cation Sites Ru-ETS-10

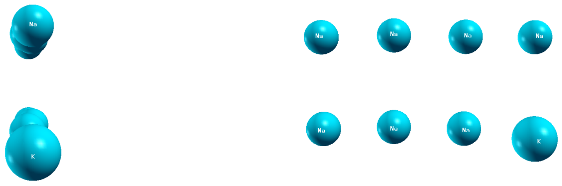

Figure 3.13: Cation Sites [Na,K]-ETS-10

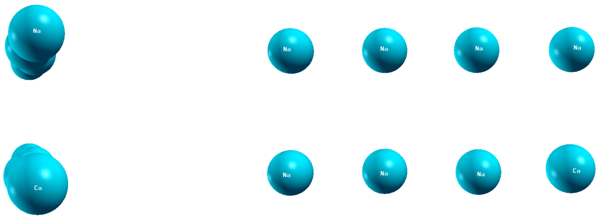

Figure 3.14: Cation Sites [Na,Ca]-ETS-10

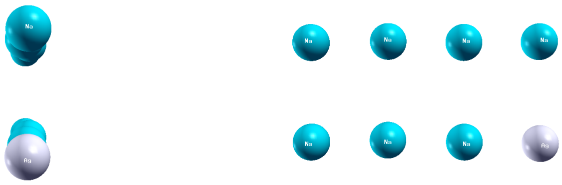

Figure 3.15: Cation Sites [Na,Ag]-ETS-10

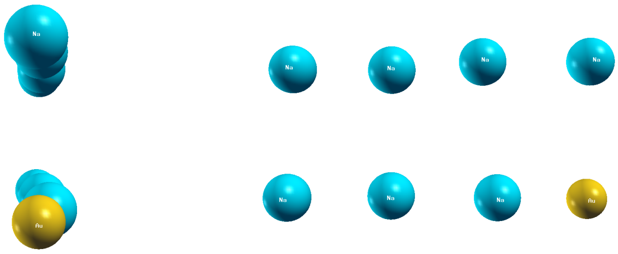

Figure 3.16: Cation Sites [Na,Au]-ETS-10

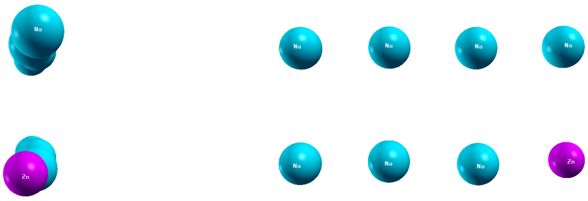

Figure 3.17: Cation Sites [Na,Zn]-ETS-10

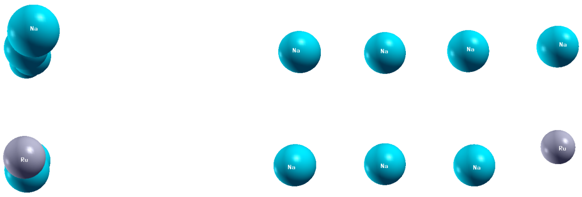

Figure 3.18: Cation Sites [Na,Ru]-ETS-10

Table3.7: Löwdin charges for selected atoms in the partially exchanged [Na,M+]-ETS10, model II. Values are in unit of |e|.

Atoms	NaK-ETS10	NaCa-ETS10	NaAg-ETS10	NaAu-ETS10	NaZn-ETS10	NaRu-ETS10
Ti	1.63,1.67	1.59,1.61	1.63,1.64	1.61,1.64	1.63, 1.65	1.62,1.64
O_{ap}	-0.73,-0.78	-0.78, -0.80	-0.75	-0.77,-0.84	-0.76, -0.78	-0.78, -0.80
O_{eq}	-0.86,-0.87	-0.85,-0.86	-0.86,-0.87	-0.85,-0.93	-0.77,-0.81	-0.74,-0.77
Orest	-0.81,-0.82	-0.80	-0.80,-0.81	-0.81,-0.82	-0.81,-0.82	-0.81,-0.82
M	0.38	0.91	0.73	0.98	-0.12	-0.22
Na	0.77	0.77	0.77	0.77	0.79	0.77
Si_{frame1}	1.57	1.58	1.58	1.58	1.58	1.58

Let us look in more detail into the structural deformations on the ETS-10 framework caused by the cation exchange. With reference to the data reported in Table 3.5 we conclude that the presence of two inequivalent Ti–O bonds along the quantum wire, which characterize both models with the sodium counterions, is conserved upon cation exchange (both in the partial and full cases), the only exception being when Ca atoms replace all sodium counterions inside the framework. The asymmetry between the two Ti–O_{ap} bond lenghts is maximum for Au (full exchange), with a largest difference of 0.47 Å or 25% of a Ti–O bond distance. More specifically, the partial and full ion-exchange of the Na^+ counterions with K of Ag ions does not affect the geometrical parameters of the TiO_6 moiety, in agreement with the experiment **[32]**. Similar conclusions also apply for Zn. In the latter case it is however interesting to observe that geometrical changes upon ion exchange are more pronounced when only 1/8 of the Na^+ sites are occupied by Zn, and this can be understood from the discussion above since half of the Zn atoms are localized far away from the wire upon full ion exchange. In the case of Ca, the asymmetry between the two inequivalent Ti–O_{ap} bond lenghts of the TiO_6 unit is already strongly reduced when only 1/8 of the Na^+ sites are occupied by Ca, and completely disappears upon full exchange of the sodium counterions with Ca. Taking the fact that the asymmetry in the Ti-O bonds of the wire can be considered to show the characteristic geometry of quantum wire. The asymmetry in the Ti–O bonds of the wire is pronounced noticeably for (Na,Au) ETS-10, Au-ETS-10 and Ru ETS-10 models, and it is less pronounced in the (Na, Ru)-ETS10 system, and disappears for the Ti center closer to the Ru ion. These results suggest that Au and Ru ion-exchange leads to the most noticable structural deformation in the wire.

We now turn our attention to the trend in the partial charges, reported in Table 3.6 for the case of full exchange, and Table 3.7 for the 1/8 ion exchange. An exchange of 1/8 of the sodium ions with K^+ ions does not have a noticeable effect on the charge density distribution of the TiO_6 unit and of the remaining Na^+ ions and the O atoms of the insulating silica matrix, meaning that the interaction of the sodium counterions and the ETS-10 framework is not affected by this substitution. The partial positive charge on the potassium is much lower than on Na, of approximately 0.36 $|e|$ and the remaining positive charge is equally distributed between the Si atoms of the matrix. Reason of this significant charge difference of potassium and sodium can be speculates as the significant difference of atomic and ionic radius between potassium and sodium, presented in Table 3.4. Confining effects of frame atoms and distance between secondary ion affect the cation and electrostatic forces. In the Table 3.3 and Table 3.8, sodium and potassium models can be compared. Sodium atoms converge to 2.4 Å distance from O_{ap} atoms and 3.05 Å from Ti atoms, while potassium atoms 2.83 Å from O_{ap} and 3.45 Å from Ti atoms. Divergence from quantum wire ended up with decrease of effective radius of charge distribution of quantum wire, which is the only charge transfer possibility for cations. Divergence could be caused by the only significant difference of atom sizes which prevents potassium atoms to get closer to quantum wire. Similar conclusions can be reached after examination of the results obtained for partial exchange with either Ca or Ag ions. Here however both counterions assume a partial positive charge similar (Ag) or higher (Ca) than that of the sodium counterions. The situation is somewhat different when 1/8 of the Na^+ sites are occupied by either Zn, Au or Ru. In all these cases the transition metal is only slightly negatively charged. The O atoms of the framework and of the TiO_6 unit are characterized by similar degrees of electron excess, varying in the range -0.74– -0.93 $|e|$. The charge density on the remaining sodium cations is not appreciably altered upon partial exchange.

When all Na ions are exchanged with potassium ions, the only noticeable differences in the electron density distributions is an increase of the partial positive charge on the Ti atoms by about 0.10 $|e|$ while the positive charge on the potassium ions is about 0.2–0.3 $|e|$ lower than the one on the sodium ions. In the case of the Ca form, the partial charge on the counterions is comparable to that characterizing the Na ions; we however notice that the partial charge on the Ti atoms decreases by about 0.3 $|e|$. In the case of Ag the atomic charge distribution resembles very closely the one of the sodium form. Finally, for both Au and Ru exchange, the extraframework atoms are either neutral (Au) or both neutral and negatively charged (Ru). The case of Zn has been highlighted above; the Zn atom located away from the quantum wire is neutral, while the ion interacting with the wire is positively charged (1.49 $|e|$).

3.1.2.1 K-ETS-10 Computations

K-ETS-10 models are presented in Fig. 3.19, 3.21, 3.23. Potassium comes with as-synthesized form in the ETS-10, regarding that strong distortions are not expected from K-ETS-10 computations. Similar to Na-ETS-10 models, three different sized DFT models are employed as computation agent. 132-Atom, 52-Atoms and 24-Atom models are compared. Selected results are listed in the Table 3.8. As expected K-ETS-10 Model I and Model II models converged to approximately same geometry with Na-ETS-10 models. Model I and Model II of K-ETS-10 are very similar and selected geometries are represented in Table 3.8. Maximum bond length difference between Model I and Model II is 0.16 Å and maximum angle difference is 6°. Model III is also very similar to Model I and Model II. General geometric parameters are very close to corresponding parameters. Maximum bond length difference computed is about 0.45 Å and maximum bond angle difference computed is 27. Relatively larger difference in Model III can be explained by the suppressing effect of the frame unit atoms on the potassium atoms. Charge balancing atoms, which is potassium atoms for K-ETS-10 model, bind with relatively weaker forces. Confining effect of the framework atoms suppress the more freely moving charge balancing atoms. Second important difference of Model III is calcium atoms create a zigzag pattern unlike the linear Model I and Model II cases and Na-ETS-10 models. Potassium atom has an electronegativity of 0.82 which is smaller than sodium, 0.93 and potassium has an ionic size of 1.37 Å which larger than sodium, 1.00. Comparison of the atoms can be seen in the Table 3.4. Significant difference between sodium and potassium atoms is ionic radius. This result is also consistent with our simulation results due to extreme sensitivity of the ETS-10 structure. Ionic radius difference of sodium and potassium atoms could cause these convergence difference. This new distortion can be explained by relatively stronger interaction caused by larger radius of potassium atoms and suppressing forces created by oxygen and silicon atoms in the side walls of framework. Effect of the ionic radius is also observed in the partial charge computations. Partial charge analysis showed that potassium atoms in the K-ETS-10 cases charged with 0.47e, while sodium atoms charged with 0.77e, which can be seen in the Table 3.6. Significant difference between sodium and potassium charges are explained as large difference between ionic radius rather than slight difference between electronegativities. Computed band gap energies of the models are 3.1859 eV for Model I and 3.3843 eV for Model II. Even though underestimation of the DFT analysis for the electronic structure exists, results are well correspondent with the experimental result of ETS-10 4.03 [60] and Na-ETS-10 models(Model I 3.26 eV, Model II 3.34 eV).

Table3.8: Selected structural parameters of the optimized structures of the three models of Potassium ETS-10. Represented bond distance units are Å.

	Model I	Model II	Model III
Ti1-Ti2	3.75	3.71	3.75
Ti2-O2	1.76	1.76	1.76
Ti2-O3	2.00	1.97	2.17
K-O2	2.80	2.83	2.62
Ti1-O2	2.00	1.97	2.27
Ti1-O1	1.76	1.76	1.76
Ti3-O3	2.00	1.97	2.17
Ti3-O4	1.76	1.76	1.76
Ti2-O5	2.04	2.05	1.97
Ti1-O6	2.04	2.03	1.97
Ti3-O7	2.04	2.02	1.97
Ti2-O6	4.45	4.29	4.74
Ti1-K	3.42	3.45	3.42
Ti1-O2-Ti2	171°	167°	144°
O2-Ti2-O3	179°	178°	179°
O2-Ti2-O5	87°	93°	84°

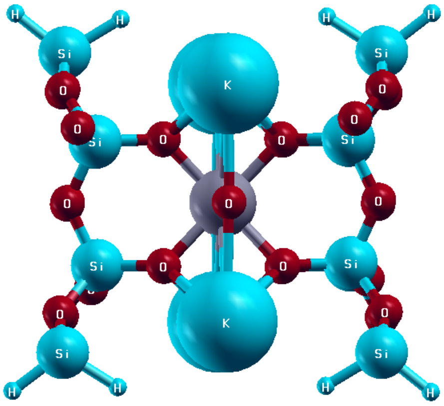

Figure 3.19: K-ETS-10 Model I Front

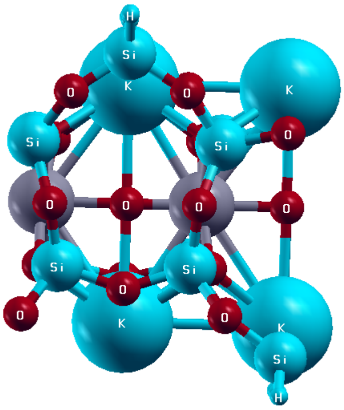

Figure 3.20: K-ETS-10 Model I Side

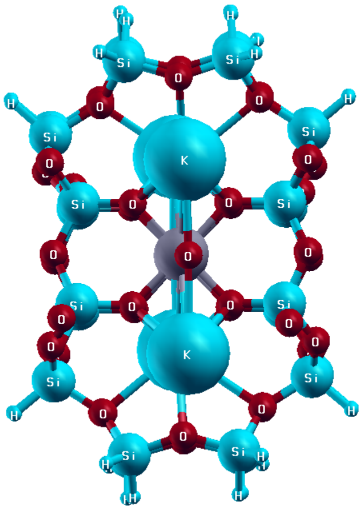

Figure 3.21: K-ETS-10 Model II Front

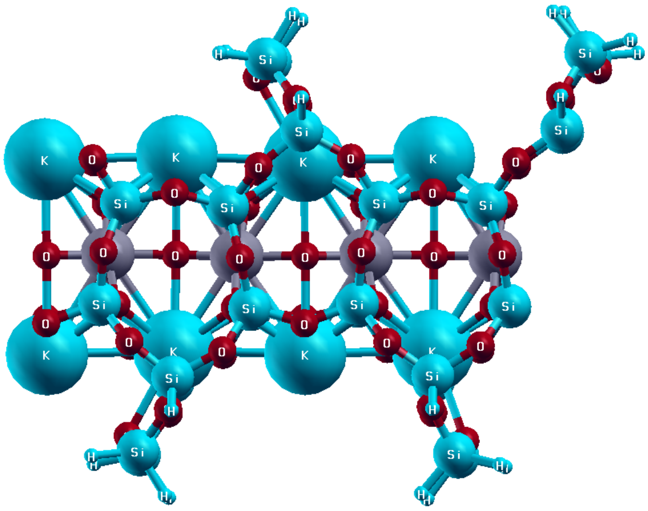

Figure 3.22: K-ETS-10 Model II Side

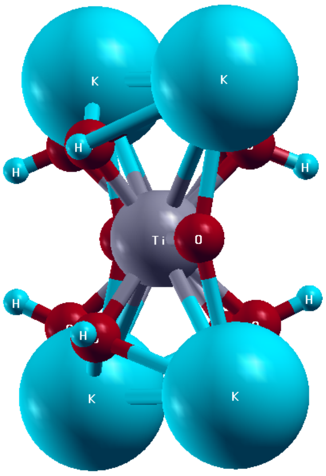

Figure 3.23: K-ETS-10 Model III Front

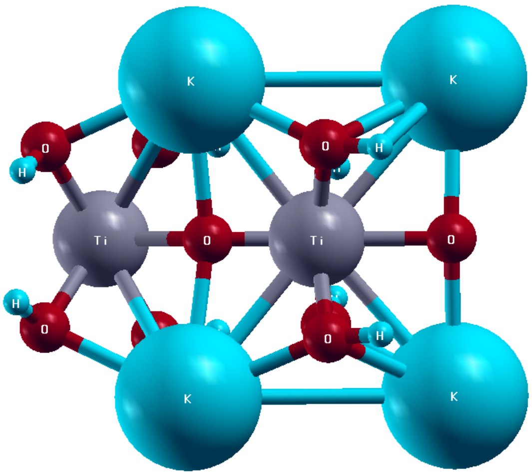

Figure 3.24: K-ETS-10 Model III Side

3.1.2.2 Ca-ETS-10 Computations

Fully exchanged calcium ETS-10 models are computed with three different models similar to Na-ETS-10 case. Model I, Model II and Model III have 52, 132 and 24 atoms respectively. Electronegativity, valence electron number and ionic radius are major key factors which are affecting the structural distortion caused in ETS-10 structure. Calcium atom has an electronegativity of 1.00 which is slightly higher than sodium 0.93 and potassium 0.82. Another important thing which is observed and discussed in the potassium exchanged ETS-10 models is atomic/ionic radius. Calcium has an ionic radius of 1.06 Å which is very close to sodium atoms. In the calcium case observed and computed differences are expected as contribution of the valence electron number and electronegativity difference. Calcium atoms are charged with 0.71 which is very close to sodium atoms of 0.77. Slightly less charged calcium atoms can be explained by slightly larger electronegativity. Calcium atoms have two valence electrons unlike one electron of sodium and potassium atoms. The most surprising result in the geometric parameters observed in the calcium exchanged ETS-10 models is asymmetric bond character of the titania quantum wire seems to be vanished. Quantum wire structure converged to a complete symmetric Ti-O bond which can be seen in the Table 3.5. Model I, Model II and Model III computations show that results converge to same geometric parameters presented in Table 3.9. Band gap calculations of the calcium ETS-10 model has a surprising result. Even though band gap calculations of the DFT computations underestimate the electronic structures of the semiconductors, Ca-ETS-10 presented a shifted Fermi level to conduction band. Resulted band gap energy for the Ca-ETS-10 Model I is 0.1993 eV.

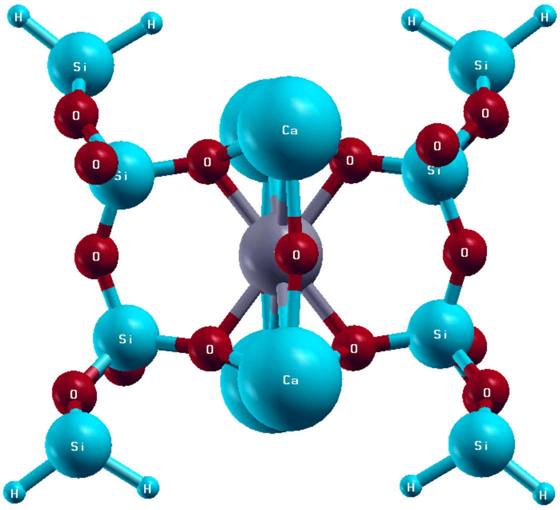

Figure 3.25: Ca-ETS-10 Model I Front

Table3.9: Selected structural parameters of the optimized structures of the three models of Calcium ETS-10. Represented bond distance units are Å.

	Model I	Model II	Model III
Ti1-Ti2	3.75	3.72	3.75
Ti2-O2	1.90	1.89	1.90
Ti2-O3	1.89	1.89	1.88
Ca-O2	2.32	2.31	2.13
Ti1-O2	1.89	1.89	1.88
Ti1-O1	1.90	1.89	1.90
Ti3-O3	1.90	1.89	1.90
Ti3-O4	1.89	1.89	1.88
Ti2-O5	2.19	2.22	2.25
Ti1-O6	2.20	2.21	2.29
Ti3-O7	2.20	2.20	2.29
Ti2-O6	4.48	4.50	4.54
Ti1-Ca	2.96	2.97	2.84
Ti1-O2-Ti2	163°	159°	165°
O2-Ti2-O3	179°	180°	179°
O2-Ti2-O5	91°	92°	95°

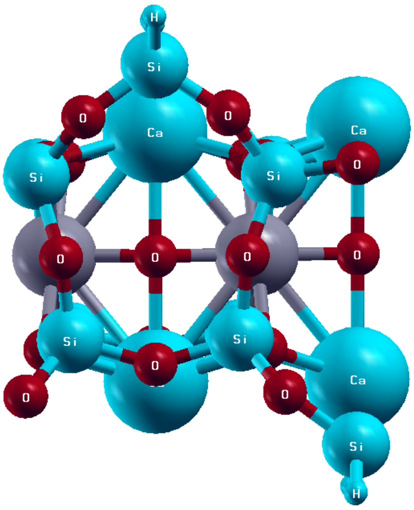

Figure 3.26: Ca-ETS-10 Model I Side

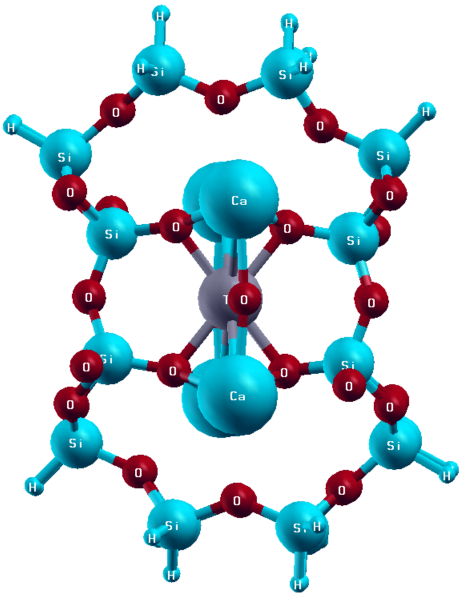

Figure 3.27: Ca-ETS-10 Model II Front

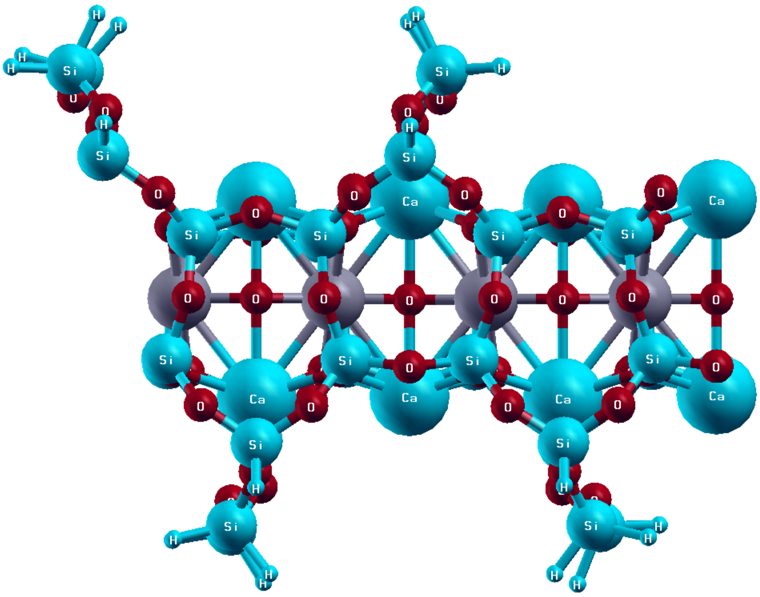

Figure 3.28: Ca-ETS-10 Model II Side

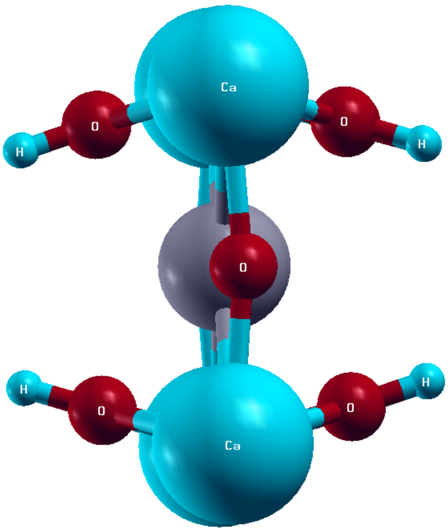

Figure 3.29: Ca-ETS-10 Model III Front

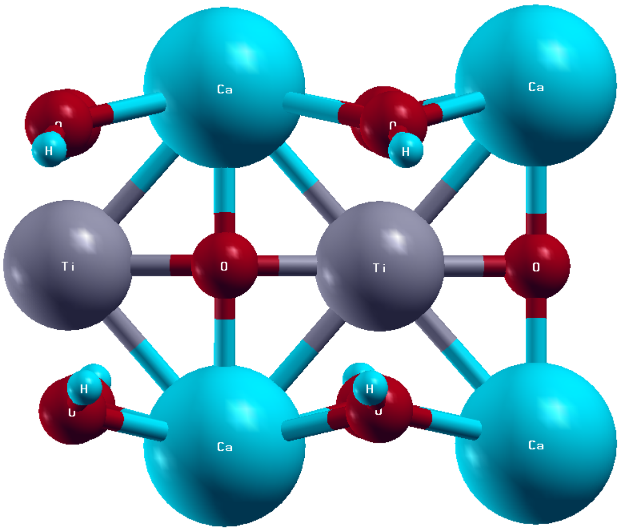

Figure 3.30: Ca-ETS-10 Model III Side

3.1.2.3 Ag-ETS-10 Computations

Three different models were employed and computed for silver ETS-10 case, Model I, Model II and Model III. Observed data showed that silver acts very similar to sodium and potassium atoms of ETS-10 respect to experimentally observed data Fig. B.9. Silver has an ionic radius of 1.00 Å which is same with sodium. Outermost electron number of silver can be accepted as one which is also same with sodium and potassium. Regarding strong correlation between chemical properties of sodium, potassium and silver, no serious difference in the geometrical structure is expected. Electronegativity of silver is significantly different than sodium which 1.93 for silver and 0.93 for sodium. Selected geometric parameters of Model I, Model II and Model III are presented in Table 3.10. Maximum bond length difference is observed 0.15 Å between models and maximum bond angle difference is 20. Similar geometric parameters with sodium and potassium cases and similar partial charge analysis computations, which is presented in Table 3.6, showed that silver exchanged ETS-10 model is very stable. Band gap calculations of silver ETS-10 converged to an energy of 2.2788 eV for model I and 2.3764 eV for model II. Large difference of band gap energy between potassium , 3.1859 eV model I, 3.3843 eV model II, and sodium, 3.26 eV model I and 3.34 model II, can be speculated as contribution of $4d$ orbital electrons of silver atom and large electronegativity.

Table3.10: Selected structural parameters of the optimized structures of the three models of Silver ETS-10. Represented bond distance units are Å.

	Model I	Model II	Model III
Ti1-Ti2	3.75	3.71	3.82
Ti2-O2	1.78	1.80	1.82
Ti2-O3	1.98	1.94	2.04
Ag-O2	2.55	2.62	2.66
Ti1-O2	1.98	1.98	2.00
Ti1-O1	1.78	1.81	1.81
Ti3-O3	1.78	1.81	1.81
Ti3-O4	1.98	1.97	2.00
Ti2-O5	2.03	1.92	1.88
Ti1-O6	2.04	2.00	1.94
Ti3-O7	2.04	2.02	1.94
Ti2-O6	4.45	4.37	4.53
Ti1-Ag	3.13	3.18	3.25
Ti1-O2-Ti2	171°	158°	178°
O2-Ti2-O3	179°	156°	159°
O2-Ti2-O5	86°	101°	99°

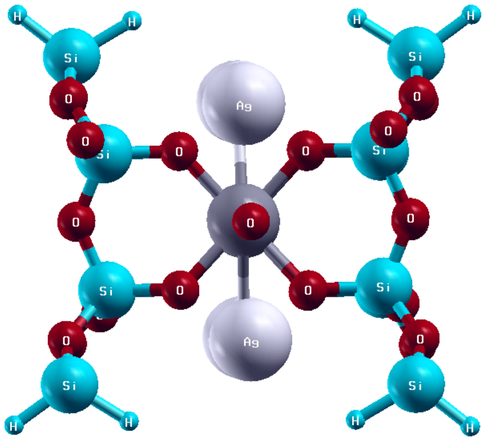

Figure 3.31: Ag-ETS-10 Model I Front

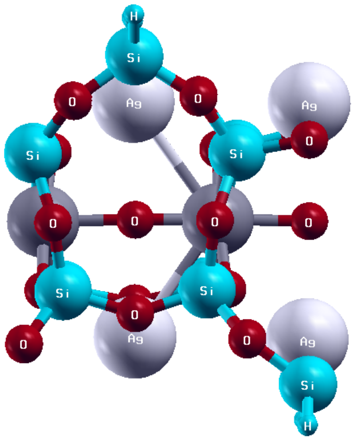

Figure 3.32: Ag-ETS-10 Model I Side

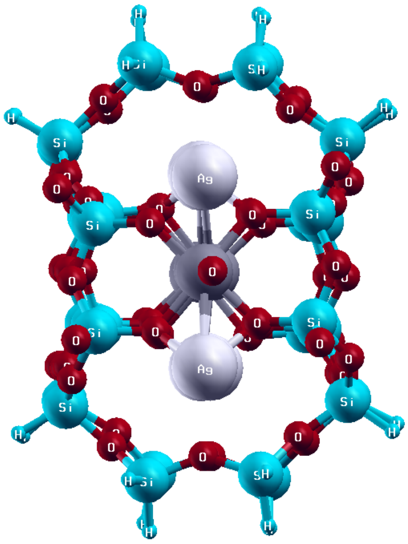

Figure 3.33: Ag-ETS-10 Model II Front

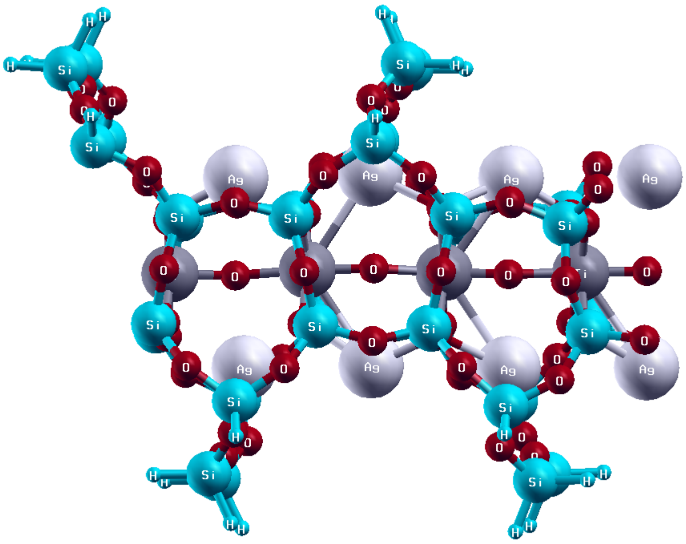

Figure 3.34: Ag-ETS-10 Model II Side

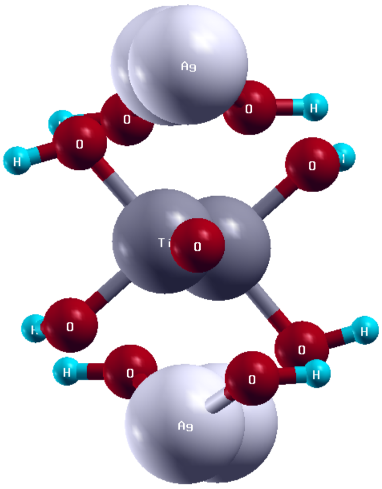

Figure 3.35: Ag-ETS-10 Model III Front

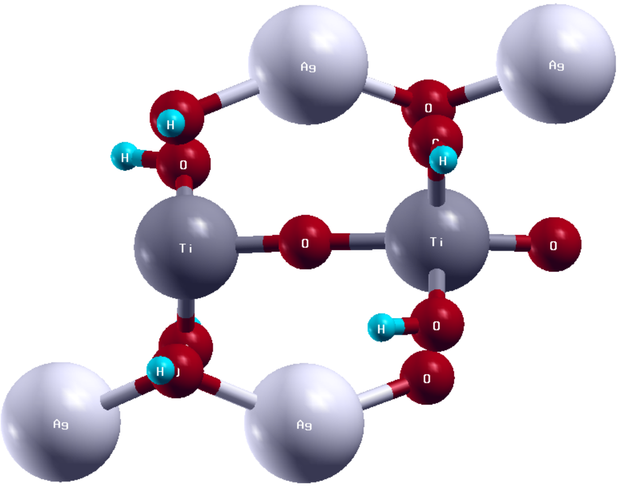

Figure 3.36: Ag-ETS-10 Model III Side

3.1.2.4 Zn-ETS-10 Computations

Zinc computations are also completed with three different models, model I, model II and model III. Zinc atom has an ionic radius of 0.68 Å, which is quiet small respect to sodium and potassium atoms. Optimized distance of zinc atoms are largest in the model III. Lack of frame atoms in the model III created more freely moving area for zinc atoms. Due to large electronegativity, 1.65, small ionic radius 0.68 Å, and two valence electron number of zinc atom geometric structure of Zn-ETS-10 converged to one zinc atom for one titanium atom in the structure instead of two cation per one titanium atom. Calcium also has two valence electrons however larger ionic radius calcium inhibits it from approaching closer to quantum wire and substitute remaining valence electron of +1 charged calcium atom. Small ionic radius of zinc atom unlike the calcium enables it to get closer to quantum wire and substitute valence electrons of $4s$ orbitals. Table 3.11 presented that maximum bond length difference between models is 0.20Å and angle difference 12. Zinc models also presented asymmetric one short and one long Ti-O bonds similar to sodium and potassium models. In Table 3.11 it can be seen that there exists one very long distance between Oap atom an zinc and one relatively short distance. Partial charge analysis showed that zinc atoms that stayed interacted with quantum wire and have shorter bond lengths with Oap atom have a partial charge of +1.49, while zinc atoms that move away from the structure stay uncharged with +0.04 in Table 3.6. This phenomena can be explained with two valence electron number of $4s$ orbitals of zinc atom and smaller ionic radius as mentioned above. Band gap computations presented that model I has a band gap of 0.4241 eV and model II has 1.8737 eV.

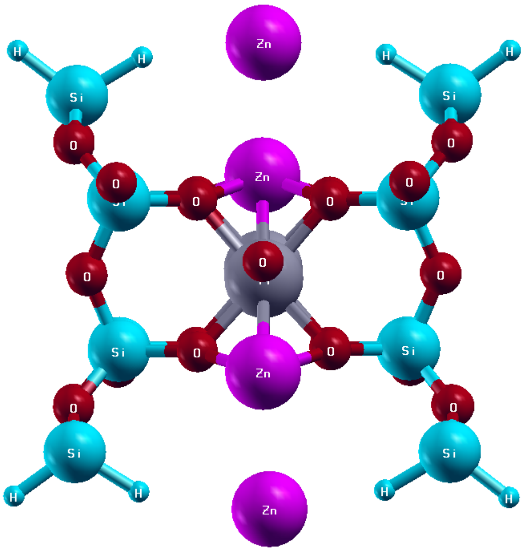

Figure 3.37: Zn-ETS-10 Model I Front

Table3.11: Selected structural parameters of the optimized structures of the three models of Zinc ETS-10. Represented bond distance units are Å.

	Model I	Model II	Model III
Ti1-Ti2	3.75	3.75	3.78
Ti2-O2	2.02	1.94	2.12
Ti2-O3	1.77	1.81	1.75
Zn-O2	2.20, 4.43	2.26, 4.28	2.38,3.59
Ti1-O2	1.76	1.77	1.74
Ti1-O1	2.02	1.98	2.11
Ti3-O3	2.02	1.98	2.11
Ti3-O4	1.76	1.81	1.74
Ti2-O5	1.99	2.18	1.90
Ti1-O6	2.05	2.03	2.00
Ti3-O7	2.05	2.03	2.00
Ti2-O6	4.06	4.31	4.94
Ti1-Zn	2.67, 4.84	2.78, 4.77	2.77, 4.34
Ti1-O2-Ti2	165°	164°	156°
O2-Ti2-O3	175°	160°	163°
O2-Ti2-O5	85°	87°	91°

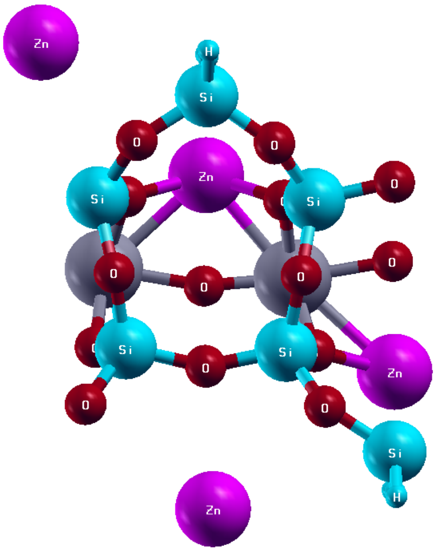

Figure 3.38: Zn-ETS-10 Model I Side

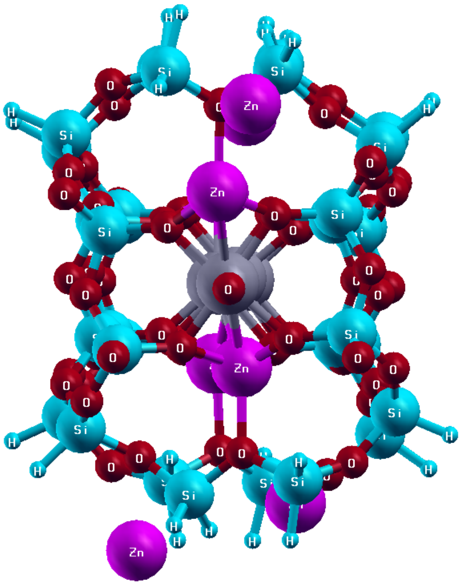

Figure 3.39: Zn-ETS-10 Model II Front

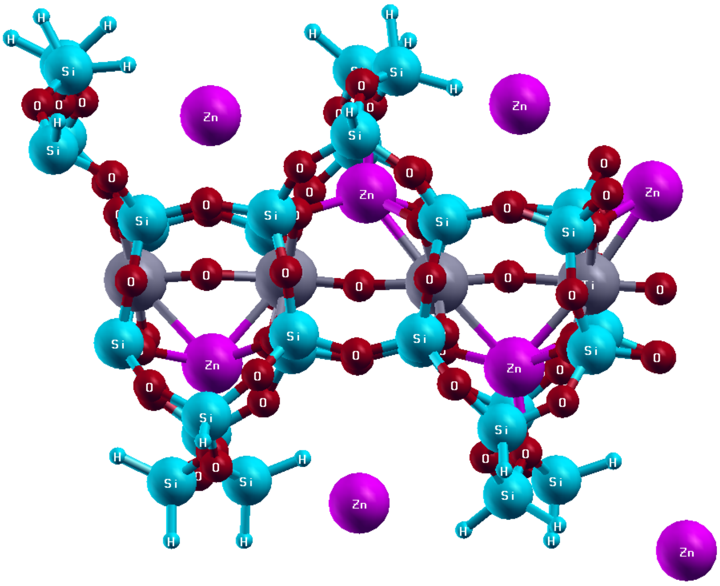

Figure 3.40: Zn-ETS-10 Model II Side

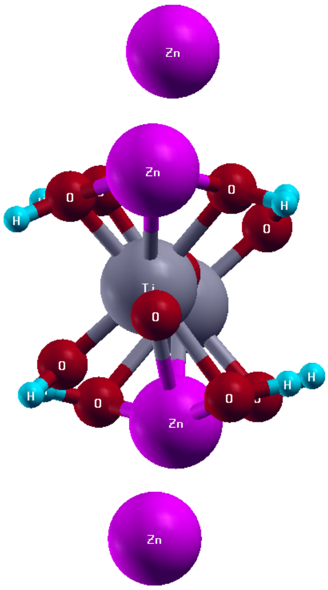

Figure 3.41: Zn-ETS-10 Model III Front

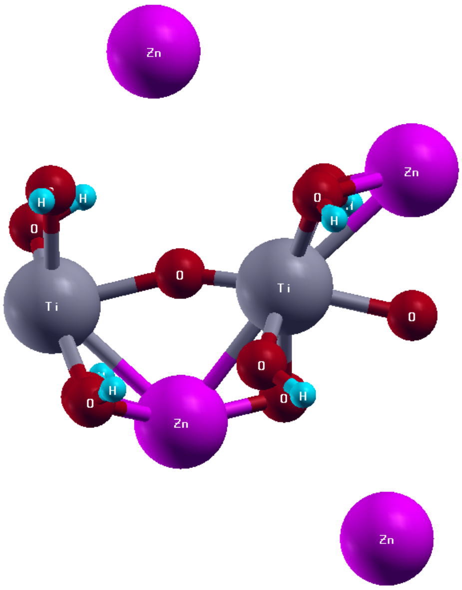

Figure 3.42: Zn-ETS-10 Model III Side

3.1.2.5 Au-ETS-10 Computations

Gold exchanged ETS-10 computations are completed with three different models, model I, model II and model III. Gold has 2.54 electronegativity which is higher than all other selected exchangeable cations. Result of high electronegativity, gold atoms in the system stay uncharged. Unbalanced electron distribution around the quantum wire with lack of charged cations, distorted the material symmetry. Compare to sodium and potassium cases asymmetric bond character of quantum wire with one short and one long Ti-O bond, seems to be preserved. Difference between short and long Ti-O bond enlarged. In the sodium and potassium cases this difference 0.17 Å while for Au-ETS-10 it becomes 0.47 Å. Another important result is characteristic Ti-Ti distance of ETS-10 seems to be affected by the addition of the gold atoms. Ti-Ti distance is 3.75 for all the other ion exchanged models, however for gold case this becomes about 3.93 for model I, 3.90 for model II and 4.00 for model III, which can be seen in Table 3.12 . This distortion shows that ETS-10 structure affected by the gold atoms. In Fig. 3.47 and Fig. 3.48 it can be easily seen that gold atoms distorted oxygen atoms and result of that there is no stable unit cell network any more. In the Fig. 3.31 it can be seen that addition of frame atoms confines unstable gold atoms. Distortion in the model I is significantly less than model III, yet equatorial oxygen atoms are highly affected by gold atoms. In the Fig. 3.33 and Fig. 3.34 distortion of the material network seems to be minimum relative to model I and model III. Equatorial oxygen atoms are observed to be affected the most again. Addition of remaining frame atoms has significant preserving effect on the ETS-10 unit. High valence electron number, very high electronegativity and significantly smaller atomic radius of gold atom of 1.37 Å, relative to 2.27 Å of potassium and 1.86 Å of sodium, make gold an unstable charge balancing agent. Result of these chemical properties of gold atom, it stayed uncharged in unit cell. Existence of highly reactive, uncharged atoms in material network affected band gap structure addition to structure. Computed band gap structure of Au-ETS-10 model I is 0.8991 eV and for model II 1.1373 eV.

Table3.12: Selected structural parameters of the optimized structures of the three models of Gold ETS-10. Represented bond distance units are Å.

	Model I	Model II	Model III
Ti1-Ti2	3.93	3.90	4.00
Ti2-O2	1.73	1.82	1.71
Ti2-O3	2.12	2.08	2.32
Au-O2	3.56,4.49	2.07,3.16	3.16,3.42
Ti1-O2	2.21	2.23	2.33
Ti1-O1	1.76	1.82	1.71
Ti3-O3	1.76	1.83	1.71
Ti3-O4	2.21	2.30	2.33
Ti2-O5	2.11	1.89	2.03
Ti1-O6	2.51	1.89	1.85
Ti3-O7	2.51	1.94	1.85
Ti2-O6	4.22	4.39	4.34
Ti1-Au	4.07,5.57	2.08,3.37	3.56,4.21
Ti1-O2-Ti2	173°	149°	163°
O2-Ti2-O3	143°	125°	137°
O2-Ti2-O5	96°	103°	100°

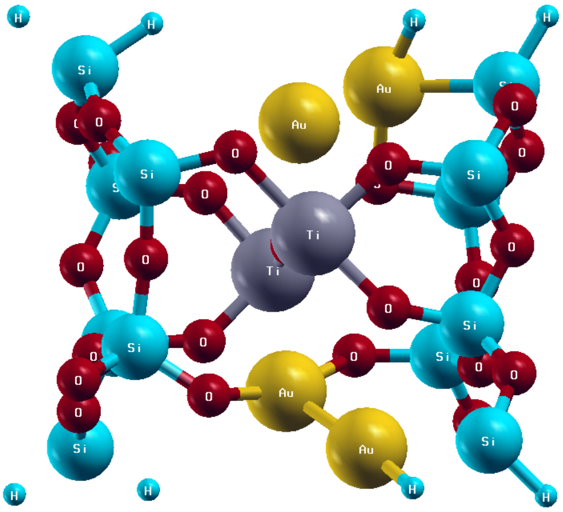

Figure 3.43: Au-ETS-10 Model I Front

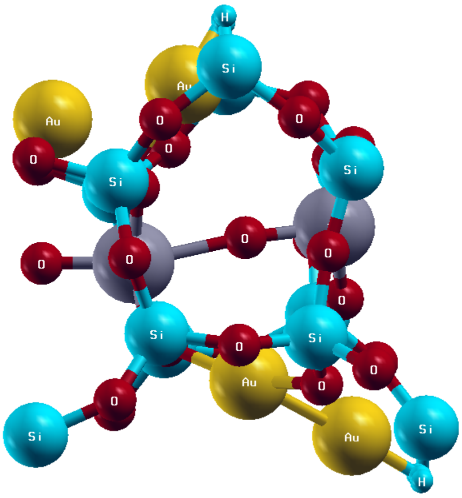

Figure 3.44: Au-ETS-10 Model I Side

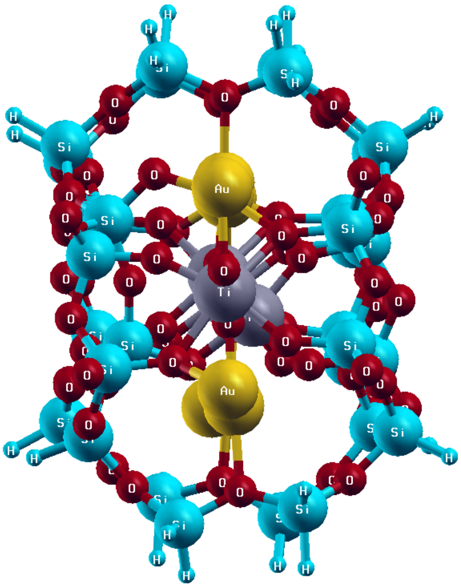

Figure 3.45: Au-ETS-10 Model II Front

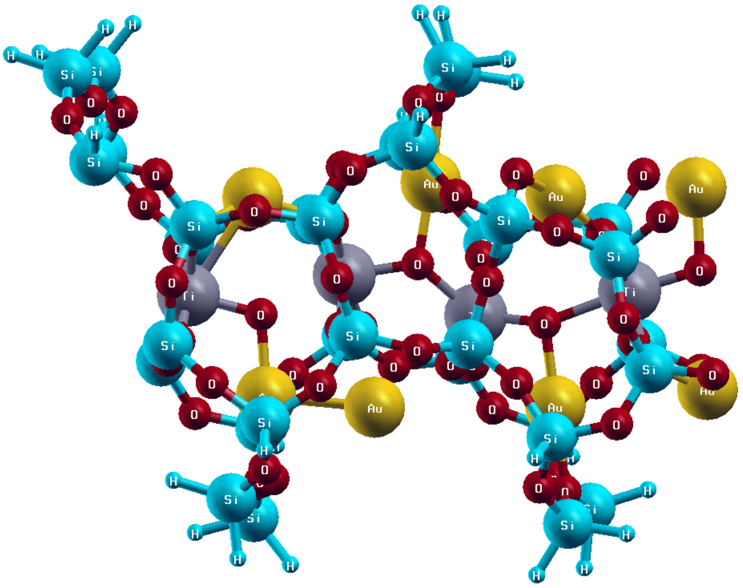

Figure 3.46: Au-ETS-10 Model II Side

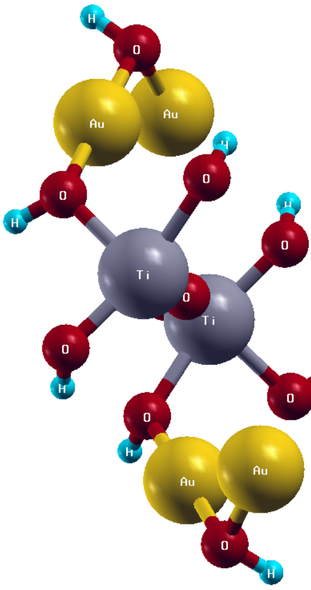

Figure 3.47: Au-ETS-10 Model III Front

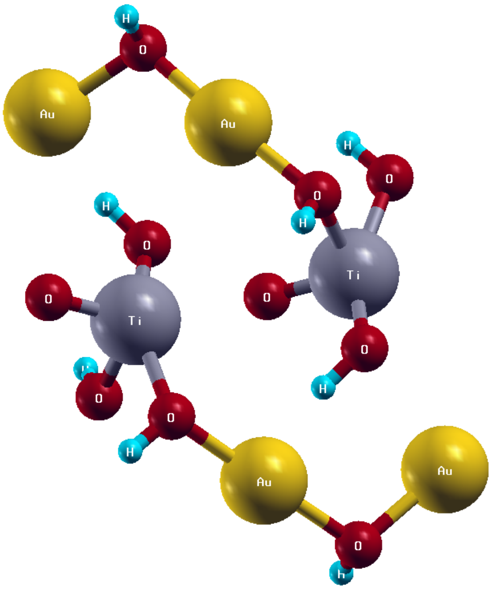

Figure 3.48: Au-ETS-10 Model III Side

3.1.2.6 Ru-ETS-10 Computations

Ruthenium exchanged ETS-10 structure is analysed with three different models also. Ruthenium has also very high electronegativity 2.2 and high valence electron number. Addition to that ruthenium atom has quiet small atomic and ionic radius which can be seen in the Table. 3.4. In the Table 3.13 it can be seen that Ti-Ti distance of 3.75 Å is preserved in the model III Ru-ETS-10 model but distortion exists in the model I and model II. In the Fig. 3.51 it can be seen that Si atoms in the framework significantly distorted by ruthenium atoms. More, periodic structure of the quantum wire no longer exists. In the Fig. 3.49 computation presented a less distorted framework nature, while variations in the quantum wire relative to sodium and potassium models still exist. The most interesting case is model III due to complete periodic convergence of Ru-ETS-10 model with lack of any frame atoms. This phenomena can be speculated by forces between ruthenium atoms, quantum wire and frame atoms become unbalanced with existing ETS-10 structure. This can also be verified from experimental raman results Fig. B.15 and phonon calculations. Raman results suggest that ruthenium exchanged ETS-10 model converge to unbalanced, distorted structure with lack of sharp peak at 724cm^{-1}. Band gap structure computations also point that distortion. Calculated band gap is 0.3261 eV for model II and there seems to be no band gap energy, metallic, for model I.

Table3.13: Selected structural parameters of the optimized structures of the three models of Ruthenium ETS-10. Represented bond distance units are Å.

	Model I	Model II	Model III
Ti1-Ti2	3.79	3.87	3.76
Ti2-O2	2.00	1.92	2.26
Ti2-O3	1.91	2.04	1.97
Ru-O2	2.12	2.07,2.68	2.08
Ti1-O2	1.90	2.02	1.97
Ti1-O1	2.00	1.91	2.25
Ti3-O3	2.00	2.08	2.25
Ti3-O4	1.90	1.96	1.97
Ti2-O5	2.29	2.04	2.19
Ti1-O6	2.08	1.98	2.19
Ti3-O7	2.08	2.08	2.19
Ti2-O6	4.77	4.19	4.50
Ti1-Ru	2.42	3.46	2.54
Ti1-O2-Ti2	153°	160°	125°
O2-Ti2-O3	162°	167°	174°
O2-Ti2-O5	81°	92°	99°

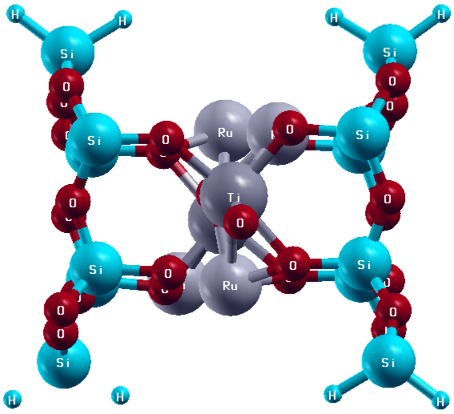

Figure 3.49: Ru-ETS-10 Model I Front

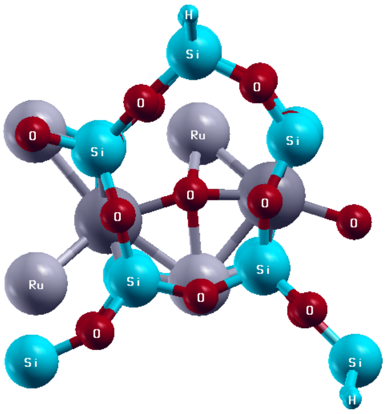

Figure 3.50: Ru-ETS-10 Model I Side

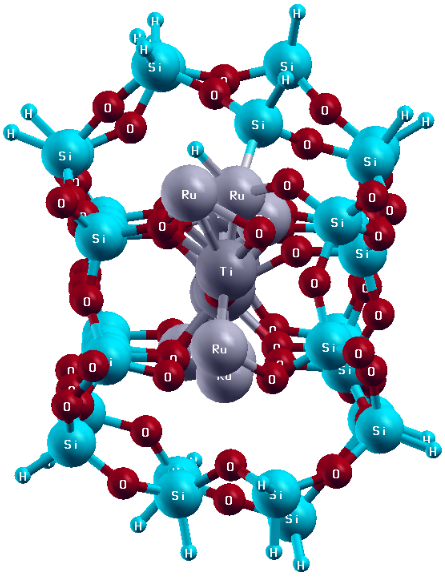

Figure 3.51: Ru-ETS-10 Model II Front

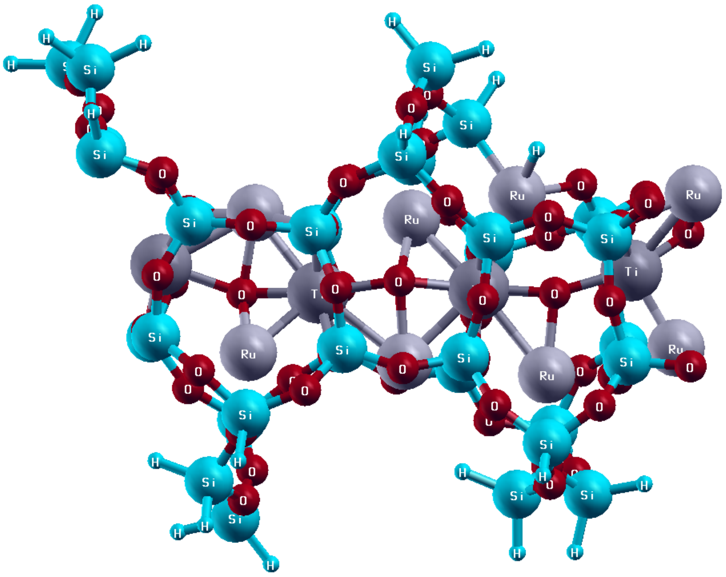

Figure 3.52: Ru-ETS-10 Model II Side

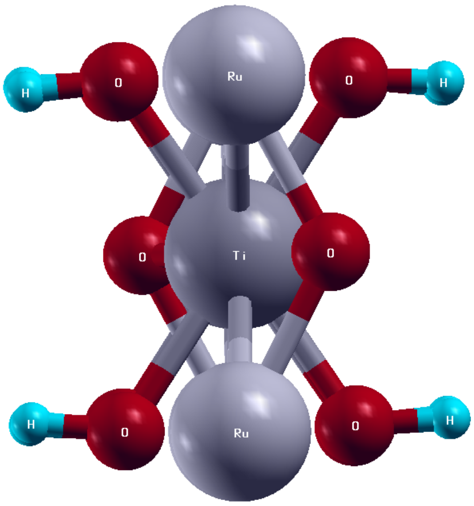

Figure 3.53: Ru-ETS-10 Model III Front

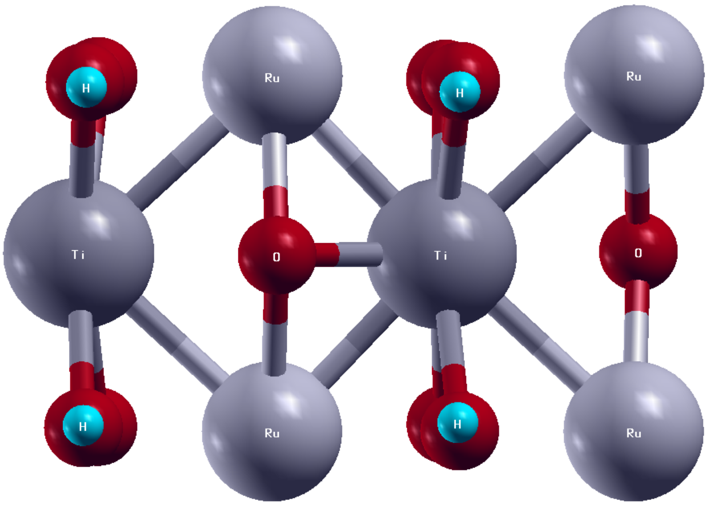

Figure 3.54: Ru-ETS-10 Model III Side

3.1.2.7 B-ETS-10 Computations

Boron has an electronegativity of 2.05, which can be seen in the table 3.14 and it has a small ionic and atomic radius of 0.41 Å, 0.85 Å similar to ruthenium. Boron has four valence electrons which is similar to ruthenium. Similar structural distortions exist in B-ETS-10 case due to correlations of chemical properties of boron and ruthenium. It can be seen in the Table 3.15 that Ti-Ti distance diverge from 3.75 to 4.03 Å. Oeq atoms, equatorial oxygen atoms also distort significantly can be seen in the Fig. 3.55 and Fig. 3.56. Periodicity of the unit cell is lost. Calculated band gap energy is 1.1027 eV for model I, which differ from the ruthenium exchanged ETS-10 model II.

Table3.14: Pauling (Allen) electronegativity (EN), atomic and ionic radius of the extra cations completed in this work work. Atomic and ionic radii are in Å.

Element	EN	atomic radius	ionic radius
B	2.04 (2.05)	0.85	(+4) 0.41
Cd	1.69 (-)	1.55	(+2) 1.09
Cu	1.90 (-)	1.35	(+1) 0.77, (+2) 0.73
Pb	1.65 (1.59)	1.80	(+2) 1.19, (+4) 0.77

Table3.15: Selected structural parameters of the optimized structures of the Model I of Boron ETS-10. Represented bond distance units are Å.

	Model I
Ti1-Ti2	4.03
Ti2-O2	1.99
Ti2-O3	2.08
B-O2	1.45,3.72
Ti1-O2	2.08
Ti1-O1	1.99
Ti3-O3	1.99
Ti3-O4	2.08
Ti2-O5	2.33
Ti1-O6	3.36
Ti3-O7	3.36
Ti2-O6	4.94
Ti1-B	2.37,5.50
Ti1-O2-Ti2	165°
O2-Ti2-O3	137°
O2-Ti2-O5	83°

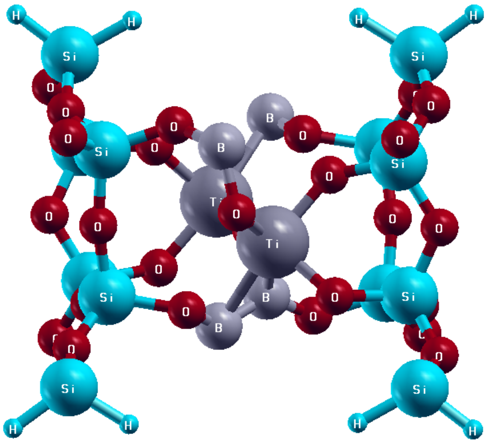

Figure 3.55: B-ETS-10 Model I Front

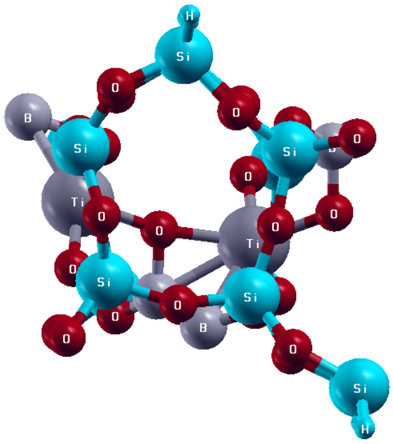

Figure 3.56: B-ETS-10 Model I Side

3.1.2.8 Cd-ETS-10 Computations

Cadmium has 1.69 Pauling scale electronegativity and atomic radius of 1.55 Å very similar to zinc. Ionic radius differs from zinc case. Cadmium exchanged ETS-10 structure computations showed that optimized coordinates of Cd-ETS-10 model I and Zn-ETS-10 model I is approximately same with 0.01 Å deviation. Ti-Ti distances stayed in expected ranges, equatorial oxygen atoms and quantum wire symmetry preserved which can be seen in the Table 3.16. In the Fig. 3.57 and Fig. 3.58 it can be seen that two of the cadmium ions pushed away from the system and remainin two of them balanced the excess charge come from titania chain. Results are very similar to zinc exchanged case. Calculated band gap structure of the Cd-ETS-10 model I is 0.3172 eV which is quiet similar to Zn-ETS-10 model I of 0.4241 eV.

Table3.16: Selected structural parameters of the optimized structures of the Model I of Cadmium ETS-10. Represented bond distance units are Å.

	Model I
Ti1-Ti2	3.74
Ti2-O2	1.76
Ti2-O3	2.01
Cd-O2	4.74,7.01
Ti1-O2	2.00
Ti1-O1	1.76
Ti3-O3	1.76
Ti3-O4	2.00
Ti2-O5	2.03
Ti1-O6	2.03
Ti3-O7	2.03
Ti2-O6	3.98
Ti1-Cd	2.97,4.72
Ti1-O2-Ti2	170°
O2-Ti2-O3	177°
O2-Ti2-O5	90°

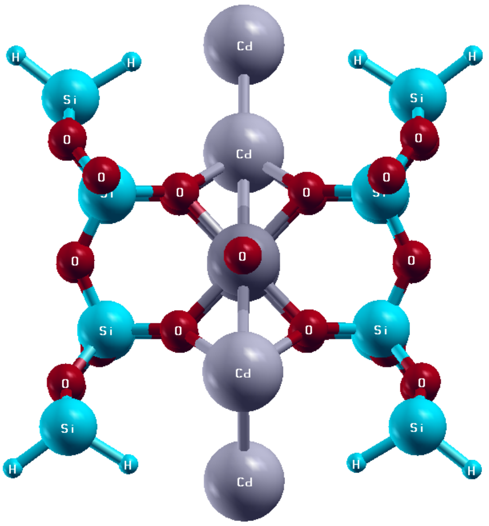

Figure 3.57: Cd-ETS-10 Model I Front

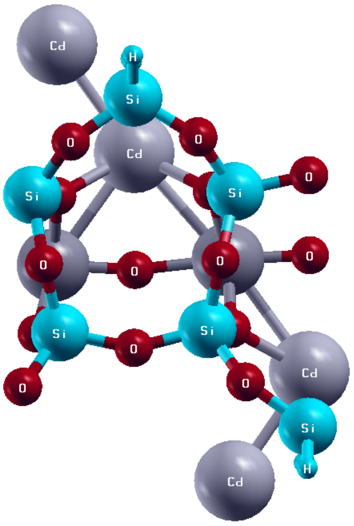

Figure 3.58: Cd-ETS-10 Model I Side

3.1.2.9 Cu-ETS-10 Computations

Copper has 1.90 Pauling scale electronegativity and 1.60 Å atomic radius. While these physical properties are similar to silver case, its ionic radius and valence electron number differ from silver. In the Fig. 3.59 and Fig. 3.60 it can be seen that distortions caused by addition of copper cations observed. Linearity of the quantum wire and periodicity of the continuous chain geometry seem to be broken in Table 3.17.

Table3.17: Selected structural parameters of the optimized structures of the Model I of Copper ETS-10. Represented bond distance units are Å.

	Model I
Ti1-Ti2	3.79
Ti2-O2	2.03
Ti2-O3	1.82
Cu-O2	2.12
Ti1-O2	1.83
Ti1-O1	2.03
Ti3-O3	2.03
Ti3-O4	1.83
Ti2-O5	2.05
Ti1-O6	2.45
Ti3-O7	2.45
Ti2-O6	4.44
Ti1-Cu	2.90
Ti1-O2-Ti2	159°
O2-Ti2-O3	163°
O2-Ti2-O5	88°

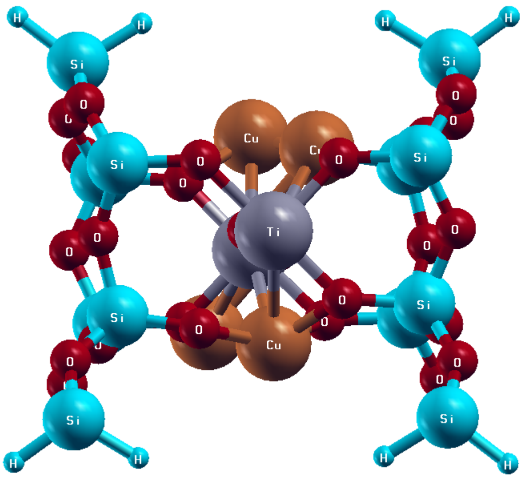

Figure 3.59: Cu-ETS-10 Model I Front

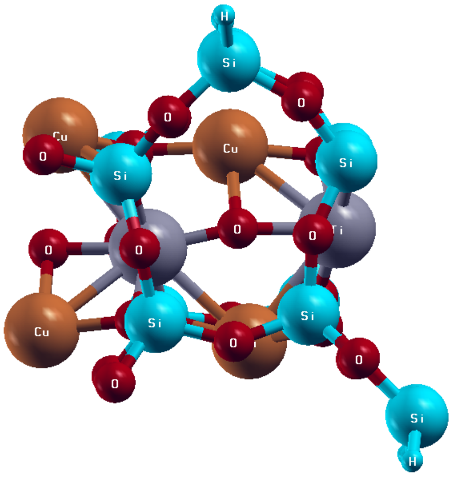

Figure 3.60: Cu-ETS-10 Model I Side

3.1.2.10 Pb-ETS-10 Computations

Lead exchanged ETS-10 model is computed with model I. Lead has 1.65 Pauling scale electronegativity, same as zinc, it has 1.80 Å atomic radius and two outermost electron numbers. Chemical properties show some similarities with the zinc case. In the Fig. 3.61 and Fig. 3.62 it can be seen that converged optimized coordinates show some similarities with zinc and cadmium models. Instead of four cations, system charge distribution is balanced with two cations. Selected geometries presented in Table 3.18, results suggest that characteristic parameters of ETS-10 model are preserved. Interesting result is one long and one short Ti-O bond leaves its place to symmetric bond type at 1.93 Å, which is similar to calcium exchanged ETS-10 model I. Calculated band gap energy is 0.2228 eV for model I, this result is also similar with Ca-ETS-10 model I, Zn-ETS-10 model I and Cd-ETS-10 model I.

Table3.18: Selected structural parameters of the optimized structures of the Model I of Lead ETS-10. Represented bond distance units are Å.

	Model I
Ti1-Ti2	3.75
Ti2-O2	1.94
Ti2-O3	1.94
Pb-O2	2.27,6.02
Ti1-O2	1.93
Ti1-O1	1.93
Ti3-O3	1.93
Ti3-O4	1.93
Ti2-O5	2.32
Ti1-O6	2.33
Ti3-O7	2.33
Ti2-O6	4.44
Ti1-Pb	3.32,6.95
Ti1-O2-Ti2	152°
O2-Ti2-O3	151°
O2-Ti2-O5	79°

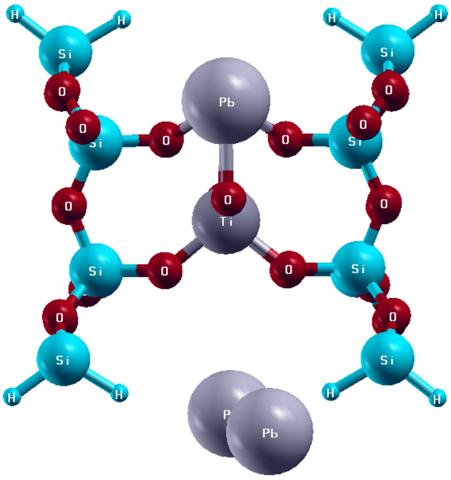

Figure 3.61: Pb-ETS-10 Model I Front

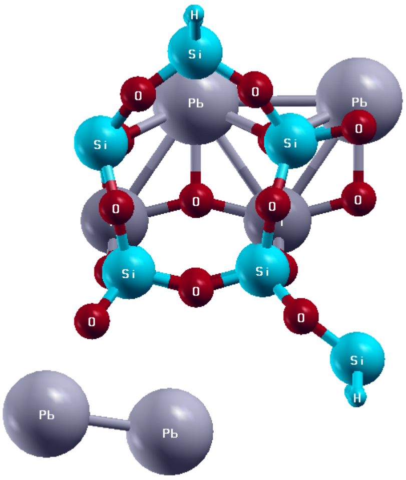

Figure 3.62: Pb-ETS-10 Model I Side

3.1.3 Dye, Nanoparticle Simulations

Sensitizers and modification agents are also modelled. In order to achieve a successful sensitizer-semiconductor combination in the DSSC scheme experimentally, simulation of semiconductor dye couple became essential. First step is converging optimized results of the molecules separately. Optimization studies of ETS-10 are presented in the previous section. In this section ruthenium based dye molecule and nanoparticle results will be presented.

Dye Simulations

Modelled dye molecule is known as N886, trans-[Ru(L)(NCS)2], L = 4,4' "-di-tert-butyl-4',4' '-bis(carboxylic acid)-2,2':6',2' ':6' ',2' "-quaterpyridine, which is a Ruthenium based organometallic dye molecule first introduced by Graetzel [86]. In the Fig. 3.63 and Fig. 3.64, optimized coordinates of the N886 dye model can be seen. Succesful convergence achieved with model.

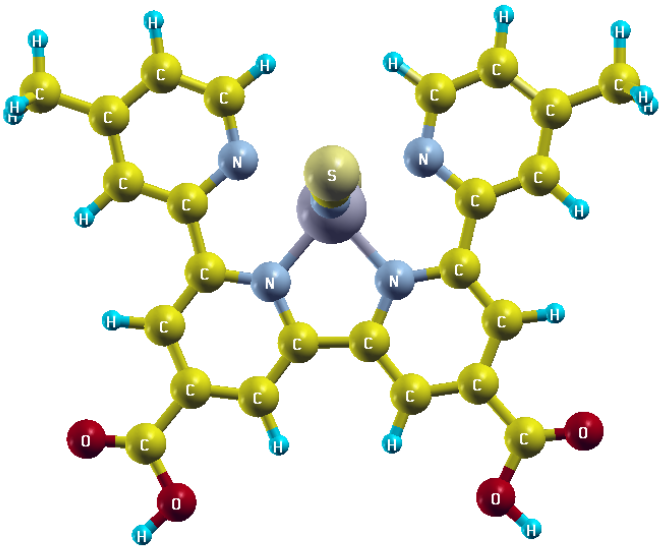

Figure 3.63: N886 front

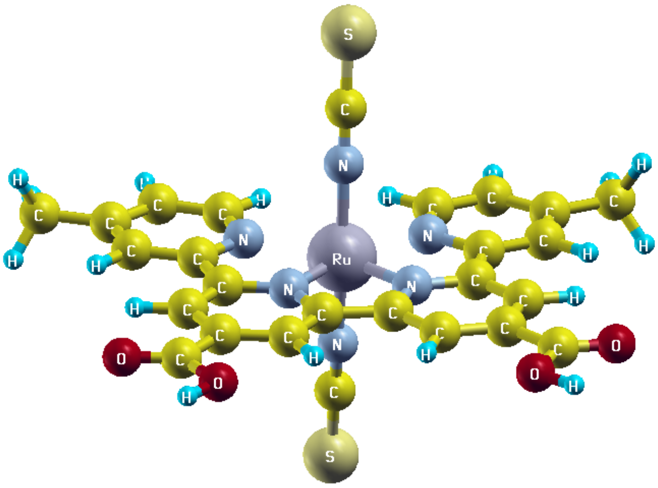

Figure 3.64: N886 side

Nanoparticle

Quantum Dots are very popular sensitizer materials used in DSSC structures. Silver nanoparticles are modelled and simulated in a very broad range of atomic size including 13 atoms sized nanoparticle to 300 atoms sized nanoparticles. Some selected results are presented in Fig. 3.65-3.68. Converged bond distances of nanoparticles have been computed as 2.93 Å, 3.00 Å, 3.10 Å and 3.15 Å respectively. Sizes of nanoparticles are 5.57 Å for 13-Atom, 7.95 Å for 20-Atom, 14.40 Å for 100-Atom and 22.58 Å for 300-Atom models. It can be speculated as up to 100 atoms, nanoparticles could fit into the largest pore of ETS-10. An example of silver nanoparticle inside ETS-10 could be seen in the Fig. 3.69.

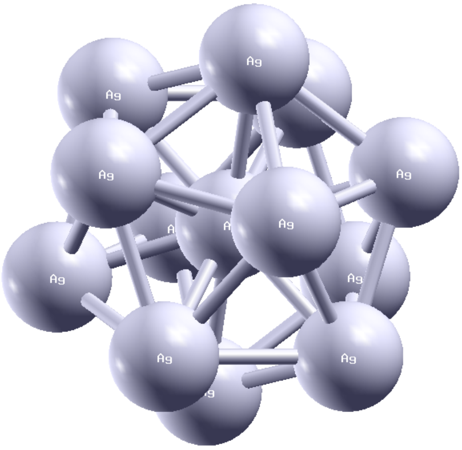

Figure 3.65: 23-Atom Ag Nanoparticle

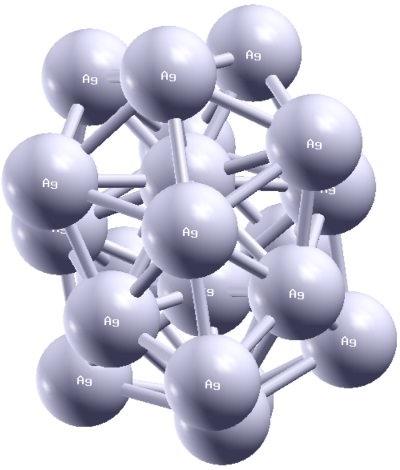

Figure 3.66: 20-Atom Ag Nanoparticle

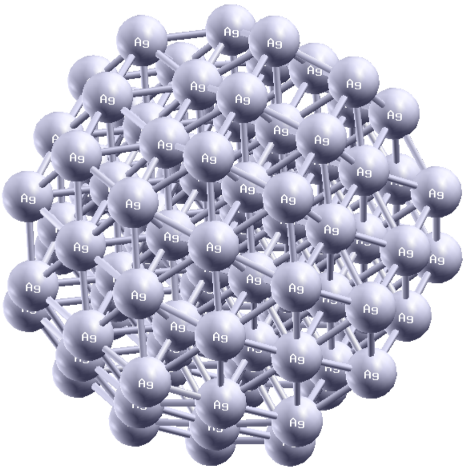

Figure 3.67: 100-Atom Ag Nanoparticle

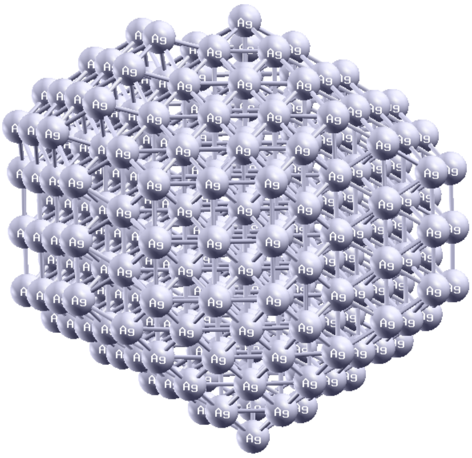

Figure 3.68: 300-Atom Ag Nanoparticle

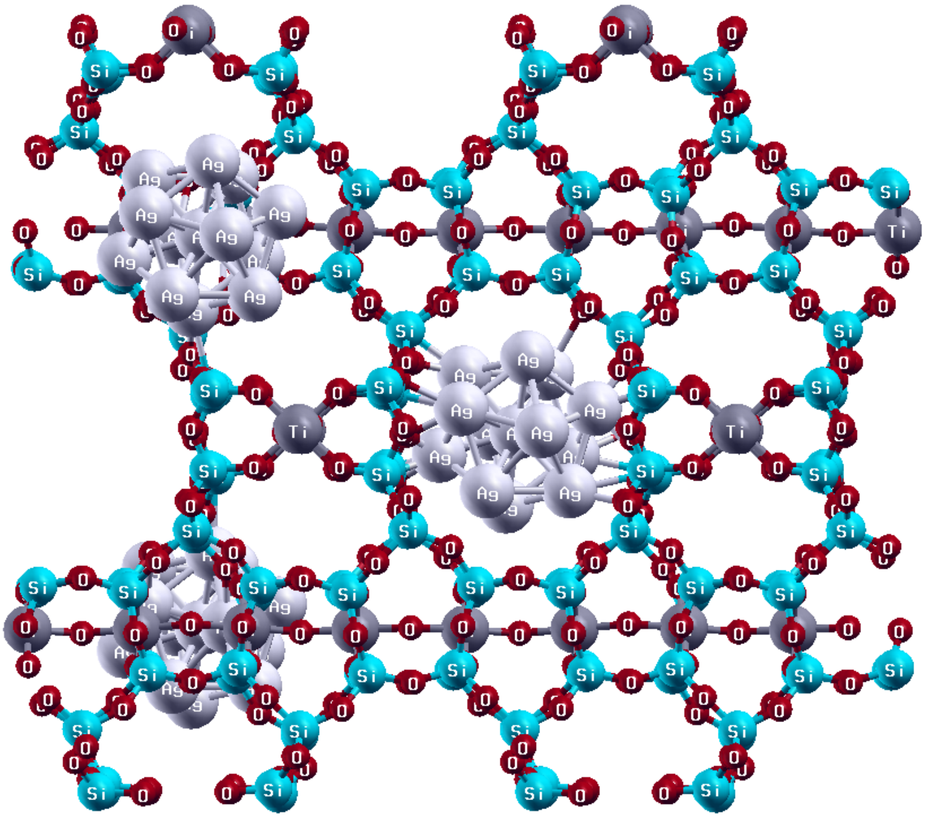

Figure 3.69: 13-Atom Silver Nanoparticle Embedded inside ETS-10

3.2 Experimental Results

Typical truncated bipyramid morphology of ETS-10 [87] was observed in the SEM image of the ETS-10, Fig. 3.70. The XRD spectrum of ETS-10 in Fig. 3.71 is an example taken from literature [88]. The XRD patterns in the Fig. 3.72 showed that there were no structural collapse, crystal deformation in the structure of ETS-10, these results can also be compared with literature results. SEM images and XRD results showed that synthesized crystals were pure ETS-10.

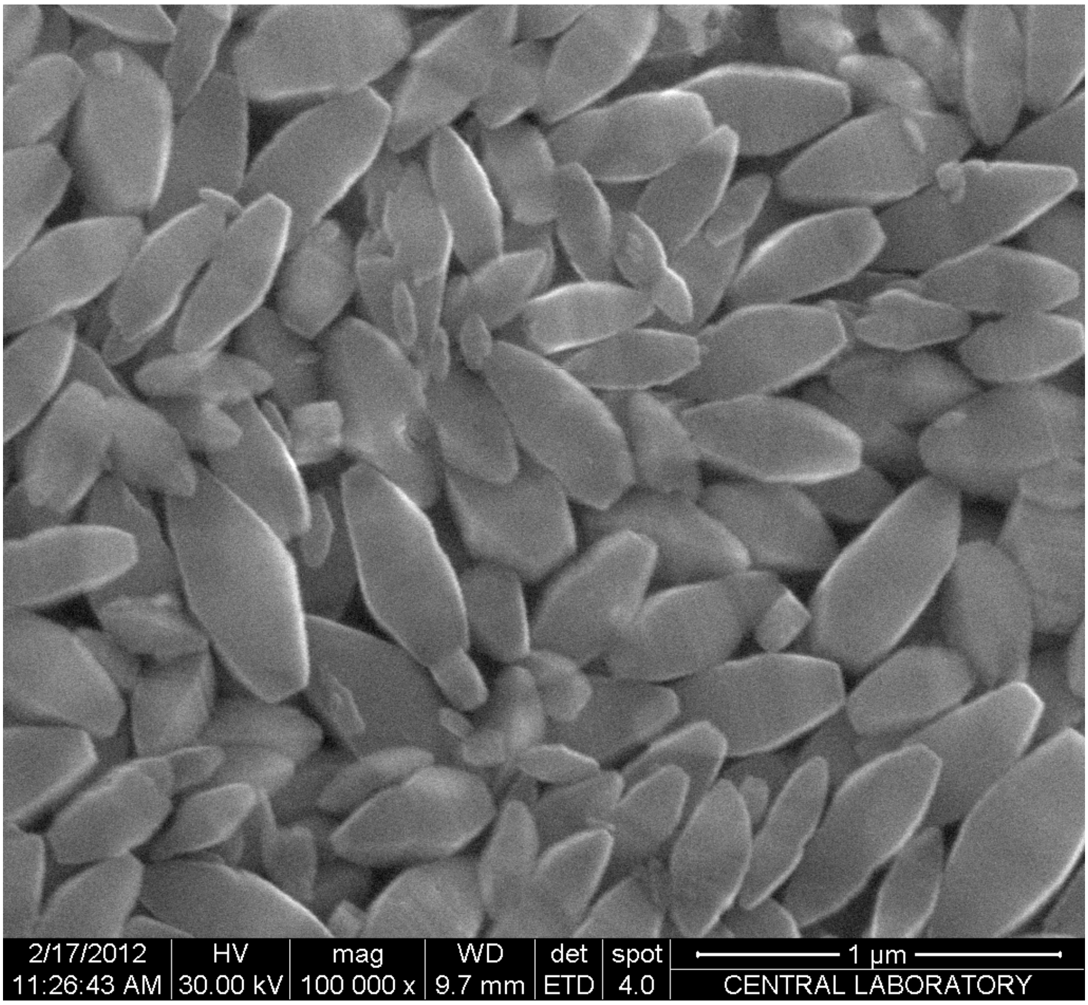

Figure 3.70: SEM Micrograph of ETS-10

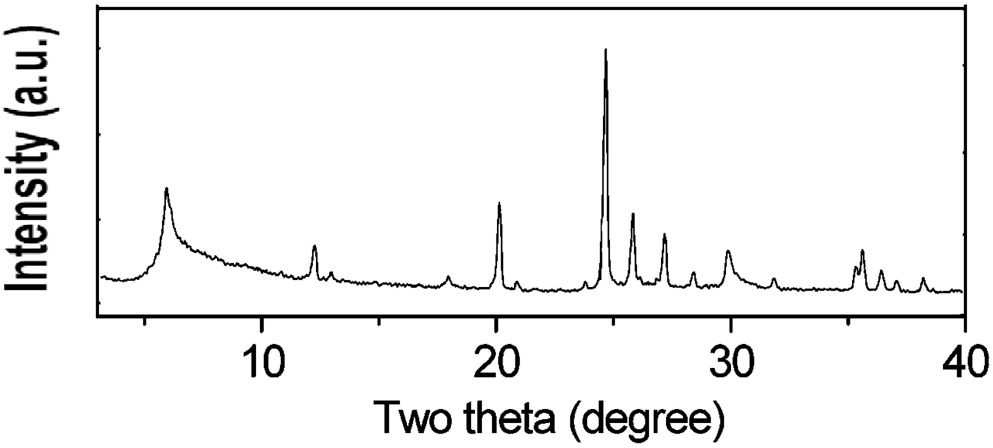

Figure 3.71: XRD Spectrum of ETS-10 [89]

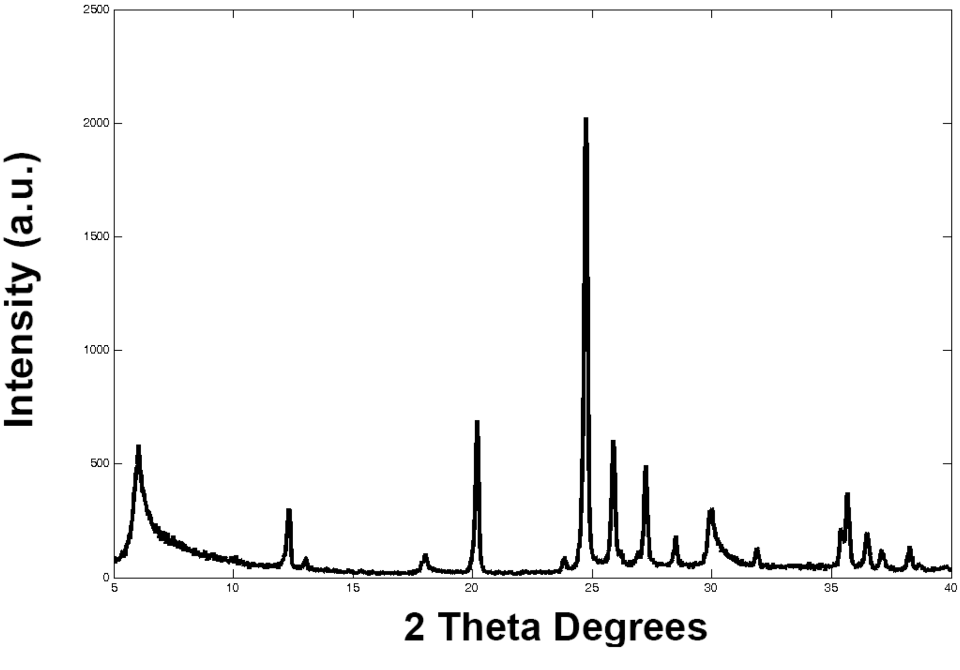

Figure 3.72: XRD Spectrum of ETS-10 This Work

Raman Results

Characteristic Raman spectroscopy of ETS-10 and fingerprint peak of ETS-10 at 724cm^{-1} can be seen at Fig. 3.73.

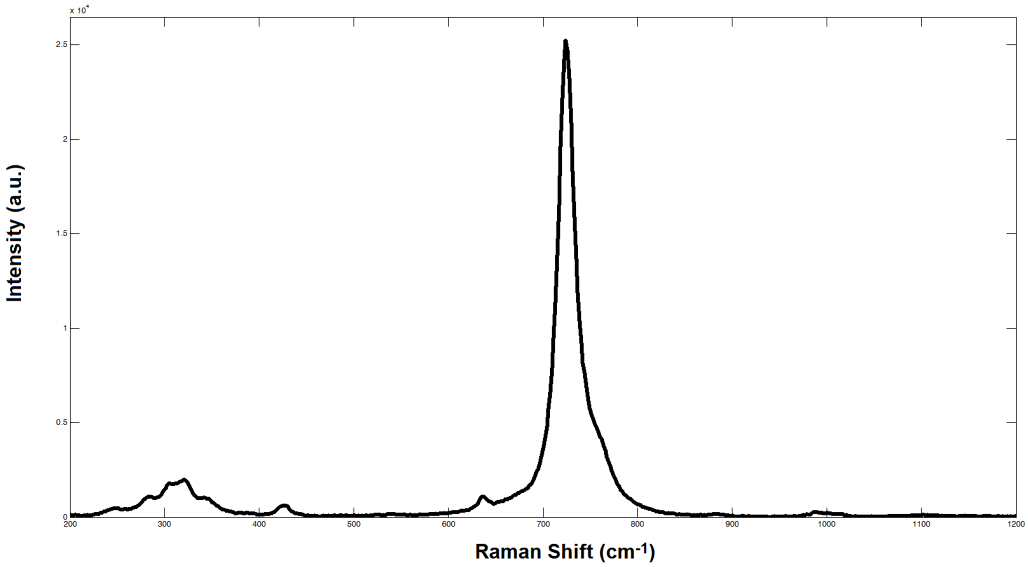

Figure 3.73: Raman Spectrum of ETS-10

Maximum peak intensity is observed at 707 cm^{-1} for silver exchanged ETS-10, which is presented in the Fig. 3.74. More ion exchange does not seem to distort the -O-Ti-O-Ti- chain of Ag-ETS-10, maximum intensity of the Raman spectrum unchanged at 707 cm^{-1} which can be seen at Fig. B.10. Modelling results, Table 3.10, Table 3.7 and Fig. 3.9, were suggesting that silver exchange wouldn't cause any distortion in the crystalline structure of ETS-10. Sharp peak at 707.327 cm^{-1} confirms it experimentally. Silver ion exchange does not affect structure of the ETS-10 as distortion and in the Fig. B.10 it could be added that even continue of ion exchange procedure for one day wouldn't affect ETS-10.

Maximum peak intensity is observed at 716 cm^{-1} for Calcium exchanged ETS-10, which can be seen at Fig. 3.75. Peak at 716.432 cm^{-1} suggest that structure of the ETS-10 was preserved. However there exists an broadening in the peak, which could be concluded as some structural variations in the system. More ion exchange seems to affect and deform the -O-Ti-O-Ti-O- chain of Ca-ETS-10, maximum intensity of the Raman spectrum unchanged at 783.505 cm^{-1}. Long durations of ion-exchange procedure could have caused agglomeration of calcium atoms in the system and eventually distort the quantum wire of ETS-10. Alien peaks in the Fig. B.12 could be explained by these distortions. Modelling studies showed that calcium atoms converge the similar cation sites with sodium and potassium atoms Table 3.9, Fig. 3.8 and Table 3.7, however asymmetric bond character of the quantum wire of one long and one short Ti-O bonds seemed to be vanished. Effect of the calcium atoms on the quantum wire was seen larger than sodium and potassium cases. Structural distortions seen at Fig. B.12

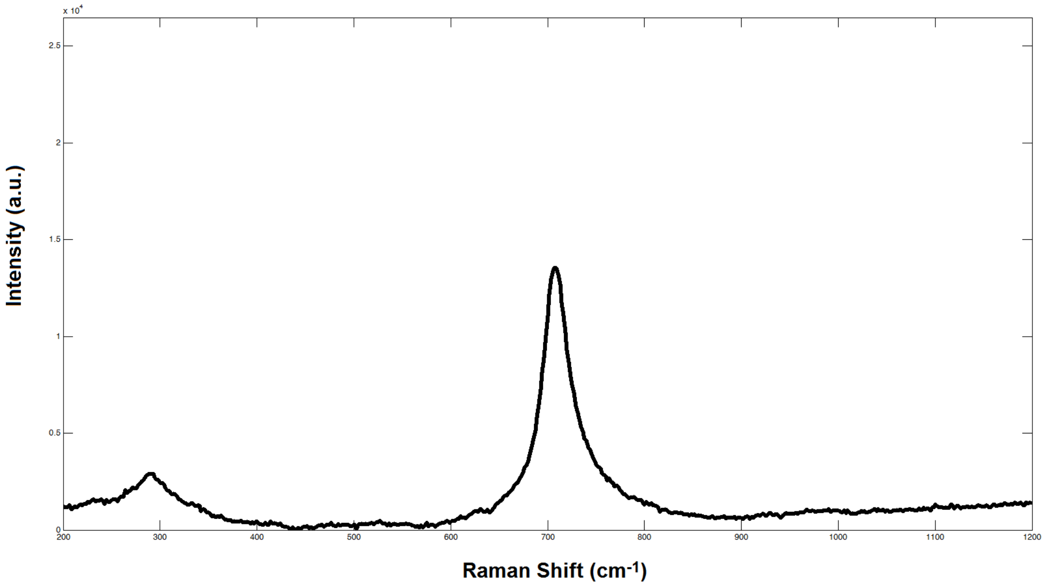

Figure 3.74: Raman Spectrum of Ag-ETS-10

could be explained by this relatively larger effect of calcium atoms.

Maximum peak intensity is observed at 536 cm^{-1} in the Fig. 3.76 for Zinc exchanged ETS-10. More ion exchange seems to distort the -O-Ti-O-Ti-O- chain of Zn-ETS-10, maximum intensity of the Raman spectrum unchanged at 981 cm^{-1} which can be seen in Fig. B.14. Raman spectrum of zinc exchanged in Fig. 3.76 and Fig. B.14 ETS-10 suggest that significant structural distortions exist in ETS-10. Sharp peak at 724cm^{-1} in Fig. 3.73 is caused by the quantum wire. Fingerprint sharp peak loss in the Raman spectrum presents distorted quantum wire, which can be confirmed by the modelling results in Fig. 3.11, Table 3.11 and Table 3.7. Half of the zinc atoms were pushed away from the system as an optimized result and quantum wire geometry affected by the remaining zinc atoms in the system which can be easily seen in the Ti-O-Ti angles varience of 20° in Table 3.11. Further, long duration of ion exchange could have caused the agglomeration of zinc atoms and distort the frame and quantum wire similar to calcium exchanged case.

Maximum peak intensity is observed at 617 cm^{-1} for ruthenium exchanged ETS-10. Fingerprint Raman spectrum of ETS-10 was seemed to be lost, serious structural distortions exist in quantum wire respect to Fig. 3.77. This result is in consistent with computations. Significant structural distortions and loss of characteristic Ti-Ti distance in the ETS-10 geometry was calculated in Table 3.13.

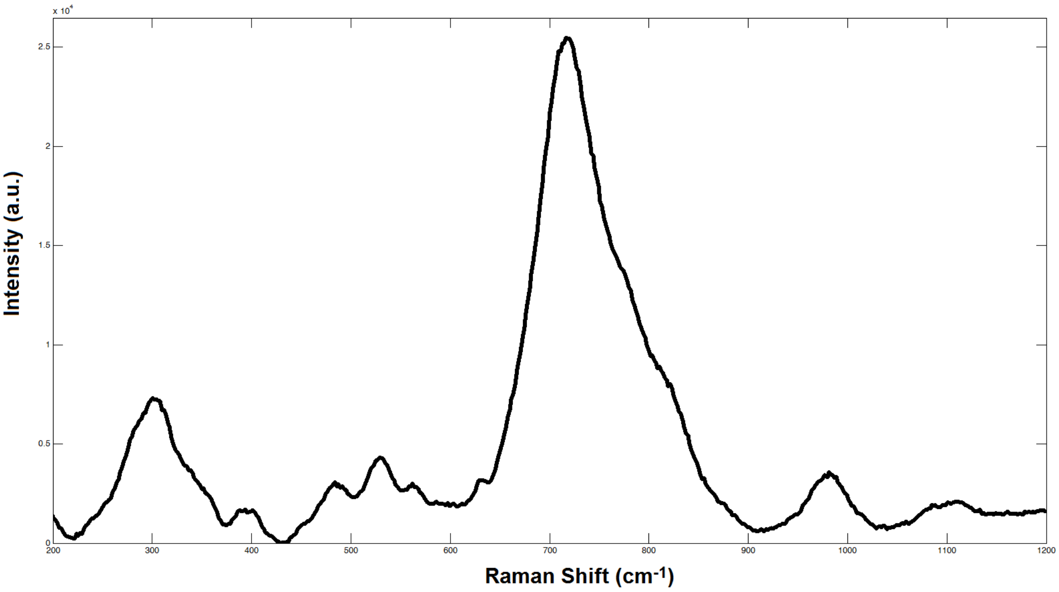

Figure 3.75: Raman Spectrum of Ca-ETS-10

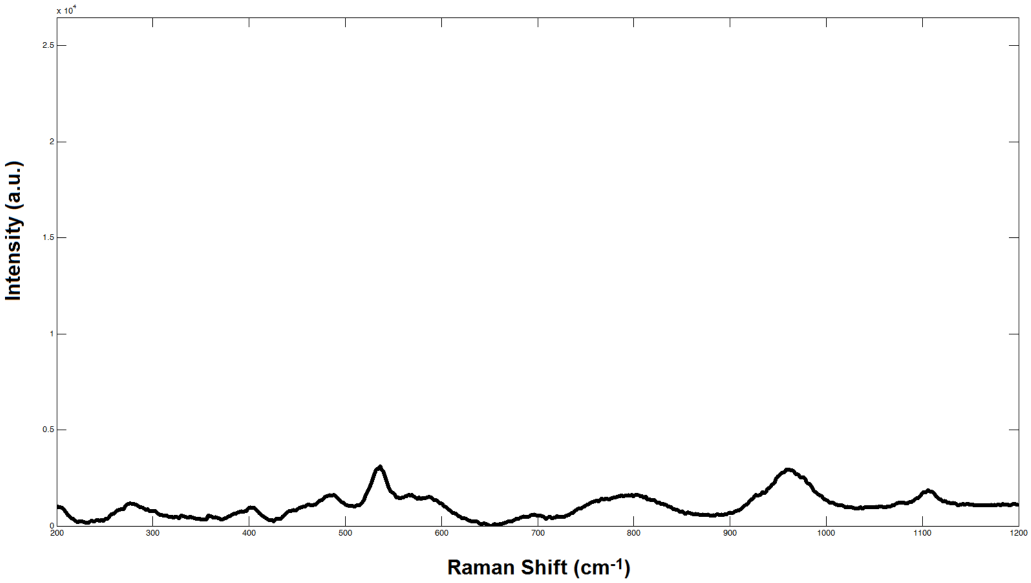

Figure 3.76: Raman Spectrum of Zn-ETS-10

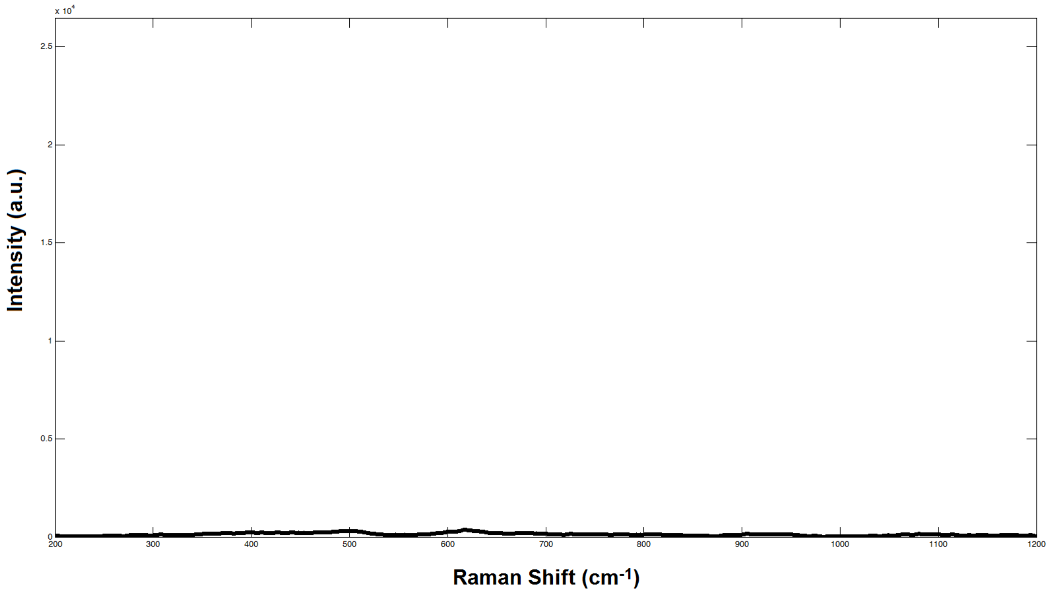

Figure 3.77: Raman Spectrum of Ru-ETS-10

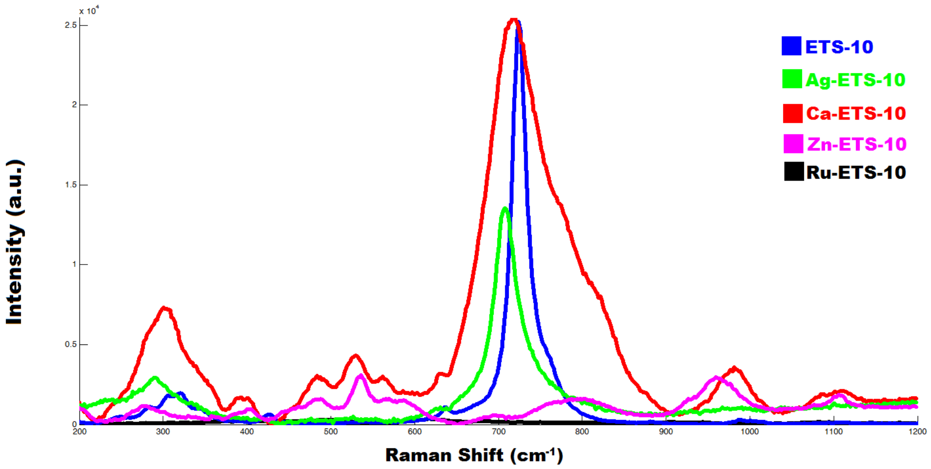

Figure 3.78: Raman Spectrum of As-Synthesized ETS-10 and Ca, Ag, Zn and Ru Exchanged ETS-10.

3.3 Solar Cell Results

ETS-10 with its as-synthesized quantum wire formation and charge balancing cations oriented around quantum wire has a significant potential for electronic applications especially in photovoltaic studies. High cation exchange capacity makes ETS-10 very attractive due to reliably and controllably modifiable electronic properties of material with cation exchange and doping. In this study silver ion and silver nanoparticle exchanged ETS-10 structure are investigated as a potential for photovoltaic applications, modified ETS-10 and non-modified ETS-10 were used as semiconductor in replacement of titanium dioxide network in Graetzel Cells. Although there are some works on different ion-exchange studies in ETS-10 investigating the electronic changes induced into ETS-10, there is still limited information about the ETS-10 in photovoltaic applications and we have not found any study that is investigating photovoltaic applications of the modified ETS-10 to the best our knowledge. Accordingly, in this current study we have used as-synthesized ETS-10, silver ion and silver nanoparticle modified ETS-10 as semiconductor network and investigated solar cell characteristics of modified and non-modified ETS-10. Dye Sensitized Solar Cells are constructed from three types of modified zeolites and for comparison pure Titanium Dioxide. Pure ETS-10, Ag ion exchanged ETS-10 and Ag cluster formed ETS-10 were synthesized by hydrothermal sol-gel routes. The produced particles were suspended in a paste composed of ethyl cellulose and alpha terpineol. Thick films of different modified zeolites were coated on FTO coated glasses by screen printing and subsequent thermal treatment at 500°C. The sensitizer was chosen as N719 organometallic dye and iodide/tri-iodide redox couple containing liquid electrolyte. Cell characteristics were determined under AM 1.5G conditions.

Table3.19: Summary of ETS-10, Ag-ETS-10 and Ag(0)-ETS-10 semiconductor based DSSC characteristics

		V_{OC}	J_{SC}	FF	Efficiency
ETS-10	forward	0.418	0.047	36.7	0.0082
	reverse	0.449	0.046	34.6	0.0080
Ag(0)-ETS-10	forward	0.425	0.044	36.4	0.0076
	reverse	0.435	0.041	33.9	0.0069
Ag-ETS-10	forward	0.424	0.026	40.3	0.0050
	reverse	0.552	0.025	30.5	0.0048

It was observed that modification of ETS-10 with silver nanoparticles doesn't have a significant influence on the cell characteristics, while addition of silver as Ag+ ion enhances photovoltage up to 120mV where current density is reduced noticeably, which can be seen in the Table 3.19, Fig. 3.81, Fig. 3.82 and Fig. 3.83. This situation is explained as positive shift in the Fermi level of ETS-10 due to Ag+ introduction into the structure which is determined by the DFT calculations of the band structure of ETS-10. DOS analysis are presented in the Fig.3.79 and Fig. 3.80.

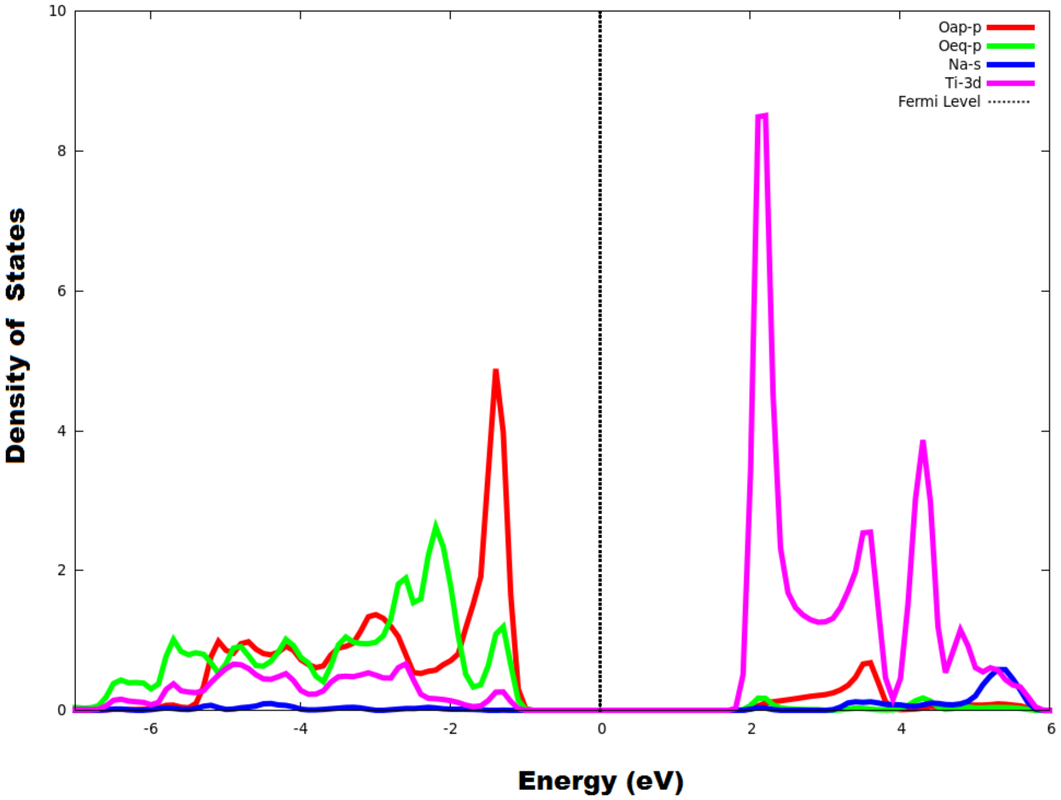

Figure 3.79: DOS Analysis of Na-ETS-10

It was seen that valence of the modifying agent on ETS-10 significantly influences the electronic structure of the ETS-10 type zeolites and the performance of the zeolite based DSSC.

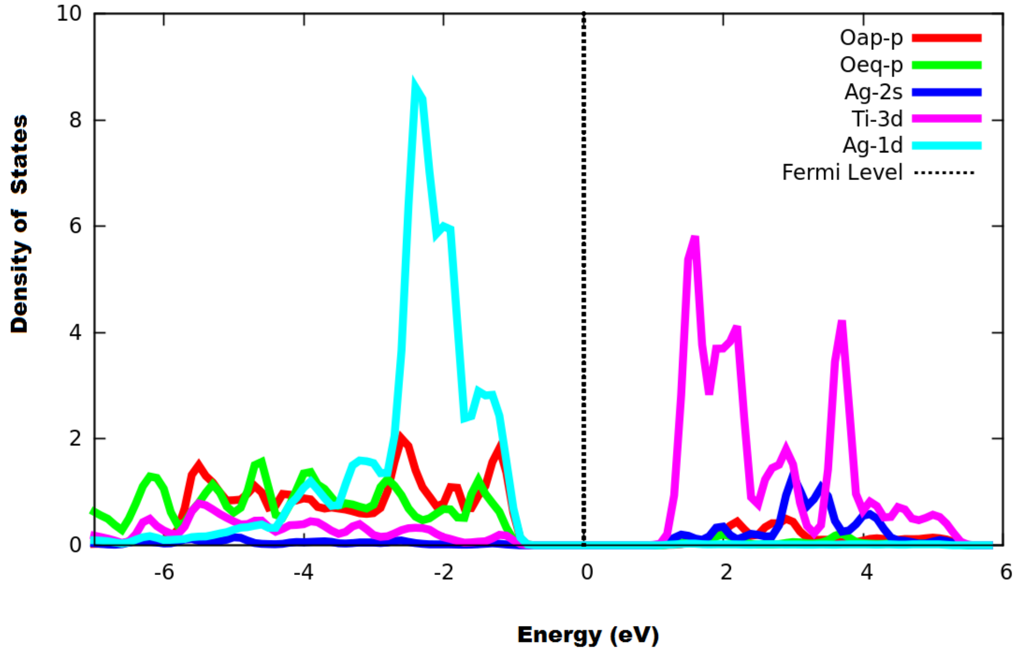

Figure 3.80: DOS Analysis of Ag-ETS-10

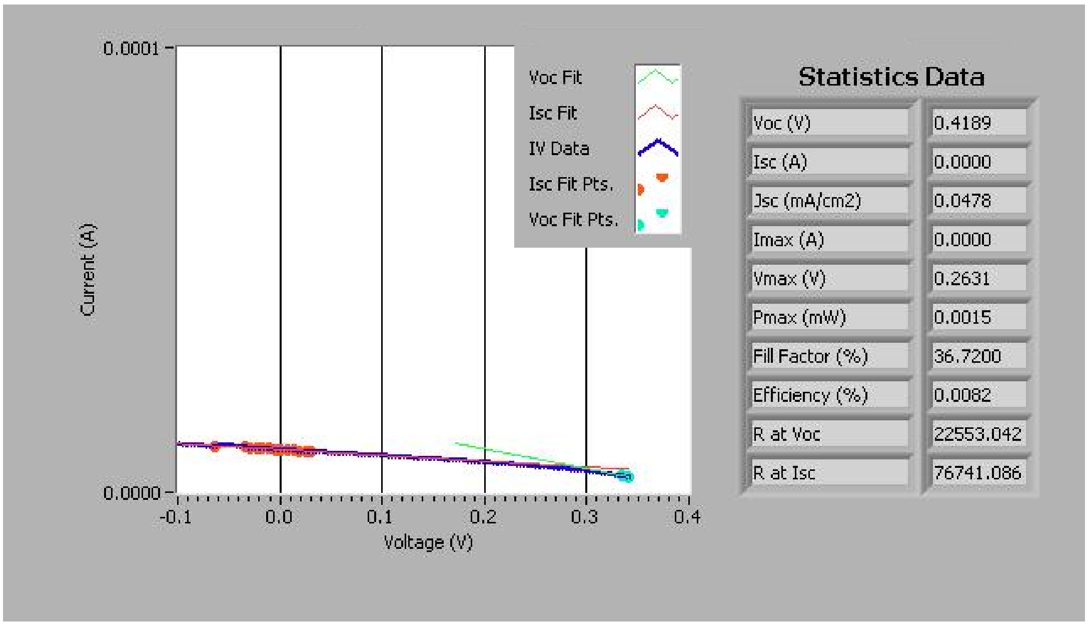

Statistics Data

Voc (V)	0.4189
Isc (A)	0.0000
Jsc (mA/cm2)	0.0478
Imax (A)	0.0000
Vmax (V)	0.2631
Pmax (mW)	0.0015
Fill Factor (%)	36.7200
Efficiency (%)	0.0082
R at Voc	22553.042
R at Isc	76741.086

Figure 3.81: ETS-10 DSSC Cell Test

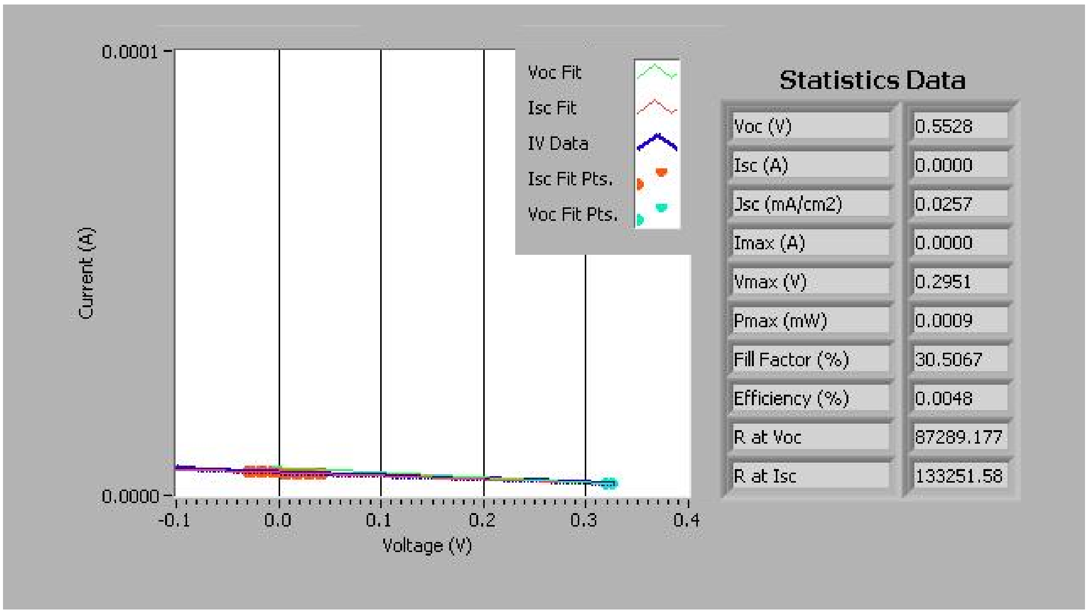

Statistics Data

Voc (V)	0.5528
Isc (A)	0.0000
Jsc (mA/cm2)	0.0257
Imax (A)	0.0000
Vmax (V)	0.2951
Pmax (mW)	0.0009
Fill Factor (%)	30.5067
Efficiency (%)	0.0048
R at Voc	87289.177
R at Isc	133251.58

Figure 3.82: Ag^{+}-ETS-10 DSSC Cell Test

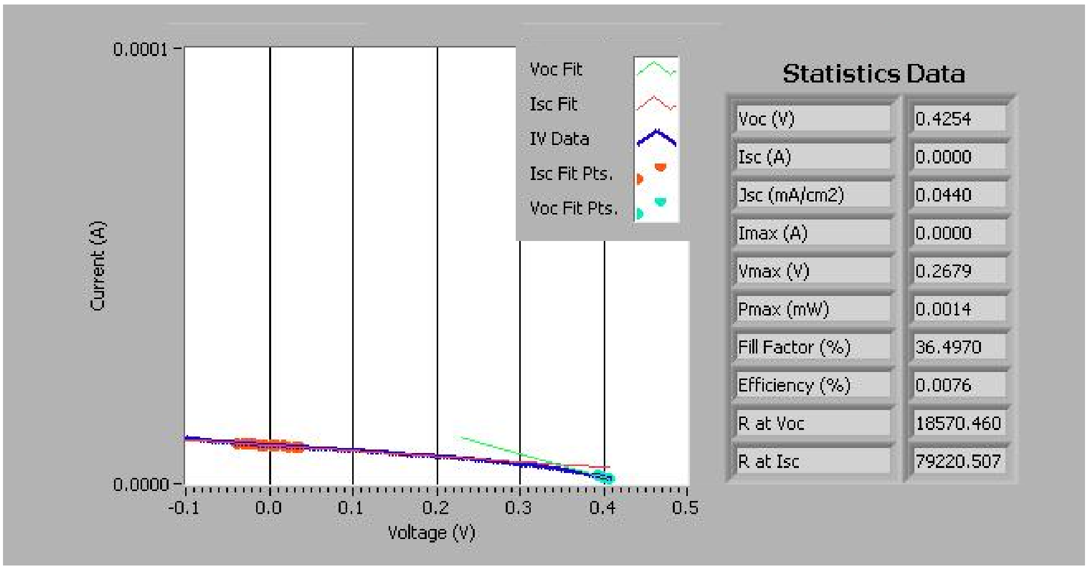

Statistics Data

Voc (V)	0.4254
Isc (A)	0.0000
Jsc (mA/cm2)	0.0440
Imax (A)	0.0000
Vmax (V)	0.2679
Pmax (mW)	0.0014
Fill Factor (%)	36.4970
Efficiency (%)	0.0076
R at Voc	18570.460
R at Isc	79220.507

Figure 3.83: Silver Nanoparticle-ETS-10 DSSC Cell Test

CHAPTER 4

CONCLUSION

Successful ETS-10 model was achieved with three different models. Several unsuccessful attempts reveal that quantum wire is highly sensitive to any symmetry change in the structure. Three different combination of frame atoms existence presented effect of existence frame atoms on the structure and cations. After stable Na-ETS-10 models were achieved different starting symmetries were tried in order to confirm that quantum wire has asymmetric, one long and one short Ti-O bond character. Our data are reveal the presence of two inequivalent Ti–O bonds along the chain in the ETS-10 sodium form, in disagreement with more recent theoretical and experimental studies and in good agreement with earlier experimental literature results. Density functional theory (DFT) calculations within the gradient-corrected approximation (GGA) have been carried out on three models of ETS-10 with the aim to elucidate the effect of ion exchange on the structural, electronic and vibrational properties of the Ti–O–Ti quantum wire. Atomic size, electronegativity and valence electron numbers of cations carry significance in the simulations, which were discussed. Results of models and different cations attempts point that potassium, calcium, silver exchange ETS-10 converge similar positions. Simulation results of these models were confirmed by the experimental results. When sodium atoms are exchanged with calcium, potassium and silver, no structural distortions were observed both theoretically and experimentally. However in calcium case, asymmetric character of quantum wire was lost respect to modelling results. Raman spectrum of calcium exchanged ETS-10 structure pointed that expansion in the fingerprint sharp peak of ETS-10 in 700-750 cm^{-1}, which can be indication of observed bond character change in modelling results. Zinc exchanged ETS-10 simulations showed that respect to Na, Ca, K and Ag cases, half of the Zn atoms were needed to balance the excess charge of quantum wire. In order to clarify this result Cd and Pb atoms were employed. Similar result was expected in Pb and Cd exchanged ETS-10 case respect to electronegativity, atomic size and valence electron similarities of Zn, Cd and Pb. Simulations results showed that half number of atoms needed in the Pb and Cd exchange case also. Same structural parameters were observed. Simulation results pointed that for Zn-ETS-10 model very similar geometric parameters observed with Na-ETS-10 and K-ETS-10. Difference observed in the Ti-O-Ti angles. Raman spectrum of zinc exchanged ETS-10 structure presented a disordered structure. Variance in the quantum wire simulations of Zn-ETS-10 could be an indicator for observed structural disorder. It should be noted that atomic reactions happen in very small time scales, experimental setup of long duration respect to atomic time scales for ion-exchange procedure might have caused enlarge the disorder. Cations with very high electronegativity possessed higher structural disorder. This can be explained by the unbalanced quantum wire charge distribution respect to cations tendency of preserving neutral charge character. Most of the physical optical and electronic properties of ETS-10 are defined by quantum wire. Unbalanced charge distribution of Ti atoms force structure to distort. Au-ETS-10 models show that serious structural disorders exist. Gold atoms force quantum wire to deform. Periodicity and unit cell symmetry was lost in Au-ETS-10 case. Effect of disorder is maximum in the Au-ETS-10 model III. This can be explained confining forces of frame atoms on gold. Ru-ETS-10 models show similar disorders. Addition to gold exchange model, ruthenium models converge to disordered frame structure. In order to clarify results of ruthenium, boron exchanged ETS-10 simulations completed. Similar disorders were observed with B-ETS-10 model, which were expected respect to physical property similarities of both atoms. Interesting case for the Ru-ETS-10 model is model III. Ru-ETS-10 converge to a symmetric, periodic geometry different from original ETS-10 geometry, while differ from disordered model I and model II structure. This can be explained as large radius of interest of ruthenium atom is affected by frame atoms. Existence of frame atoms and large cut off distance of effect of ruthenium perturb the equilibrium of unit cell symmetry. Raman spectrum of Ru exchanged ETS-10 confirms significant structural disorder in good agreement with simulations. The nature and spectral position of the ligand-to-metal charge transfer transition experimentally observed at 4.02 eV is also well accounted for by our DFT calculations. Calculated band gap of Na-ETS-10 is 3.26 eV for model I and 3.34 eV for model II. These results are much better than previous theoretical studies in the literature. Analysis of electronic properties of Na-ETS-10 showed that conduction band of ETS-10 is mainly contributed by d-orbitals of Ti atoms and valence band is mainly contributed by p-orbitals of O_{eq} and O_{ap} atoms which is in good agreement with literature results. when concentration of ions are 1/8, it is showed that system tolerates the alien ion. No significant structural disorders were computed for 1/8 concentration. Electronic property computations showed that ion exchange procedure significantly affects the band gap structure. This result conflict with literature. The largest band gap is observed in the Na and K exchanged ETS-10 cases and ion exchange procedure shrink the band gap for all other ions. Silver ion exchange ETS-10 structure showed 1 eV shrink in band gap, which is in good agreement with literature. Ca-ETS-10 models show presented a metallic electronic structure. Fermi level was shifted to conduction band of Ca-ETS-10, which is a surprising result and conflicts with previous studies. Au-ETS-10, Zn-ETS-10 and Ru-ETS-10 models show very narrow band gap structure. This can be explained by uncharged, metallic atoms in system that does not interact with ETS-10 and structural distortions also could have cause these system to change electronic structure. Vibrational properties, phonon frequencies of ETS-10 and ion exchanged ETS-10 were also studied. Results showed similarities with experimental analysis, however some post process is needed to eliminate arbitrary results come from methodology and simulated ones. Partial and full exchange of Na^+ cations with alkaline, earth-alkaline and transition metal ions affect both structural, electronic and vibrational properties of the quantum wire. The theoretical results have been rationalized and compared with recent experimental data.

ETS-10, Ag-ETS-10 and Ag nanoparticle embedded ETS-10 were employed in solar cell studies. Successful semiconductor curves were observed with solar simulator. It was seen from the I-V measurements that addition of silver particles into the ETS-10 structure, does not affect the cell parameters significantly. However when silver is introduced into the structure as Ion form, open circuit potential of the cell increases about 120mV, where short circuit current flux decreases about $\approx$ % 40. This situation can be explained as an increase in the Fermi level of the semiconductor upon addition of silver ions into the structure. This ion addition seems to be shifting conduction band potential of ETS-10 to a higher energy level, which results in an enhanced open-circuit potential where this potential is defined as the electrochemical potential difference between the Fermi level of the semiconductor and the redox potential of the tri-iodide/iodide couple. This shift however results in a suppressed electron injection from LUMO level of the dye molecule and the conduction band of the semiconductor. This effect is only observed in the ionic silver added semiconductor, where metallic silver does not affect electronic structure of semiconductor significantly. Although simulations conducted on silver ions exchanged ETS-10 structures suggest an narrowing in the band gap of the material, it was observed that after heat treatment of the anode chemical state of the silver changes from ionic state to most like metallic or oxide form which has to be confirmed by the detailed XPS and XRD analysis in order to confirm the above theory. Theoretical studies show that Fermi Level of the Ag-ETS-10 is 0.5eV lower than Na-ETS-10. This can be speculated as narrowing in the gap between electrolyte and fermi level of the semiconductor cause lower Open-Circuit voltages. However decrease in the short circuit flux should be clarified.

Further, modelling results showed that ion exchange procedure affects electronic structure of ETS-10. In order to clarify that information, different ions can be exchanged with ETS-10 experimentally. If the observed data is consistent with modelling results, then electronic properties of new ion exchanged ETS-10 structure is analysed and tune for the most optimized results for photovoltaic applications. However, ETS-10 showed very low efficiency values for DSSC applications. Even though band gap tuning could be possible with ion exchange respect to simulation results, there are still some major problems for solar cell applications, including current flux. Solar cell studies pointed lack of efficient charge cycles in cell structure. A detailed investigation should be completed in order to find interactions of Pt coated electrode, electrolyte and dye. Work functions, band gap structures including valence band and conduction band positions and Fermi level should be investigated in order to design the most efficient combination. Another important problem with solar cell studies, ETS-10 adsorption on the FTO substrate is much weaker than TiO_2. Current flux is directly related with available charge carriers in the system and weaker adsorption of ETS-10 indicates less available charges respect to less dye adsorbed on the surface of ETS-10. This problem could be altered by growing ETS-10 crystals directly on the surface of FTO coated glasses, by this way adsorption problems will be overcome and more importantly desired thickness can be controllably achieved. Another important study could be done with dye molecules. ETS-10 as a zeolite has very large surface area, which is essential in the DSSC design in order to combine dye and semiconductor in such a way that incident photons can travel through semiconductor without scattering or absorbed by the semiconductor directly to absorber molecule, while keeping as much absorber molecule as inside the pores of semiconductor. One step further to this study could be synthesizing the absorber molecule inside the channels of ETS-10. Absorber molecule doesn't need to be necessarily a dye molecule, instead of a dye molecule a quantum dot similar to silver nanoparticle studies in this work could be done. In this work nanoparticle studies, dye molecule studies and ion-exchange studies were completed in order to understand and compare the experimental and theoretical results. In parallel to presented results, nanoparticle and dye embedding in the pores of ETS-10 and electronic properties of these nanoparticles and dye molecules were also studied.

REFERENCES

[1] Hubbert Koller. Zeolites, 2009.

[2] Takehito Nakano Truong Cong Duan and Yasuo Nozue. Magnetic and optical properties of rb and cs clusters incorporated into zeolite a. *e-J. Surf. Sci. Nanotech.*, 5:6–11, 2007.

[3] T. Maeser. Introduction to zeolite science and practice. *Studies in Surface Science and Catalysis*, 168:1, 2007.

[4] Jens Weitkamp. Zeolites and catalysis. *Solid State Ionics*, 131:175–188, 2000.

[5] U Simon, U Flesch, W Maunz, R Müller, and C Plog. The effect of {NH3} on the ionic conductivity of dehydrated zeolites naxa0;beta and hxa0;beta. *Microporous and Mesoporous Materials*, 21(1–3):111 – 116, 1998.

[6] Sandhya Babel and Tonni Agustiono Kurniawan. Low-cost adsorbents for heavy metals uptake from contaminated water: a review. *Journal of Hazardous Materials*, 97(1–3):219 – 243, 2003.

[7] Chemistry and microbiology of permeable reactive barriers for in situ groundwater clean up. *Critical Reviews in Microbiology*, 26(4):221–264, 2000. PMID: 11192023.

[8] M. Arruebo, J. Coronas, M. Menéndez, and J. Santamarıa. Separation of hydrocarbons from natural gas using silicalite membranes. *Separation and Purification Technology*, 25(1–3):275 – 286, 2001.

[9] Michael tsapatsis. *Angewandte Chemie International Edition*, 51(36):8926–8926, 2012.

[10] Yoshio Morigami, Masakazu Kondo, Jun Abe, Hidetoshi Kita, and Kenichi Okamoto. The first large-scale pervaporation plant using tubular-type module with zeolite naa membrane. *Separation and Purification Technology*, 25(1–3):251 – 260, 2001.

[11] A. Dyer. Introduction to zeolite science and practice. *Studies in Surface Science and Catalysis*, 168:525, 2007.

[12] Faisal I Khan and Aloke Kr. Ghoshal. Removal of volatile organic compounds from polluted air. *Journal of Loss Prevention in the Process Industries*, 13(6):527 – 545, 2000.

[13] Ian E Maxwell and Peter W Lednor. Recent developments in materials science as applied to catalysis. *Current Opinion in Solid State and Materials Science*, 1(1):57 – 64, 1996.

[14] H. van Bekkum. Introduction to zeolite science and practice. *Studies in Surface Science and Catalysis*, 168:525, 2007.

[15] J.C. van der Waal and H. van Bekkum. Molecular sieves, multifunctional microporous materials in organic synthesis. *Journal of Porous Materials*, 5(3-4):289–303, 1998.

[16] S.M. Kuznicki. Preparation of small-pored crystalline titanium molecular sieve zeolites,, 1991.

[17] M. W. Anderson, O. Terasaki, T. Ohsuna, A. Philippou, S. P. MacKay, A. Ferreira, J. Rocha, and S. Lidin. Structure of the microporous titanosilicate ETS-10. *Nature*, 367:347–351, 1994.

[18] Nak Cheon Jeong, Myoung Hee Lee, and Kyung Byung Yoon. Length-dependent band-gap shift of TiO3(2-) molecular wires embedded in zeolite ETS-10. *Angewandte Chemie (International ed. in English)*, 46(31):5868–72, January 2007.

[19] Burcu Akata, Bilge Yilmaz, and Jr. Sacco, Albert. Titanosilicate ets-10 as a lewis acid catalyst in the meerwein–ponndorf–verley (mpv) reaction. *Journal of Porous Materials*, 15(3):351–357, 2008.

[20] Yuni K. Krisnandi, Eric E. Lachowski, and Russell F. Howe. Effects of ion exchange on the structure of ets-10. *Chemistry of Materials*, 18(4):928–933, 2006.

[21] Sitharaman Uma, Shalini Rodrigues, Igor N. Martyanov, and Kenneth J. Klabunde. Exploration of photocatalytic activities of titanosilicate ets-10 and transition metal incorporated ets-10. *Microporous and Mesoporous Materials*, 67(2–3):181 – 187, 2004.

[22] Inés Tiscornia, Silvia Irusta, Pedro Prádanos, Carlos Téllez, Joaquín Coronas, and Jesús Santamaría. Preparation and characterization of titanosilicate ag-ets-10 for propylene and propane adsorption. *The Journal of Physical Chemistry C*, 111(12):4702–4709, 2007.

[23] Vittorio Luca, Michael Osborne, Devlet Sizgek, Christopher Griffith, and Paula Z. Araujo. Photodegradation of methylene blue using crystalline titanosilicate quantum-confined semiconductor. *Chemistry of Materials*, 18(26):6132–6138, 2006.

[24] Lu Lv, Kean Wang, and X.S. Zhao. Effect of operating conditions on the removal of pb2+ by microporous titanosilicate ets-10 in a fixed-bed column. *Journal of Colloid and Interface Science*, 305(2):218 – 225, 2007.

[25] J.H. Choi, S.D. Kim, S.H. Noh, S.J. Oh, and W.J. Kim. Adsorption behaviors of nano-sized ets-10 and al-substituted-etas-10 in removing heavy metal ions, pb2+ and cd2+. *Microporous and Mesoporous Materials*, 87(3):163 – 169, 2006.

[26] Yaojun Wang, Xiaohui Liu, Rui Zhao, Yanqin Wang, Yanglong Guo, Yun Guo, Zhigang Zhang, Yunsong Wang, and Guanzhong Lu. Synthesis and characterization of functionalized mesoporous ethanesilica. *Microporous and Mesoporous Materials*, 102(1–3):325 – 332, 2007.

[27] Nak Cheon Jeong, Hyunjin Lim, Hyeonsik Cheong, and Kyung Byung Yoon. Distribution pattern of length, length uniformity, and density of tio32 quantum wires in an ets-10 crystal revealed by laser-scanning confocal polarized micro-raman spectroscopy. *Angewandte Chemie International Edition*, 50(37):8697–8701, 2011.

[28] Pedro Atienzar, Susana Valencia, Avelino Corma, and Hermenegildo García. Titanium-containing zeolites and microporous molecular sieves as photovoltaic solar cells. *ChemPhysChem*, 8(7):1115–1119, 2007.

[29] Francesc X. Llabrés i Xamena, Paola Calza, Carlo Lamberti, Carmelo Prestipino, Alessandro Damin, Silvia Bordiga, Ezio Pelizzetti, and Adriano Zecchina. Enhancement of the ets-10 titanosilicate activity in the shape-selective photocatalytic degradation of large aromatic molecules by controlled defect production. *Journal of the American Chemical Society*, 125(8):2264–2271, 2003. PMID: 12590556.

[30] Guoqing Guan, Tetsuya Kida, Katsuki Kusakabe, Kunio Kimura, Eiichi Abe, and Akira Yoshida. Photocatalytic activity of cds nanoparticles incorporated in titanium silicate molecular sieves of ets-4 and ets-10. *Applied Catalysis A: General*, 295(1):71 – 78, 2005.

[31] Pedro Atienzar, Susana Valencia, Avelino Corma, and Hermenegildo García. Titanium-containing zeolites and microporous molecular sieves as photovoltaic solar cells. *ChemPhysChem*, 8(7):1115–1119, 2007.

[32] Sezin Galioğlu, Mehmet Zahmakıran, Y. Eren Kalay, Saim Özkar, and Burcu Akata. Effect of silver encapsulation on the local structure of titanosilicate ets-10. *Microporous and Mesoporous Materials*, 159(0):1 – 8, 2012.

[33] Bilge Yilmaz, Juliusz Warzywoda, and Albert Sacco. Spectroscopic characterization of the quantum wires in titanosilicates ETS-4 and ETS-10. *Nanotechnology*, 17(16):4092–4099, August 2006.

[34] Lu Lv, Fabing Su, and X.S. Zhao. A reinforced study on the synthesis of microporous titanosilicate ets-10. *Microporous and Mesoporous Materials*, 76(1–3):113 – 122, 2004.

[35] W. Kohn and L. J. Sham. Self-consistent equations including exchange and correlation effects. *Phys. Rev.*, 140:A1133–A1138, Nov 1965.

[36] F. Bloch. Bemerkung zur elektronentheorie des ferromagnetismus und der elektrischen leitfähigkeit. *Zeitschrift für Physik*, 57(7-8):545–555, 1929.

[37] D. M. Ceperley and B. J. Alder. Ground state of the electron gas by a stochastic method. *Phys. Rev. Lett.*, 45:566–569, Aug 1980.

[38] Joachim Paier, Robin Hirschl, Martijn Marsman, and Georg Kresse. The perdew–burke–ernzerhof exchange-correlation functional applied to the g2-1 test set using a plane-wave basis set. *The Journal of Chemical Physics*, 122(23):234102, 2005.

[39] Brian O'Regan and Michael Gratzel. A low-cost, high-efficiency solar cell based on dye-sensitized colloidal tio2 films. *Nature*, 353(6346):737–740, Oct 1991.

[40] Aswani Yella, Hsuan-Wei Lee, Hoi Nok Tsao, Chenyi Yi, Aravind Kumar Chandiran, Md.Khaja Nazeeruddin, Eric Wei-Guang Diau, Chen-Yu Yeh, Shaik M Zakeeruddin, and Michael Grätzel. Porphyrin-sensitized solar cells with cobalt (ii/iii)–based redox electrolyte exceed 12 percent efficiency. *Science*, 334(6056):629–634, 2011.

[41] Michael Grätzel. Corrigendum to "conversion of sunlight to electric power by nanocrystalline dye-sensitized solar cells" [j. photochem. photobiol. a: Chem. 164 (2004) 3–14]. *Journal of Photochemistry and Photobiology A: Chemistry*, 168(3):235 –, 2004.

[42] Masaru Saito and Shinobu Fujihara. Large photocurrent generation in dye-sensitized zno solar cells. *Energy Environ. Sci.*, 1:280–283, 2008.

[43] ElizabethA. Gibson, AmandaL. Smeigh, Loïc LePleux, Jérôme Fortage, Gerrit Boschloo, Errol Blart, Yann Pellegrin, Fabrice Odobel, Anders Hagfeldt, and Leif Hammarström. A p-type nio-based dye-sensitized solar cell with an open-circuit voltage of 0.35v. *Angewandte Chemie International Edition*, 48(24):4402–4405, 2009.

[44] Saif A. Haque, Emilio Palomares, Byung M. Cho, Alex N. M. Green, Narukuni Hirata, David R. Klug, and James R. Durrant. Charge separation versus recombination in dye-sensitized nanocrystalline solar cells: the minimization of kinetic redundancy. *Journal of the American Chemical Society*, 127(10):3456–3462, 2005. PMID: 15755165.

[45] Peng Wang, Shaik M. Zakeeruddin, Pascal Comte, Ivan Exnar, and Michael Grätzel. Gelation of ionic liquid-based electrolytes with silica nanoparticles for quasi-solid-state dye-sensitized solar cells. *Journal of the American Chemical Society*, 125(5):1166–1167, 2003.

[46] Gerrit Boschloo and Anders Hagfeldt. Characteristics of the iodide/triiodide redox mediator in dye-sensitized solar cells. *Accounts of Chemical Research*, 42(11):1819–1826, 2009. PMID: 19845388.

[47] Peng Wang, Shaik M. Zakeeruddin, Jacques E. Moser, Mohammad K. Nazeeruddin, Takashi Sekiguchi, and Michael Gratzel. A stable quasi-solid-state dye-sensitized solar cell with an amphiphilic ruthenium sensitizer and polymer gel electrolyte. *Nat Mater*, 2(6):402–407, Jun 2003.

[48] M. K. Nazeeruddin, A. Kay, I. Rodicio, R. Humphry-Baker, E. Mueller, P. Liska, N. Vlachopoulos, and M. Graetzel. Conversion of light to electricity by cis-X2bis(2,2'-bipyridyl-4,4'-dicarboxylate)ruthenium(II) charge-transfer sensitizers (X = Cl-, Br-, I-, CN-, and SCN-) on nanocrystalline titanium dioxide electrodes. *Journal of the American Chemical Society*, 115(14):6382–90, 1993.

[49] Jong Kwan Koh, Jeonghun Kim, Byeonggwan Kim, Jong Hak Kim, and Eunkyoung Kim. Highly efficient, iodine-free dye-sensitized solar cells with solid-state synthesis of conducting polymers. *Advanced Materials*, 23(14):1641–1646, 2011.

[50] P. Hohenberg and W. Kohn. Inhomogeneous electron gas. *Phys. Rev.*, 136(3B):B864–B871, Nov 1964.

[51] David Vanderbilt. Soft self-consistent pseudopotentials in a generalized eigenvalue formalism. *Phys. Rev. B*, 41(11):7892–7895, Apr 1990.

[52] John P. Perdew, Kieron Burke, and Matthias Ernzerhof. Generalized gradient approximation made simple. *Phys. Rev. Lett.*, 77(18):3865–3868, Oct 1996.

[53] Paolo Giannozzi, Stefano Baroni, Nicola Bonini, Matteo Calandra, Roberto Car, Carlo Cavazzoni, Davide Ceresoli, Guido L Chiarotti, Matteo Cococcioni, Ismaila Dabo, Andrea Dal Corso, Stefano de Gironcoli, Stefano Fabris, Guido Fratesi, Ralph Gebauer, Uwe Gerstmann, Christos Gougoussis, Anton Kokalj, Michele Lazzeri, Layla Martin-Samos, Nicola Marzari, Francesco Mauri, Riccardo Mazzarello, Stefano Paolini, Alfredo Pasquarello, Lorenzo Paulatto, Carlo Sbraccia, Sandro Scandolo, Gabriele Sclauzero, Ari P Seitsonen, Alexander Smogunov, Paolo Umari, and Renata M Wentzcovitch. Quantum espresso: a modular and open-source software project for quantum simulations of materials. *Journal of Physics: Condensed Matter*, 21(39):395502, 2009.

[54] Anton Kokalj. Computer graphics and graphical user interfaces as tools in simulations of matter at the atomic scale. *Computational Materials Science*, 28(2):155 – 168, 2003.

[55] Alessandro Damin, Francesc X Llabre, Bartolomeo Civalleri, Claudio M Zicovich-wilson, and Adriano Zecchina. Structural , Electronic , and Vibrational Properties of the Ti-O-Ti Quantum Wires in the. *Journal of Physical Chemistry B*, pages 1328–1336, 2004.

[56] Hendrik J. Monkhorst and James D. Pack. Special points for brillouin-zone integrations. *Phys. Rev. B*, 13(12):5188–5192, Jun 1976.

[57] S. M. Kuznicki. Large-pored crystalline titanium molecular sieve zeolites, 08 1989.

[58] Xiqu Wang and Allan J Jacobson. Crystal structure of the microporous titanosilicate ETS-10 refined from single crystal X-ray diffraction data. *Chem Commun*, 612(001):973–974, 1999.

[59] Anne Marie Zimmerman, Douglas J Doren, and Raul F Lobo. Electronic and geometric properties of ETS-10: QM/MM studies of cluster models. *The journal of physical chemistry. B*, 110(18):8959–64, May 2006.

[60] C. Lamberti. Electron–hole reduced effective mass in monoatomic . . . –O–Ti–O–Ti–O–. . . quantum wires embedded in the siliceous crystalline matrix of ETS-10. *Microporous and Mesoporous Materials*, 30(1):155–163, August 1999.

[61] W. Y. Ching, Y.-N. Xu, and Z.-q. Gu. *PHYSICAL REVIEW B*, 54(22):585–589, 1996.

[62] ME Grillo and J Carrazza. Computational Modeling of the Nonframework Cation Location and Distribution in Microporous Titanosilicate ETS-10. *The Journal of Physical Chemistry*, 3654(95):12261–12264, 1996.

[63] Michael W. Anderson, Jonathan R. Agger, Donat-Pierre Luigi, Anthony K. Baggaley, and Joao Rocha. Cation sites in ets-10: 23na 3q mas nmr and lattice energy minimisation calculations. *Phys. Chem. Chem. Phys.*, 1:2287–2292, 1999.

[64] Claudiu C Pavel, Bodo Zibrowius, Elke Löffler, and Wolfgang Schmidt. On the influence of ion exchange on the local structure of the titanosilicate ETS-10. *Physical chemistry chemical physics : PCCP*, 9(26):3440–6, July 2007.

[65] Claudiu C. Pavel, So-Hyun Park, Axel Dreier, Bernd Tesche, and Wolfgang Schmidt. Structural Defects Induced in ETS-10 by Postsynthesis Treatment with H2O2 Solution. *ChemInform*, 37(43):3813–3820, October 2006.

[66] Suresh B. Waghmode, Rajappan Vetrivel, Suryakant G. Hegde, Chinnakonda S. Gopinath, and Subramanian Sivasanker. Physicochemical Investigations of the Basicity of the Cation Exchanged ETS-10 Molecular Sieves. *The Journal of Physical Chemistry B*, 107(33):8517–8523, August 2003.

[67] a Philippou. Aldol-Type Reactions over Basic Microporous Titanosilicate ETS-10 Type Catalysts. *Journal of Catalysis*, 189(2):395–400, January 2000.

[68] a Valente. Gas-Phase Oxidative Dehydrogenation of Cyclohexanol over ETS-10 and Related Materials. *Journal of Catalysis*, 200(1):99–105, May 2001.

[69] Eric J Doskocil. Effect of water and alkali modifications on ETS-10 for the cycloaddition of CO2 to propylene oxide. *The journal of physical chemistry. B*, 109(6):2315–20, February 2005.

[70] C.B. Lopes, M. Otero, J. Coimbra, E. Pereira, J. Rocha, Z. Lin, and a. Duarte. Removal of low concentration Hg2+ from natural waters by microporous and layered titanosilicates. *Microporous and Mesoporous Materials*, 103(1-3):325–332, June 2007.

[71] Yong-Nian Xu, W. Y. Ching, and Zong-Quan Gu. Electronic structure of microporous titanosilicate ets-10. *Ferroelectrics*, 194(1):219–226, 1997.

[72] S. Bordiga, G. Turnes Palomino, a. Zecchina, G. Ranghino, E. Giamello, and C. Lamberti. Stoichiometric and sodium-doped titanium silicate molecular sieve containing atomically defined –OTiOTiO– chains: Quantum ab initio calculations, spectroscopic properties, and reactivity. *The Journal of Chemical Physics*, 112(8):3859, 2000.

[73] Nak Cheon Jeong, Young Ju Lee, Jung-Hyun Park, Hyunjin Lim, Chae-Ho Shin, Hyeonsik Cheong, and Kyung Byung Yoon. New insights into ETS-10 and titanate quantum wire: a comprehensive characterization. *Journal of the American Chemical Society*, 131(36):13080–92, September 2009.

[74] Gopinathan Sankar, Robert G Bell, John Meurig Thomas, Michael W Anderson, and Paul A Wright. Determination of the Structure of Distorted TiO 6 Units in the Titanosilicate ETS-10 by a Combination of X-ray Absorption Spectroscopy and Computer Modeling. 92:449–452, 1996.

[75] C Prestipino, P L Solari, and C Lamberti. EXAFS and XANES investigation of the ETS-10 microporous titanosilicate. *The journal of physical chemistry. B*, 109(27):13132–7, July 2005.

[76] Anne Marie Shough, Douglas J. Doren, and Babatunde Ogunnaike. Transition Metal Substitution in ETS-10: DFT Calculations and a Simple Model for Electronic Structure Prediction. *Chemistry of Materials*, 21(7):1232–1241, April 2009.

[77] Enzo Borello, Carlo Lamberti, Silvia Bordiga, Adriano Zecchina, and Carlos Otero Arean. Quantum-size effects in the titanosilicate molecular sieve. *Applied Physics Letters*, 71(16):2319–2321, 1997.

[78] Peter D. Southon and Russell F. Howe. Spectroscopic Studies of Disorder in the Microporous Titanosilicate ETS-10. *Chemistry of Materials*, 14(10):4209–4218, October 2002.

[79] F. X. Llabres i Xamena, A. Damin, S. Bordiga, and A. Zecchina. Healing of defects in ets-10 by selective uv irradiation: a raman study. *Chem. Commun.*, 0:1514–1515, 2003.

[80] Yali Su, Mari Lou Balmer, and Bruce C. Bunker. Raman spectroscopic studies of silicotitanates. *The Journal of Physical Chemistry B*, 104(34):8160–8169, 2000.

[81] David Segev, Anderson Janotti, and Chris G. Van de Walle. Self-consistent band-gap corrections in density functional theory using modified pseudopotentials. *Phys. Rev. B*, 75:035201, Jan 2007.

[82] Linus Pauling. The George Fisher Baker Non-Resident Lectureship in Chemistry at Cornell University, third edition, 1960.

[83] Leland C. Allen. Electronegativity is the average one-electron energy of the valence-shell electrons in ground-state free atoms. *Journal of the American Chemical Society*, 111(25):9003–9014, 1989.

[84] L.H. Ahrens. The use of ionization potentials part 1. ionic radii of the elements. *Geochimica et Cosmochimica Acta*, 2(3):155 – 169, 1952.

[85] R. D. Shannon. Revised effective ionic radii and systematic studies of interatomic distances in halides and chalcogenides. *Acta Crystallographica Section A*, 32(5):751–767, 1976.

[86] C. Barolo, Md. K. Nazeeruddin, Simona Fantacci, D. Di Censo, P. Comte, P. Liska, G. Viscardi, P. Quagliotto, Filippo De Angelis, S. Ito, and M. Grätzel. Synthesis, characterization, and dft-tddft computational study of a ruthenium complex containing a functionalized tetradentate ligand. *Inorganic Chemistry*, 45(12):4642–4653, 2006.

[87] LuLvFabing Su and X.S. Zhao. Synthesis and characterization of microporous titanosilicate ets-10 with different titanium precursors. *Journal of Porous Materials*, 13(3-4):263–267, 2006.

[88] L. Lv, J. K. Zhou, F. Su, and X. S. Zhao. Local structure changes of microporous titanosilicate ets-10 upon acid treatment. *The Journal of Physical Chemistry C*, 111(2):773–778, 2007.

APPENDIX A

MODELLING RESULTS:SUPPORTING INFORMATION

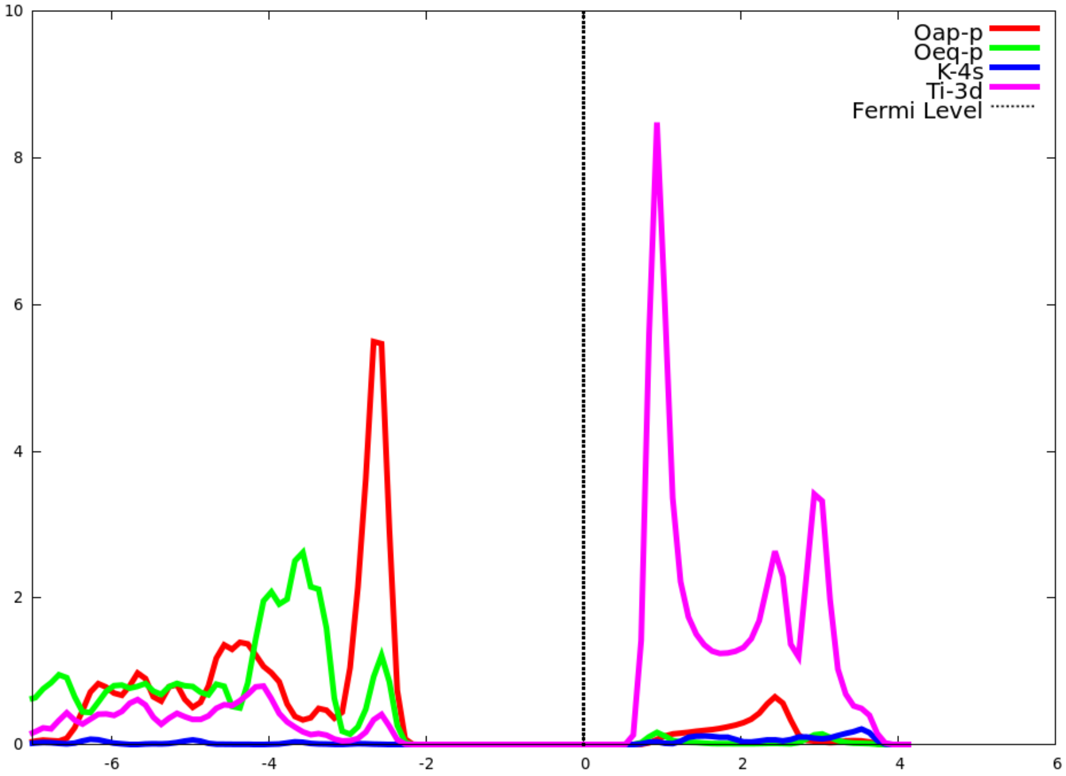

Figure A.1: DOS Analysis of K-ETS-10

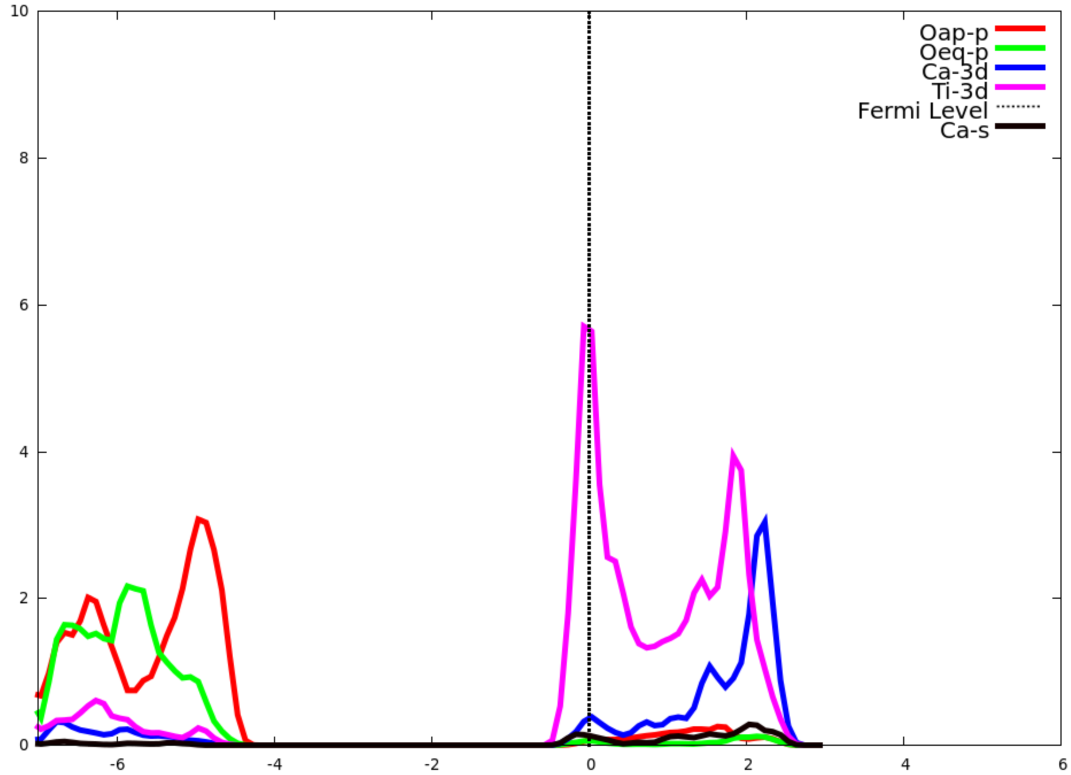

Figure A.2: DOS Analysis of Ca-ETS-10

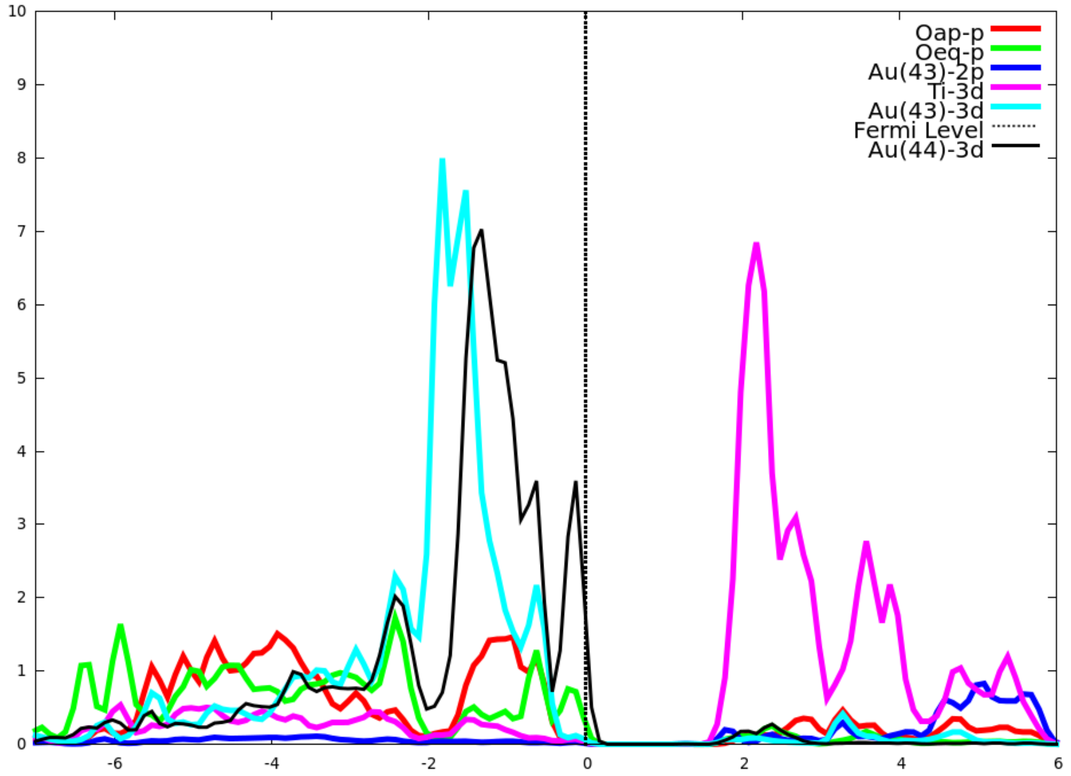

Figure A.3: DOS Analysis of Au-ETS-10

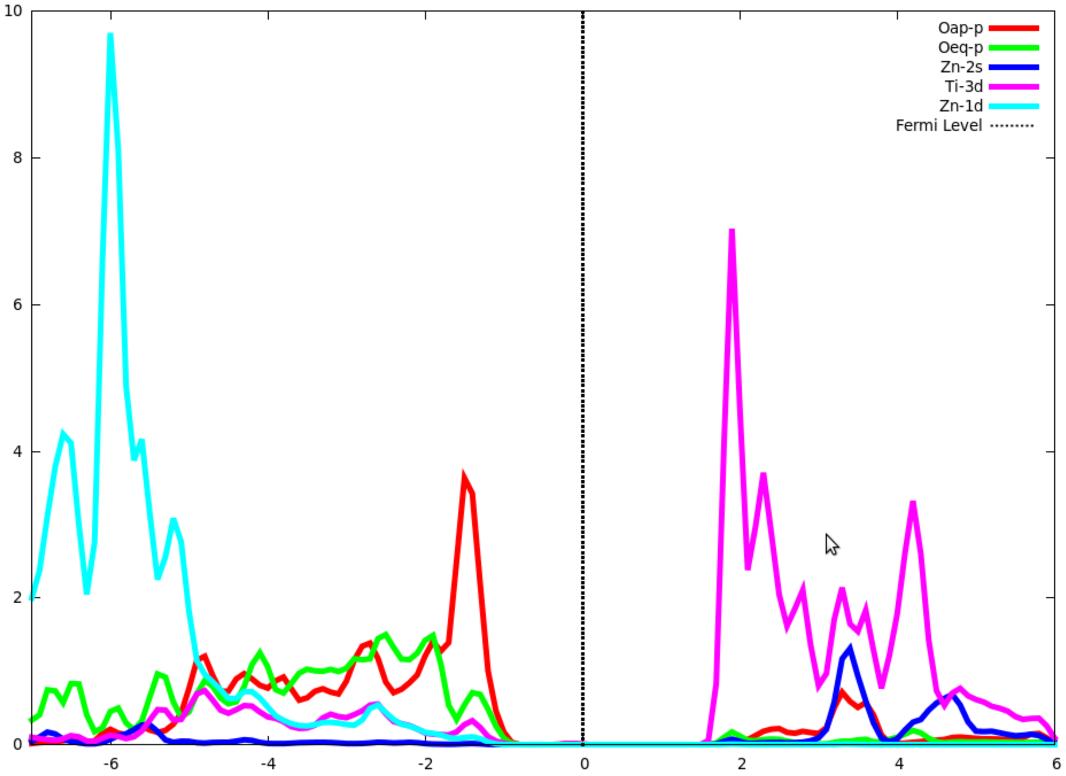

Figure A.4: DOS Analysis of Zn-ETS-10

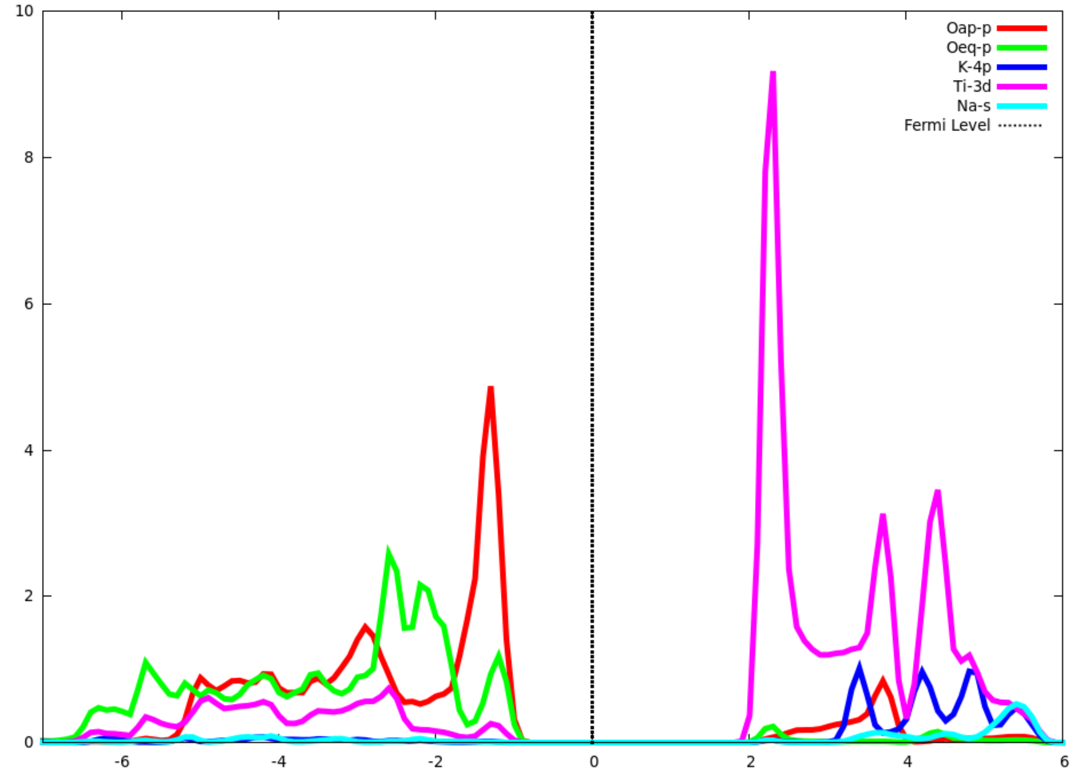

Figure A.5: DOS Analysis of [Na,K]-ETS-10

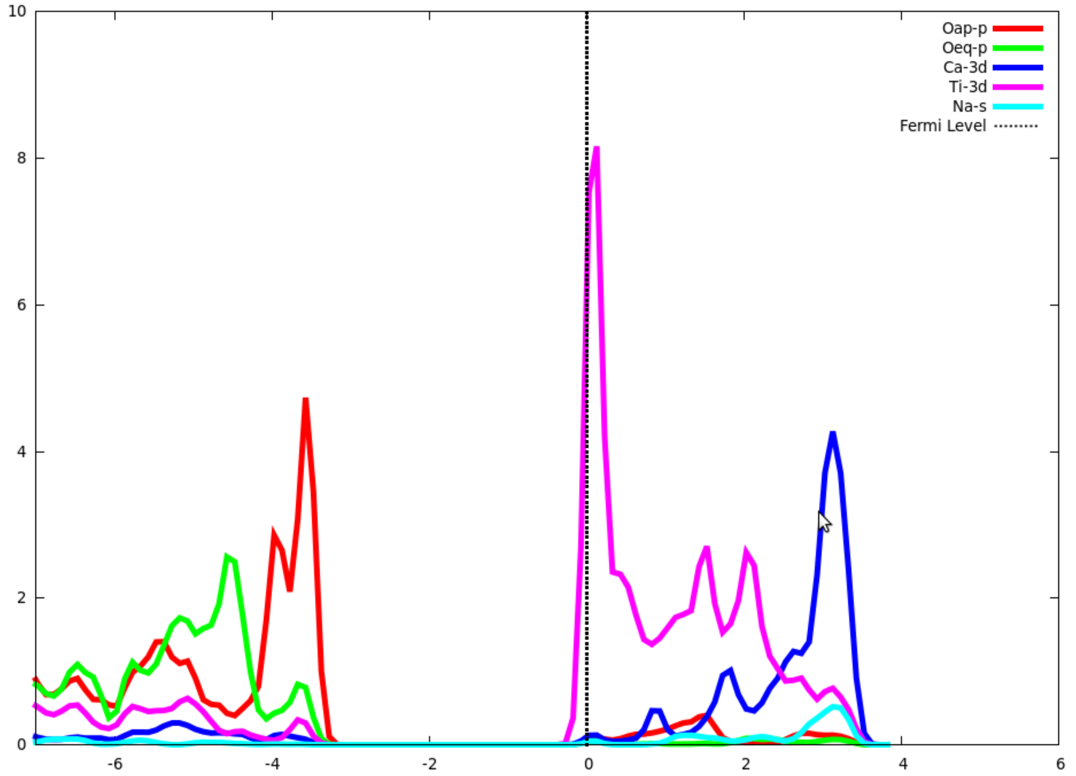

Figure A.6: DOS Analysis of [Na,Ca]-ETS-10

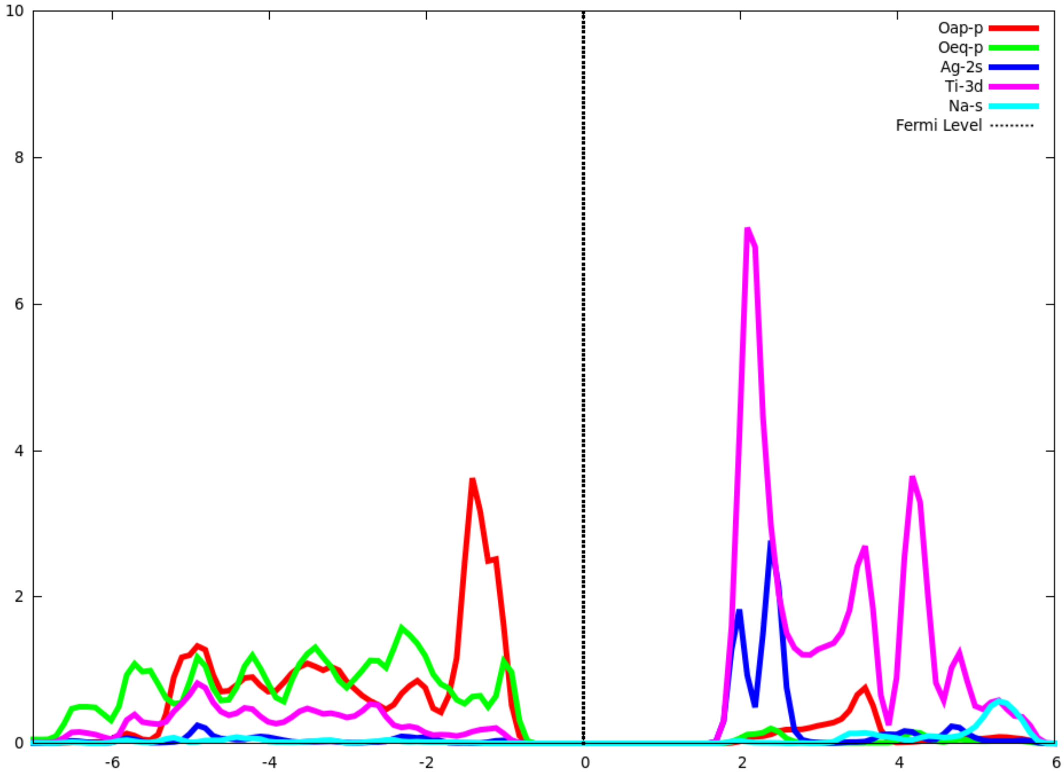

Figure A.7: DOS Analysis of [Na,Ag]-ETS-10

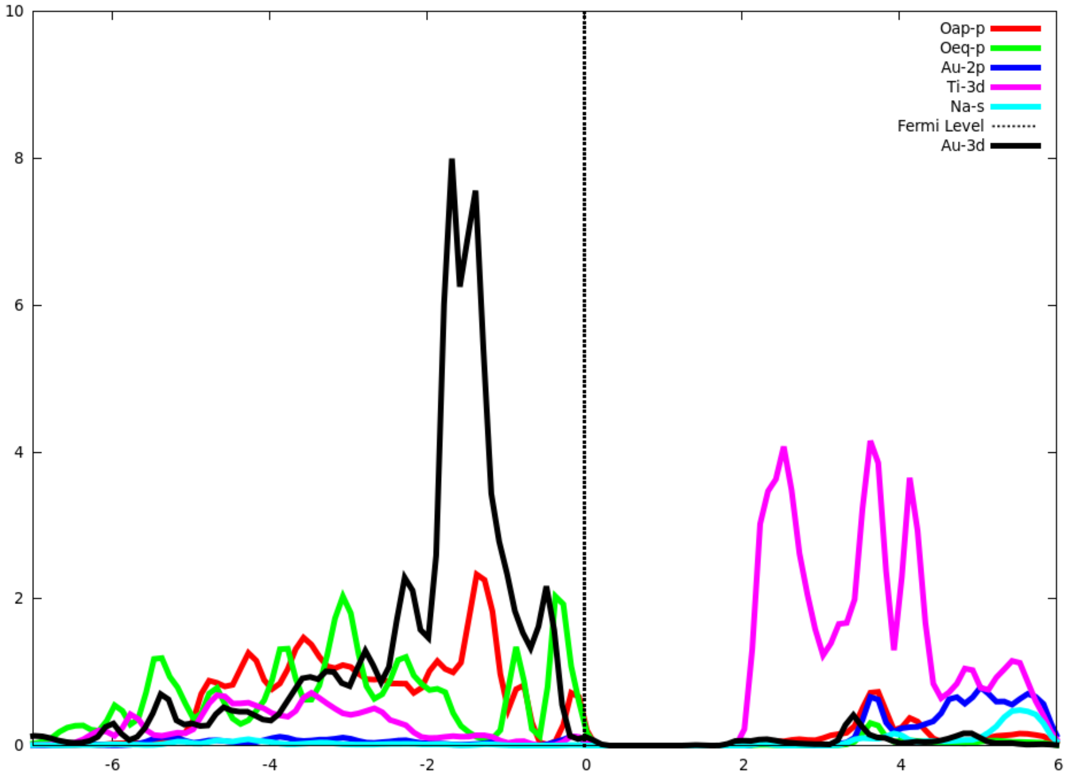

Figure A.8: DOS Analysis of [Na,Au]-ETS-10

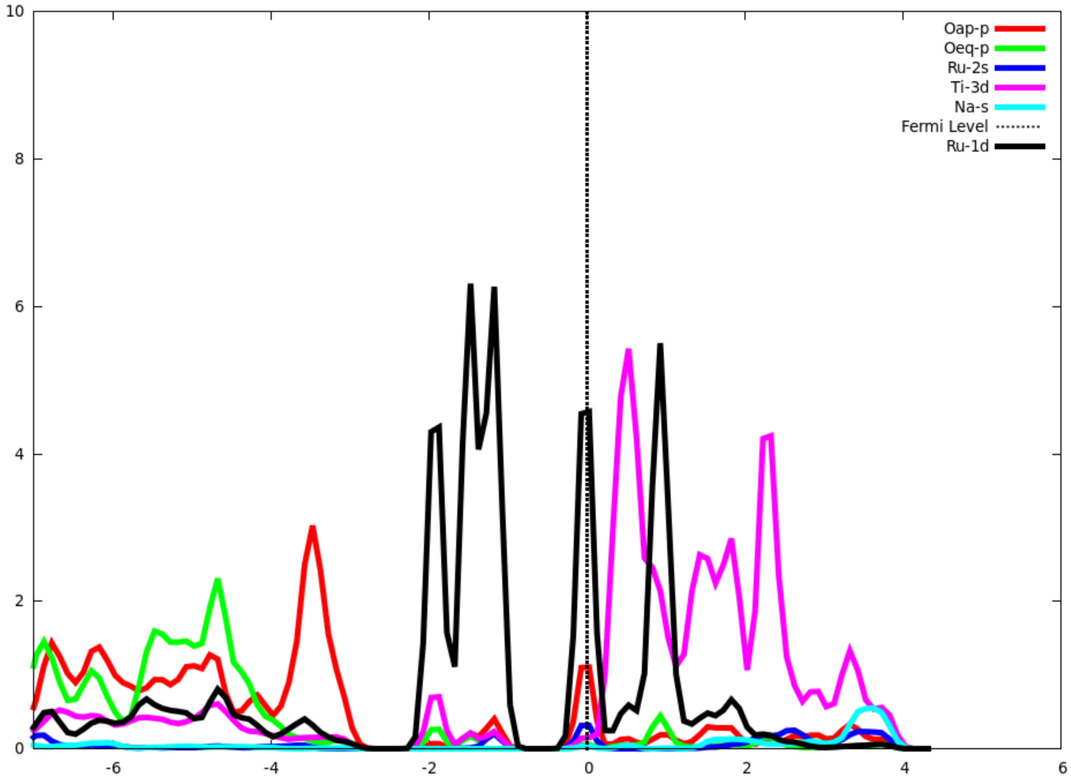

Figure A.9: DOS Analysis of [Na,Ru]-ETS-10

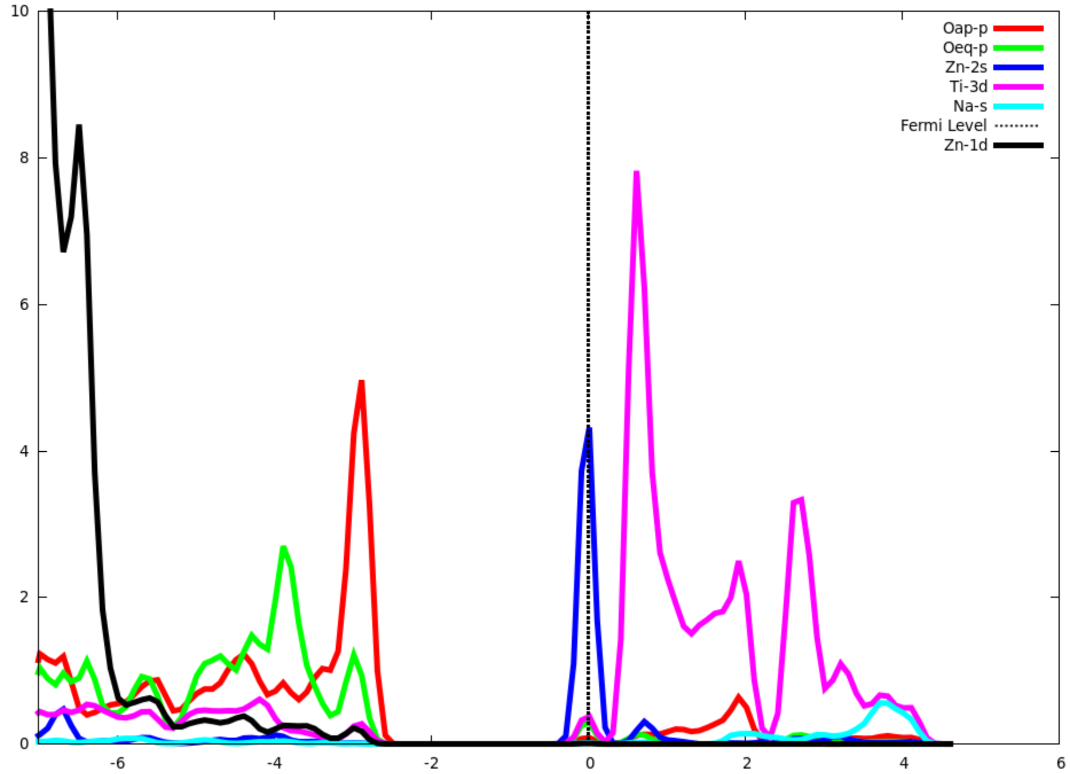

Figure A.10: DOS Analysis of [Na,Zn]-ETS-10

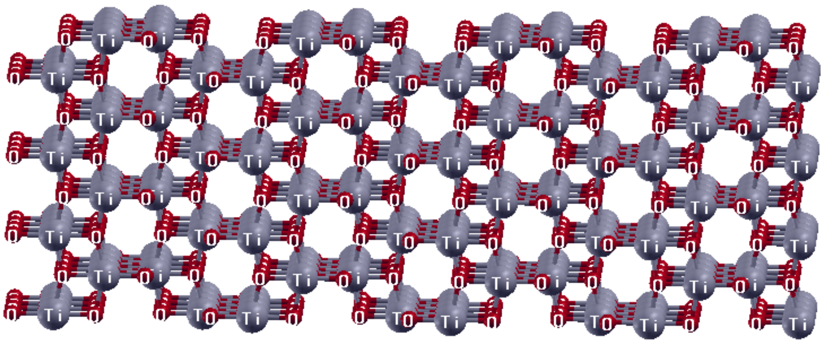

Figure A.11: Modelled TiO_2, Calculated Band Gap is 2.14 eV

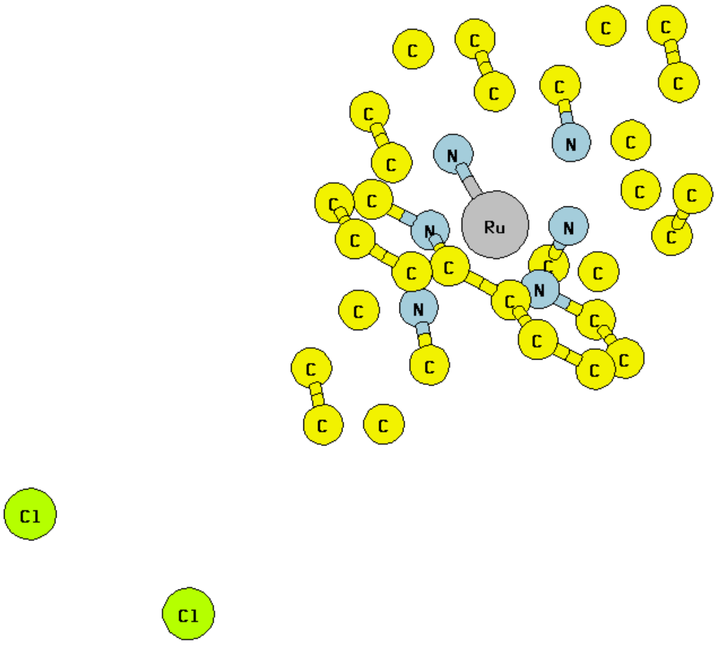

Figure A.12: Tris(bipyridine)ruthenium(II) chloride

APPENDIX B

EXPERIMENTAL RESULTS:SUPPORTING INFORMATION

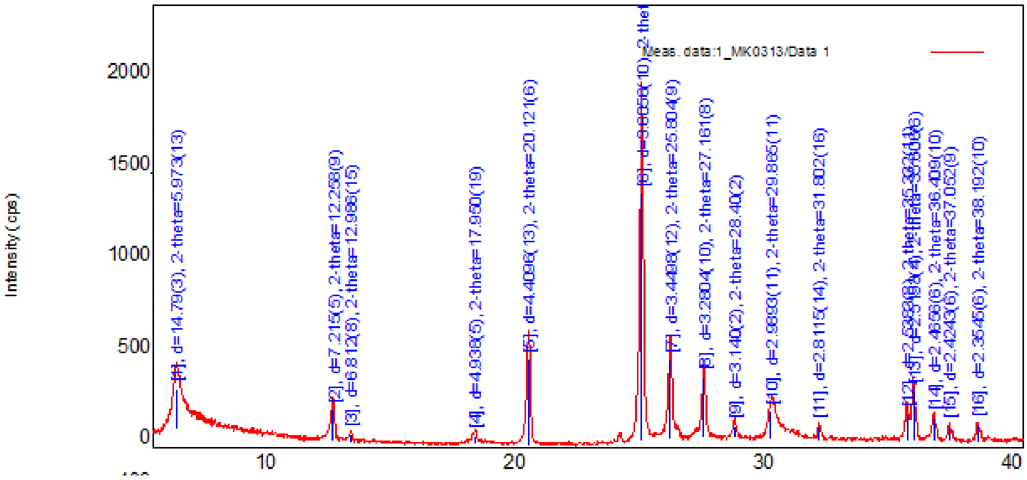

Figure B.1: XRD Spectrum of ETS-10

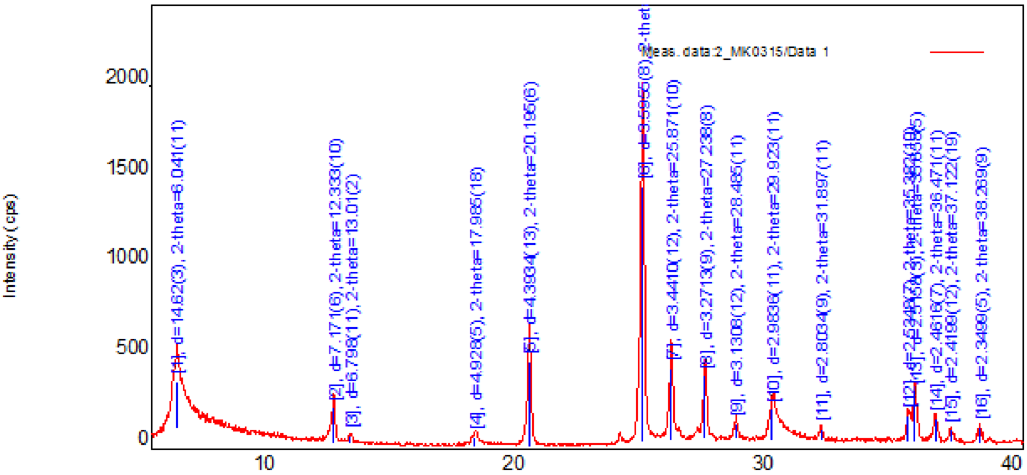

Figure B.2: XRD Spectrum of ETS-10

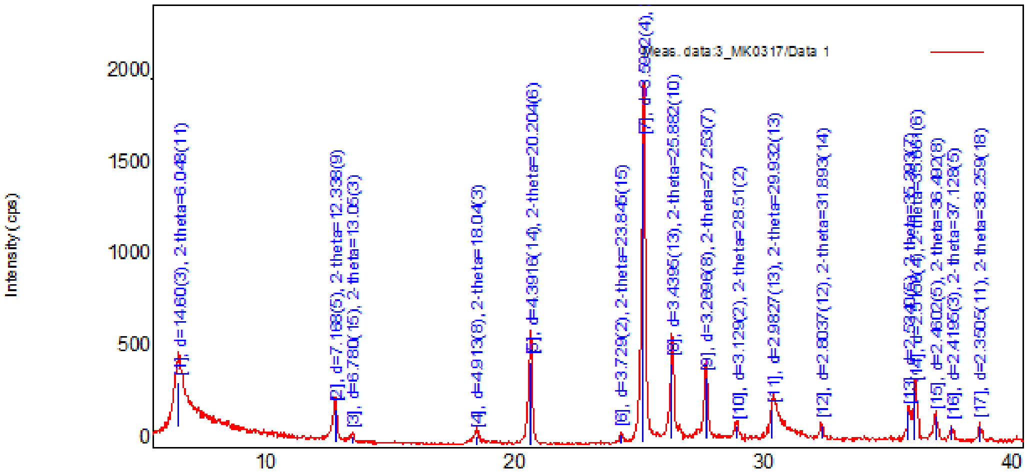

Figure B.3: XRD Spectrum of ETS-10

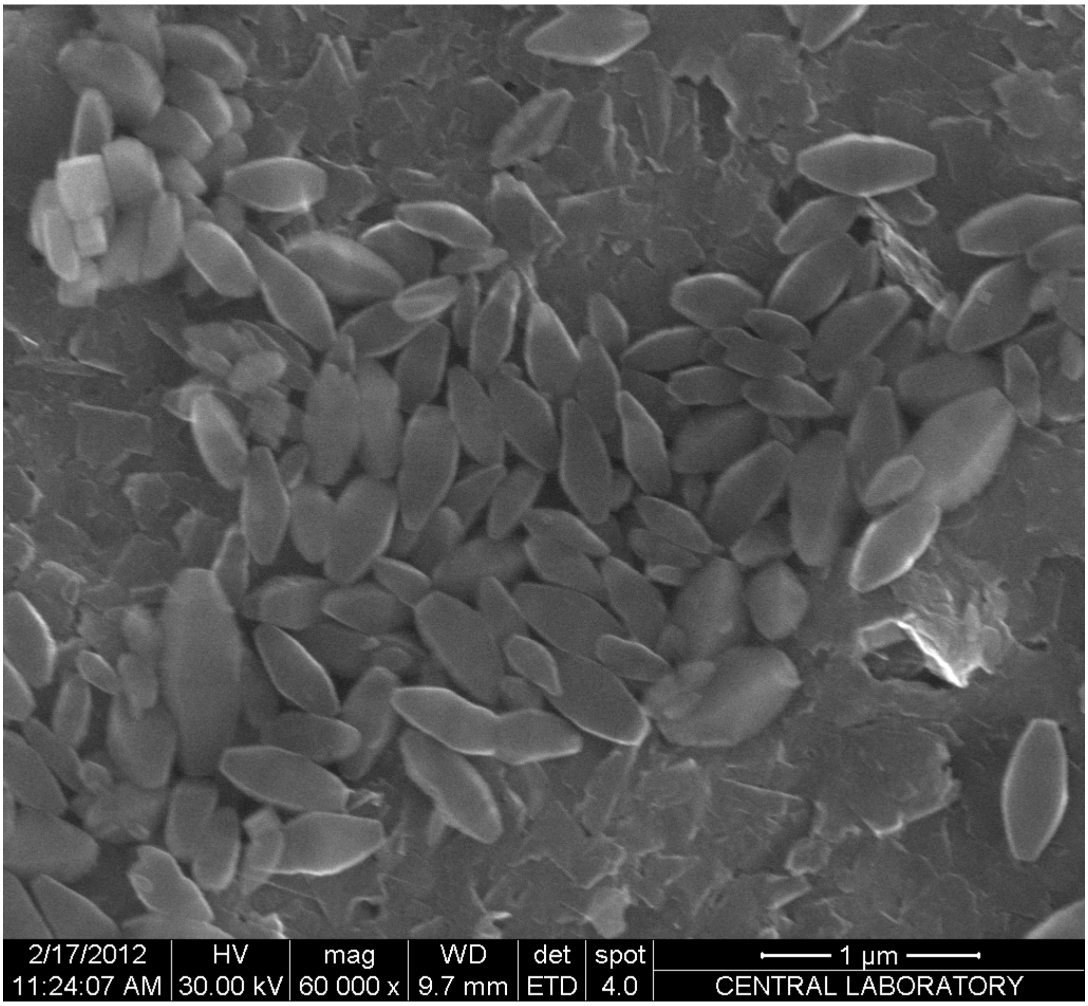

Figure B.4: SEM Picture of ETS-10

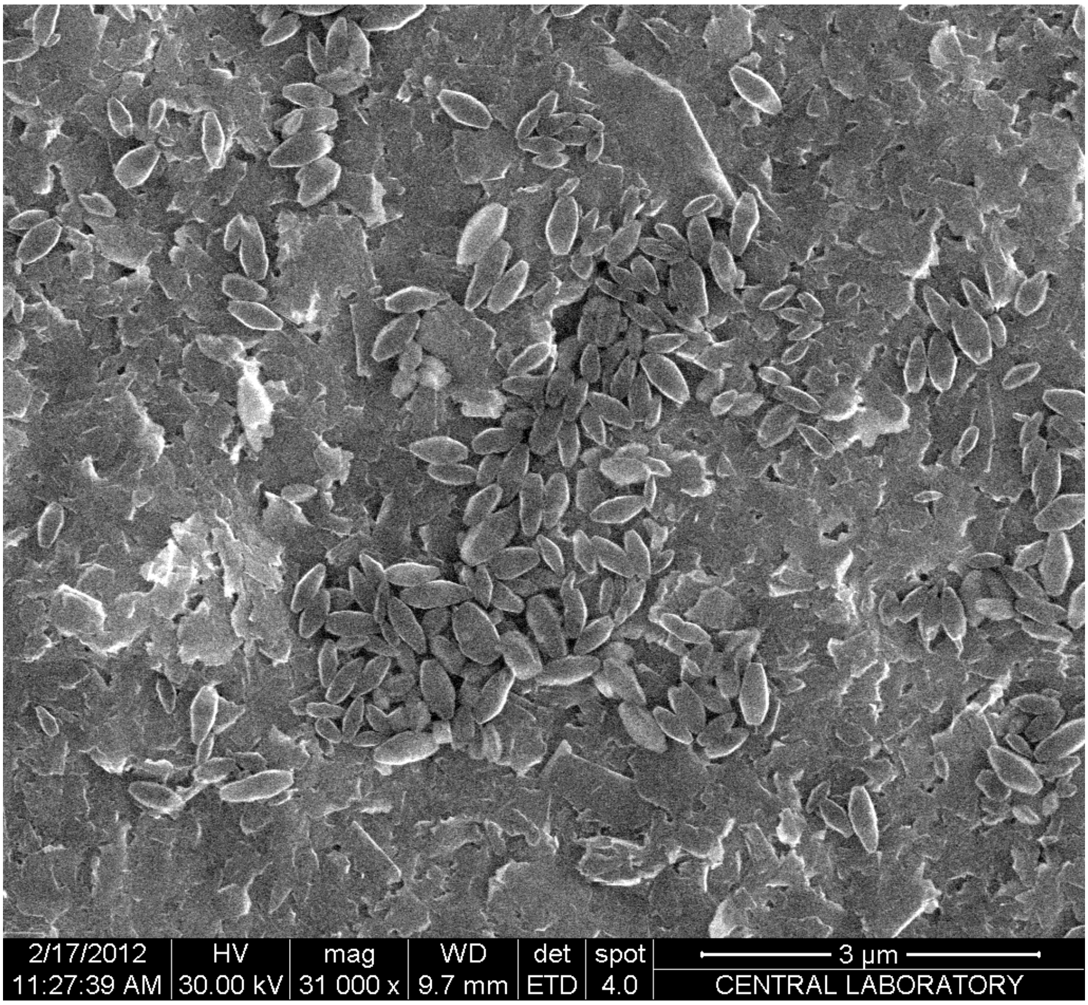

Figure B.5: SEM Picture of ETS-10

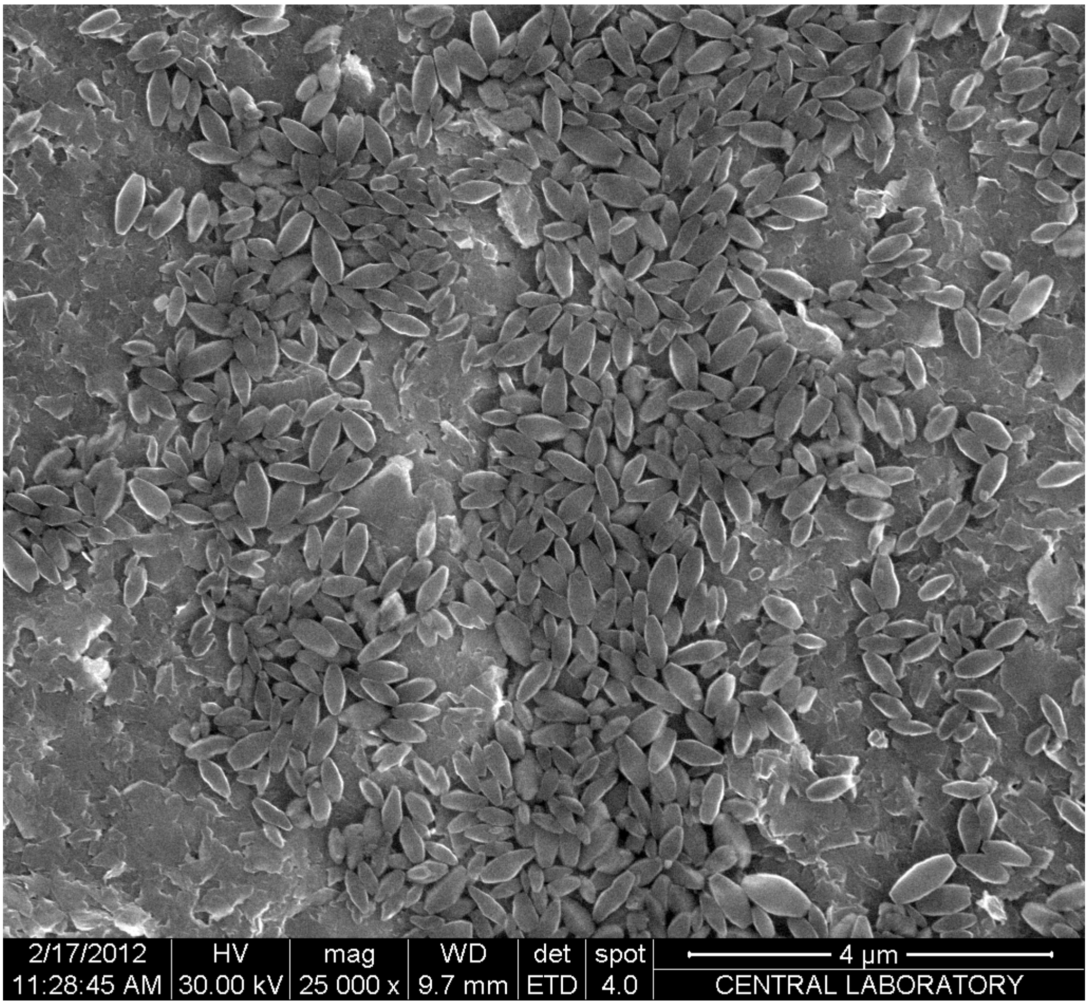

Figure B.6: SEM Picture of ETS-10

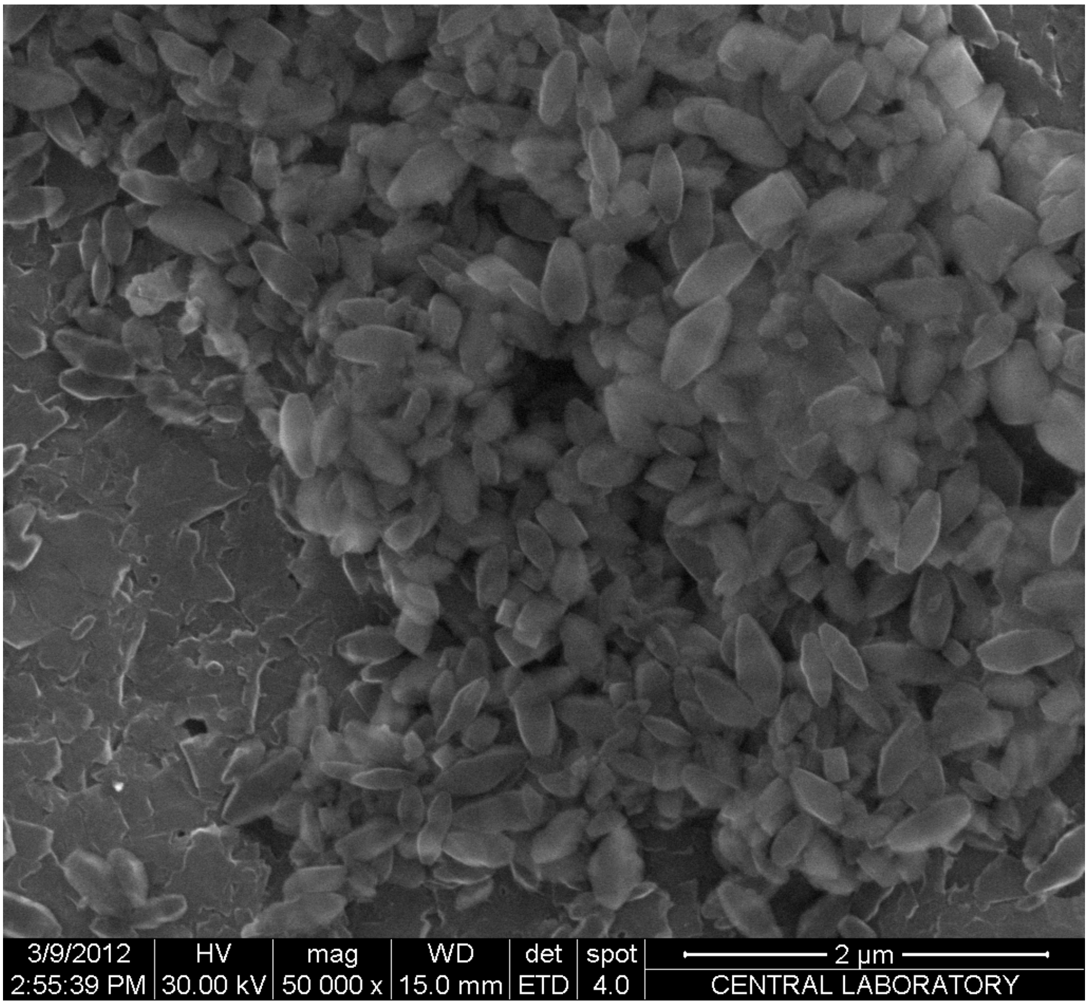

Figure B.7: SEM Picture of ETS-10

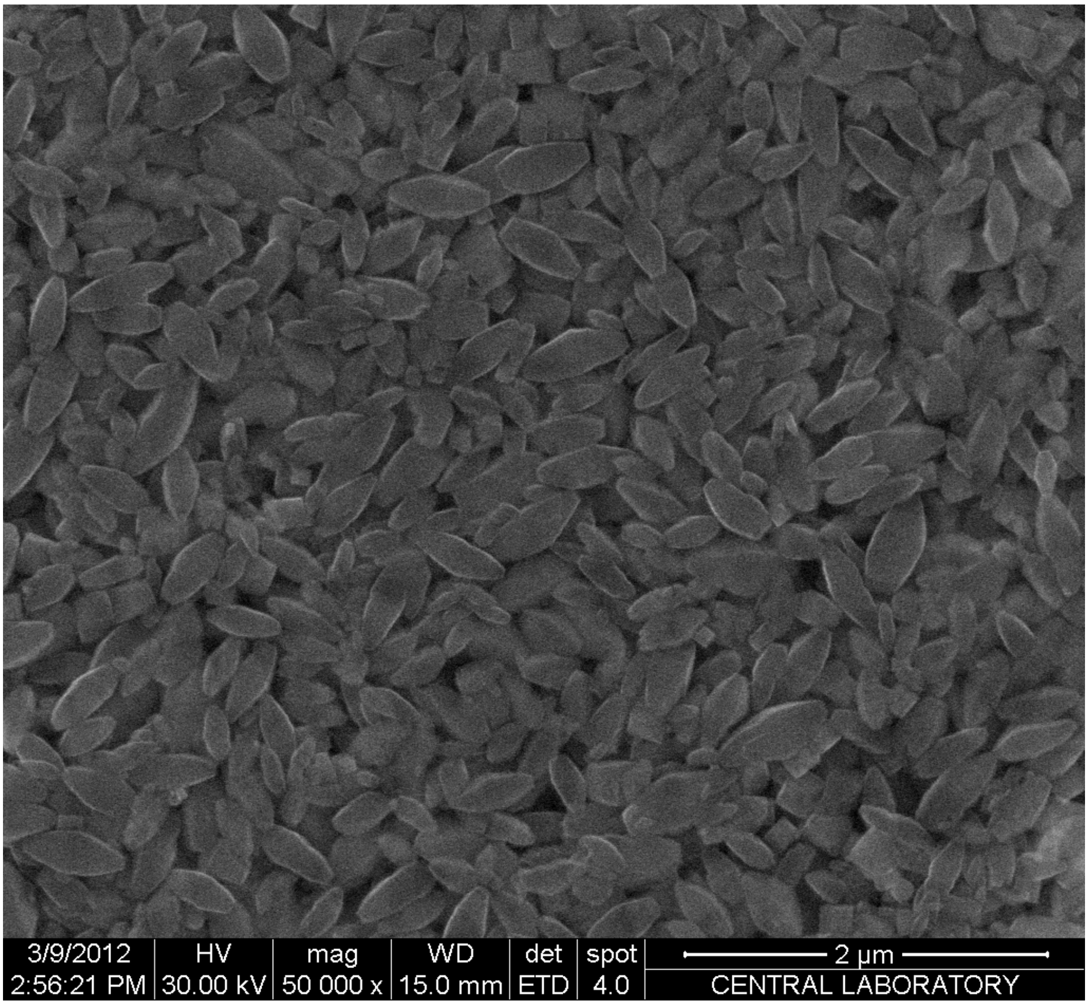

Figure B.8: SEM Picture of ETS-10

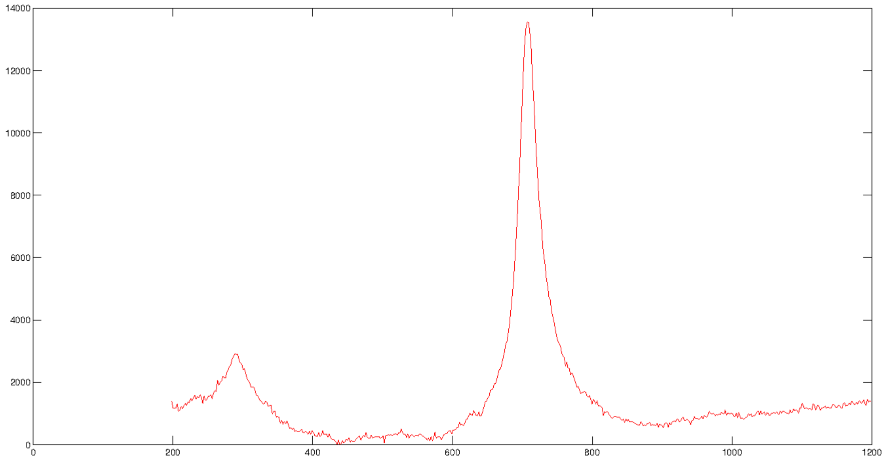

Figure B.9: Ag-ETS-10 Raman Results

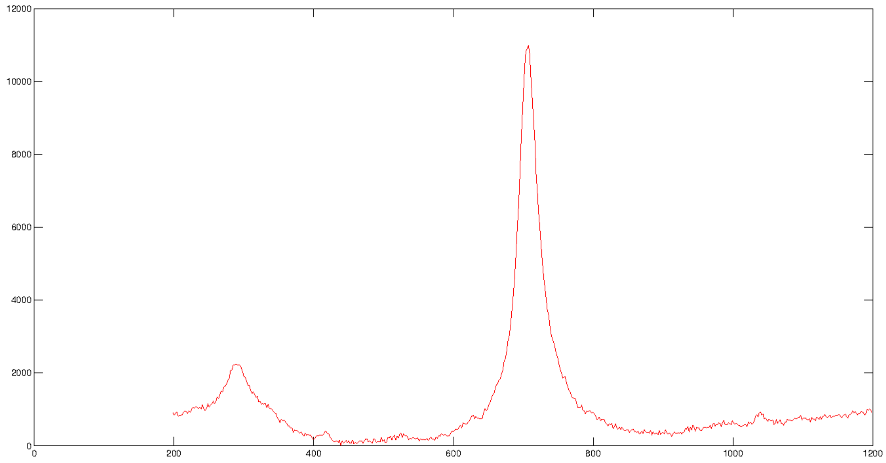

Figure B.10: Ion Exchanged Continued with Ag-ETS-10 Raman Results

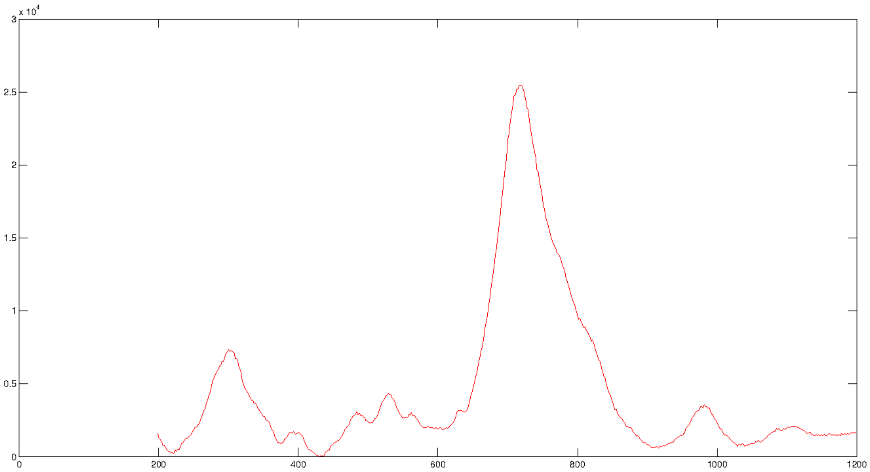

Figure B.11: Ca-ETS-10 Raman Results

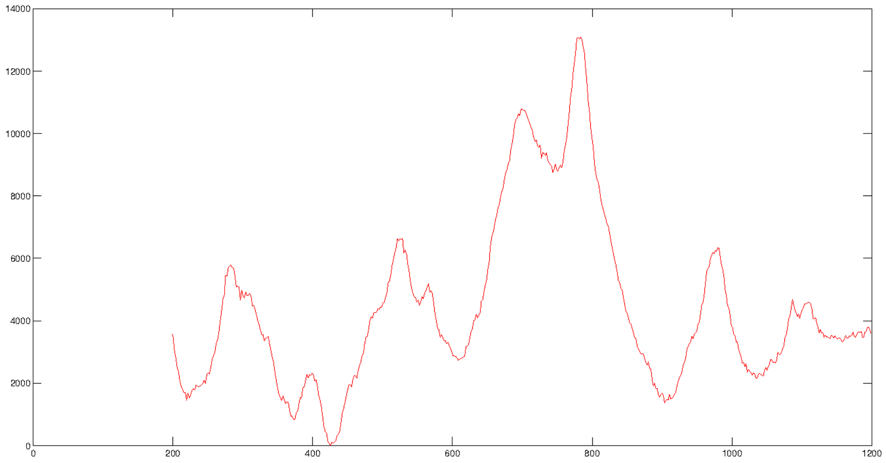

Figure B.12: Ion Exchanged Continued with Ca-ETS-10 Raman Results

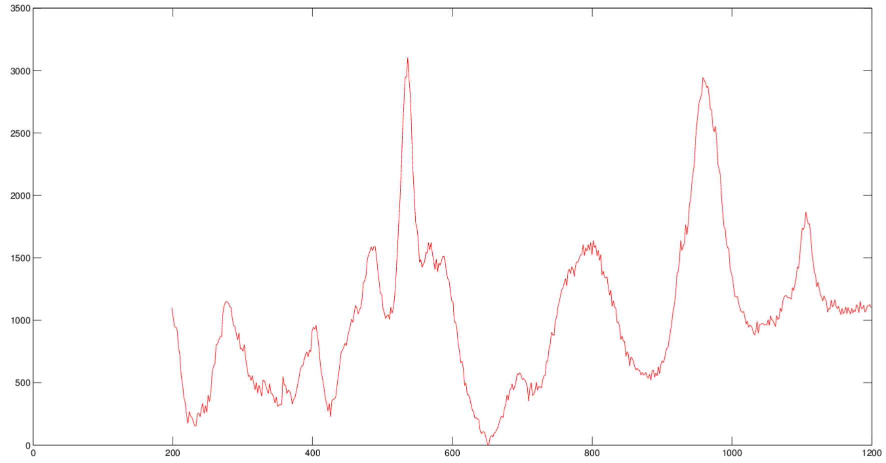

Figure B.13: Zn-ETS-10 Raman Results

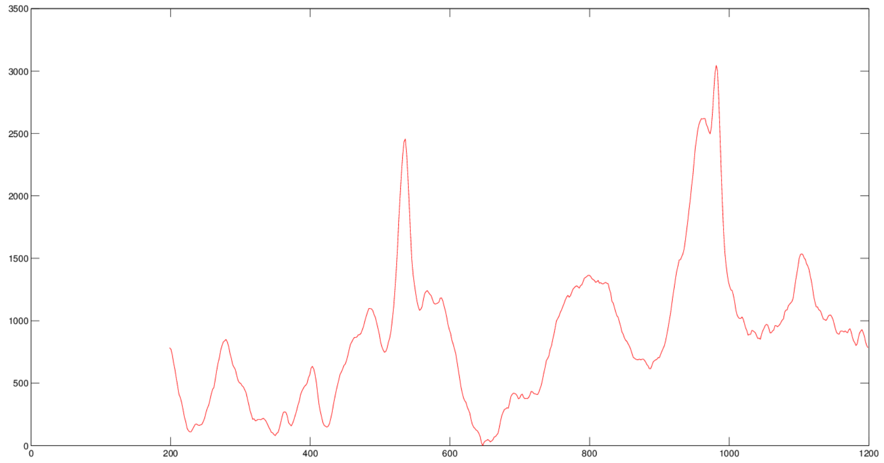

Figure B.14: Ion Exchanged Continued with Zn-ETS-10 Raman Results

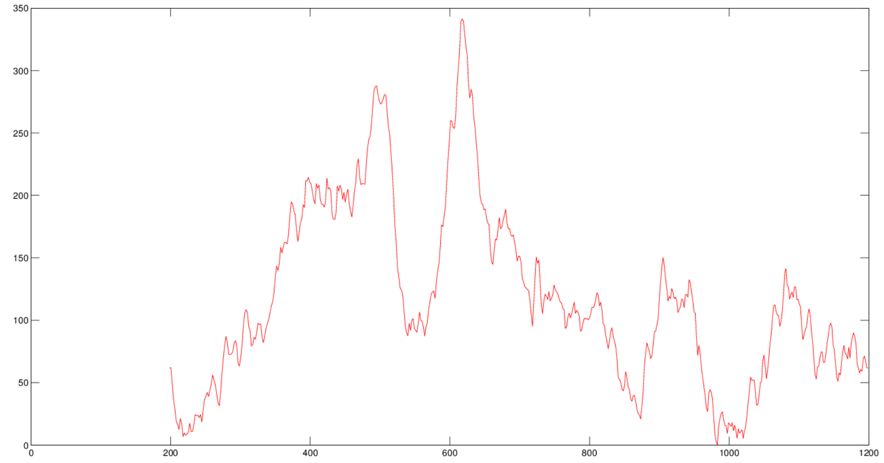

Figure B.15: Ru-ETS-10 Raman Results

APPENDIX C

APPLICATION RESULTS:SUPPORTING INFORMATION

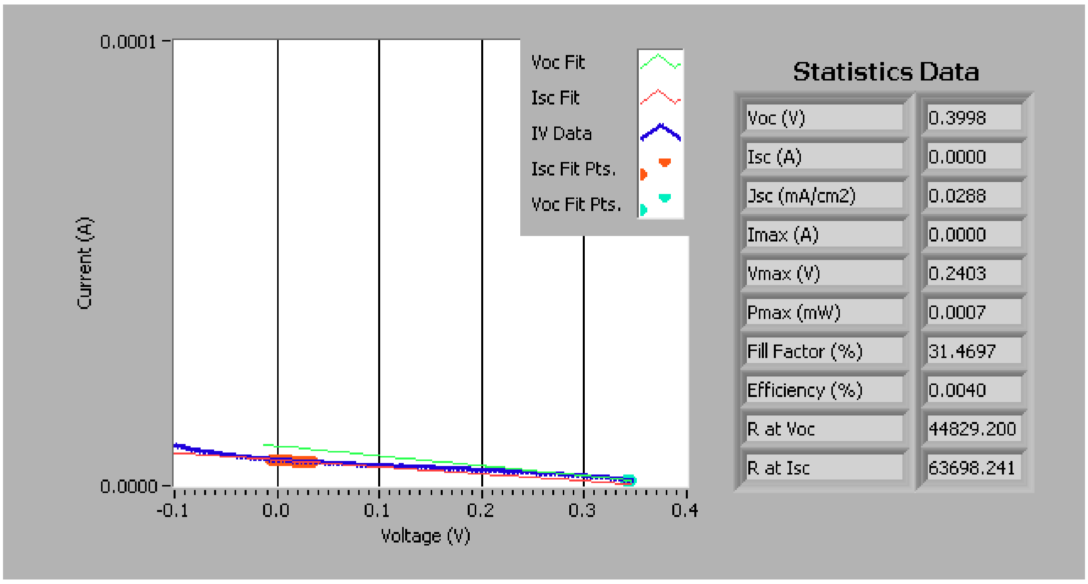

Statistics Data

Voc (V)	0.3998
Isc (A)	0.0000
Jsc (mA/cm2)	0.0288
Imax (A)	0.0000
Vmax (V)	0.2403
Pmax (mW)	0.0007
Fill Factor (%)	31.4697
Efficiency (%)	0.0040
R at Voc	44829.200
R at Isc	63698.241

Figure C.1: First ETS-10 DSSC Solar Measurements

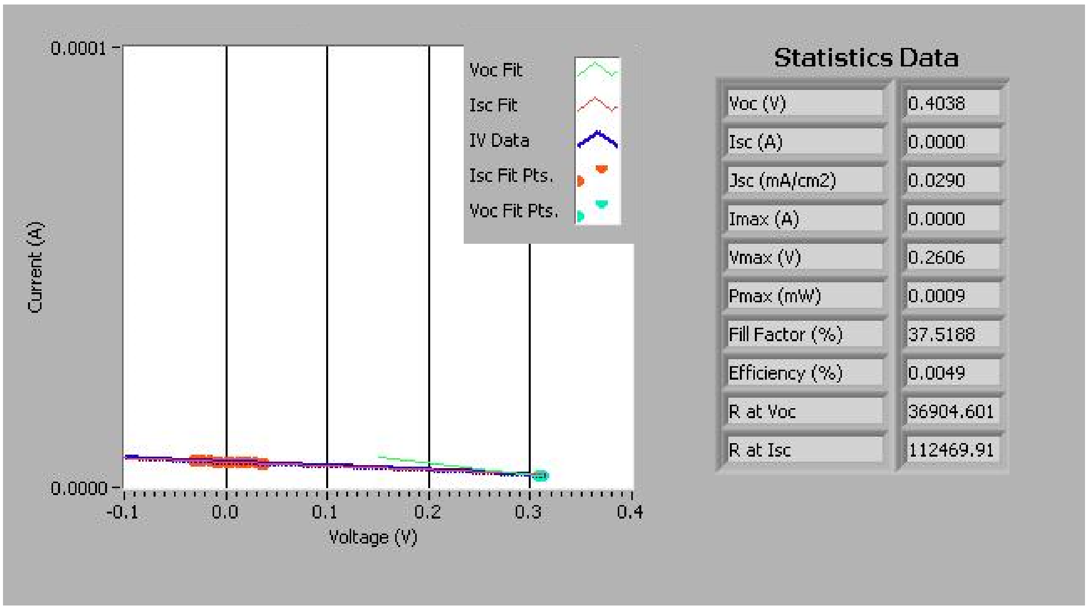

Statistics Data

Voc (V)	0.4038
Isc (A)	0.0000
Jsc (mA/cm2)	0.0290
Imax (A)	0.0000
Vmax (V)	0.2606
Pmax (mW)	0.0009
Fill Factor (%)	37.5188
Efficiency (%)	0.0049
R at Voc	36904.601
R at Isc	112469.91

Figure C.2: ETS-10 DSSC Cell Test

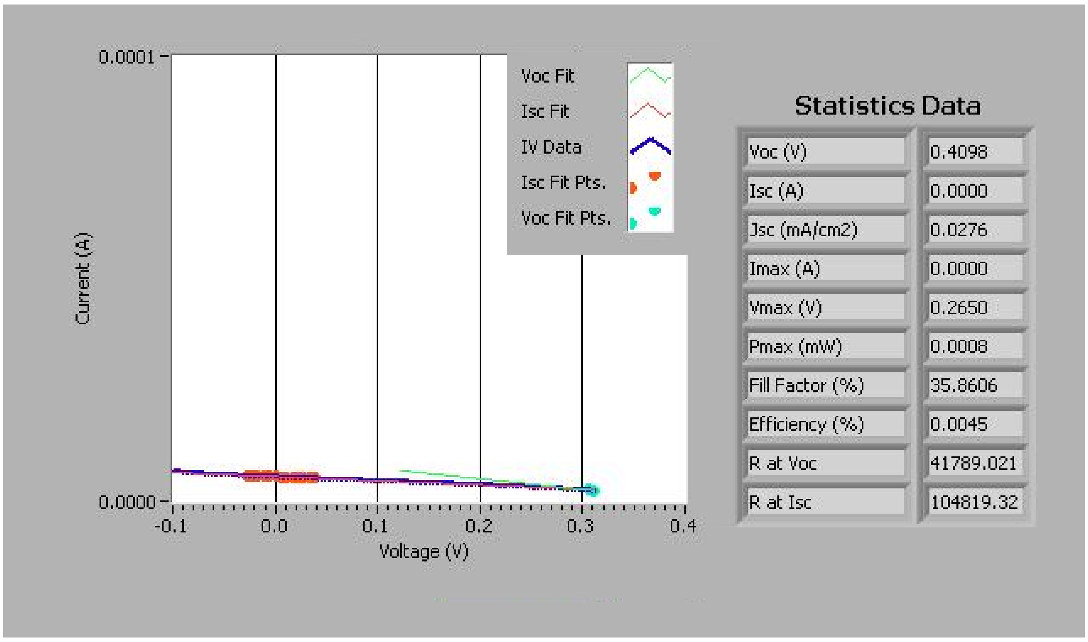

Statistics Data

Voc (V)	0.4098
Isc (A)	0.0000
Jsc (mA/cm2)	0.0276
Imax (A)	0.0000
Vmax (V)	0.2650
Pmax (mW)	0.0008
Fill Factor (%)	35.8606
Efficiency (%)	0.0045
R at Voc	41789.021
R at Isc	104819.32

Figure C.3: ETS-10 DSSC Cell Test reverse biased

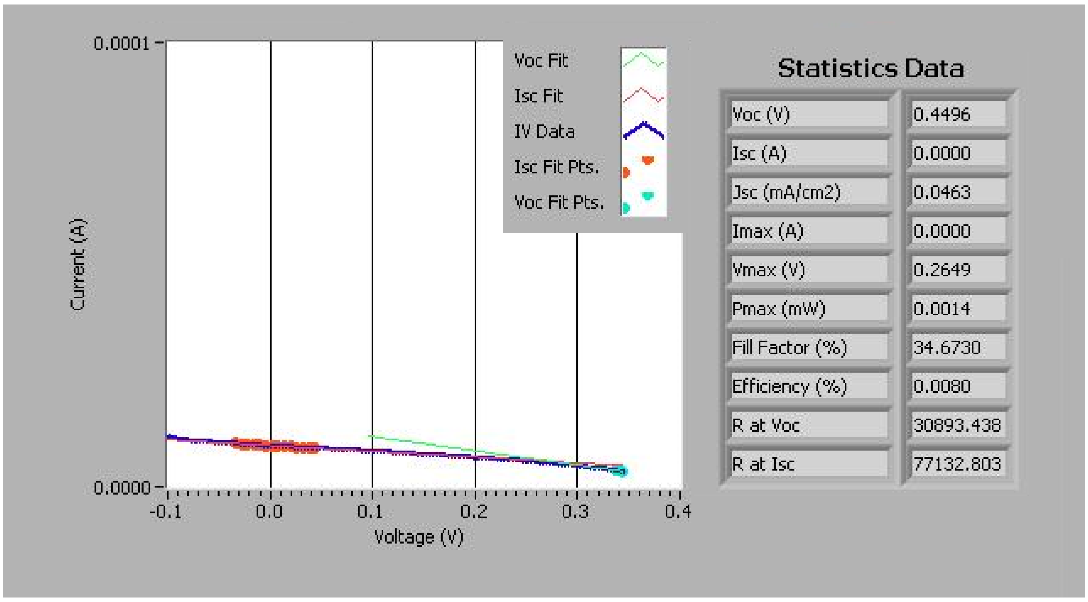

Statistics Data

Voc (V)	0.4496
Isc (A)	0.0000
Jsc (mA/cm2)	0.0463
Imax (A)	0.0000
Vmax (V)	0.2649
Pmax (mW)	0.0014
Fill Factor (%)	34.6730
Efficiency (%)	0.0080
R at Voc	30893.438
R at Isc	77132.803

Figure C.4: ETS-10 DSSC Cell Test reverse biased

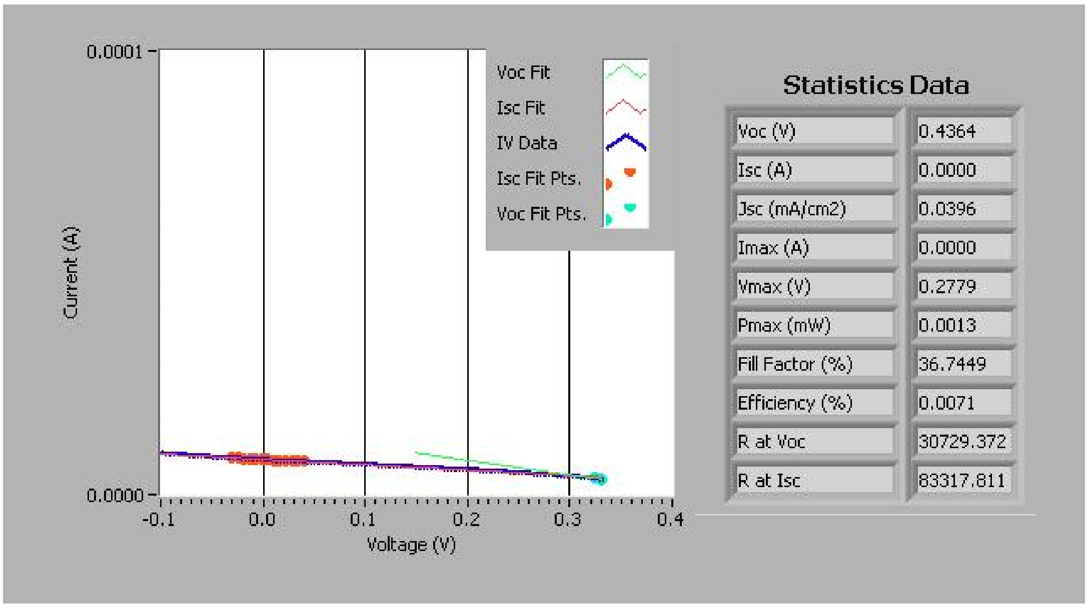

Statistics Data

Voc (V)	0.4364
Isc (A)	0.0000
Jsc (mA/cm2)	0.0396
Imax (A)	0.0000
Vmax (V)	0.2779
Pmax (mW)	0.0013
Fill Factor (%)	36.7449
Efficiency (%)	0.0071
R at Voc	30729.372
R at Isc	83317.811

Figure C.5: ETS-10 DSSC Cell Test

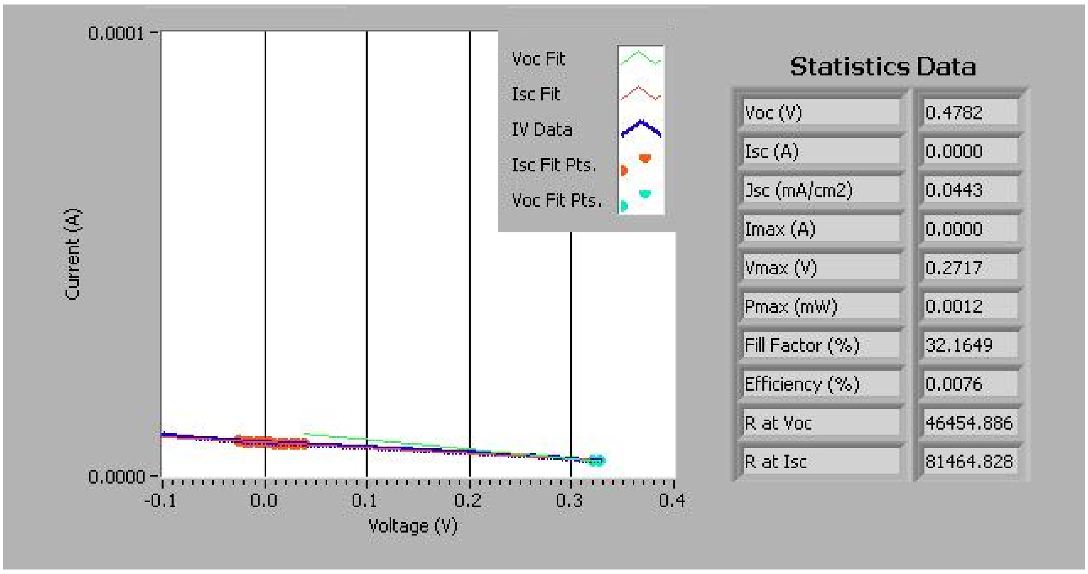

Statistics Data

Voc (V)	0.4782
Isc (A)	0.0000
Jsc (mA/cm2)	0.0443
Imax (A)	0.0000
Vmax (V)	0.2717
Pmax (mW)	0.0012
Fill Factor (%)	32.1649
Efficiency (%)	0.0076
R at Voc	46454.886
R at Isc	81464.828

Figure C.6: ETS-10 DSSC Cell Test reverse biased

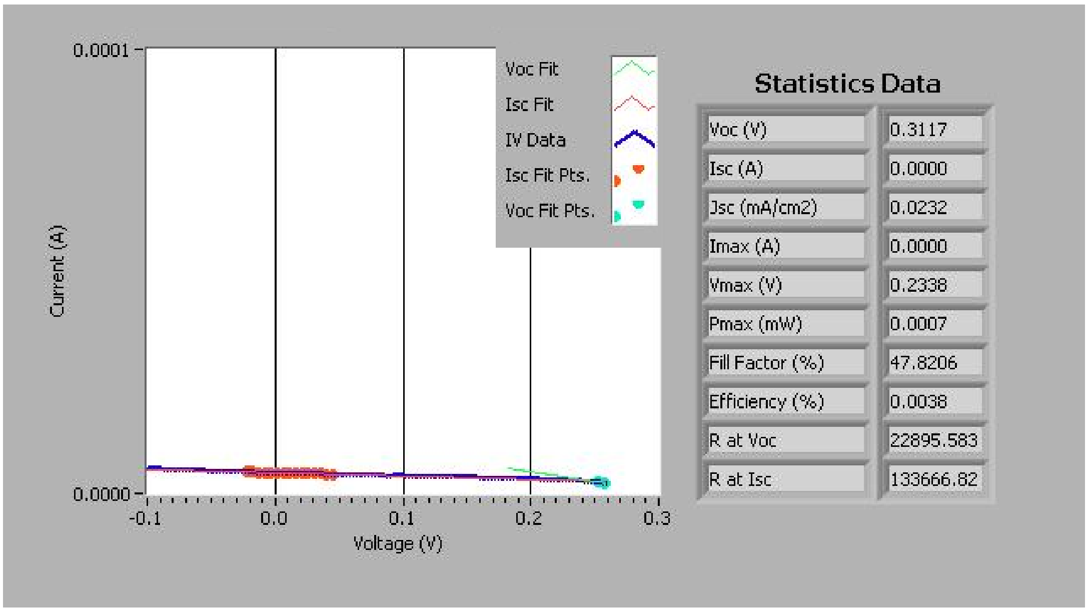

Statistics Data

Voc (V)	0.3117
Isc (A)	0.0000
Jsc (mA/cm2)	0.0232
Imax (A)	0.0000
Vmax (V)	0.2338
Pmax (mW)	0.0007
Fill Factor (%)	47.8206
Efficiency (%)	0.0038
R at Voc	22895.583
R at Isc	133666.82

Figure C.7: Ag^+-ETS-10 DSSC Cell Test

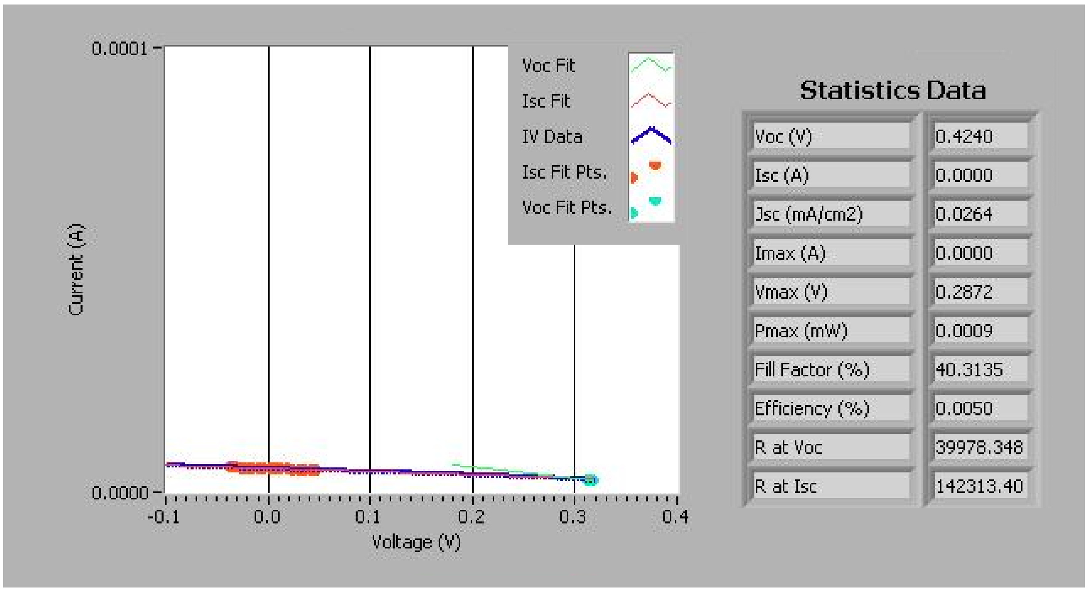

Voc (V)	0.4240
Isc (A)	0.0000
Jsc (mA/cm2)	0.0264
Imax (A)	0.0000
Vmax (V)	0.2872
Pmax (mW)	0.0009
Fill Factor (%)	40.3135
Efficiency (%)	0.0050
R at Voc	39978.348
R at Isc	142313.40

Figure C.8: Ag^{+}-ETS-10 DSSC Cell Test

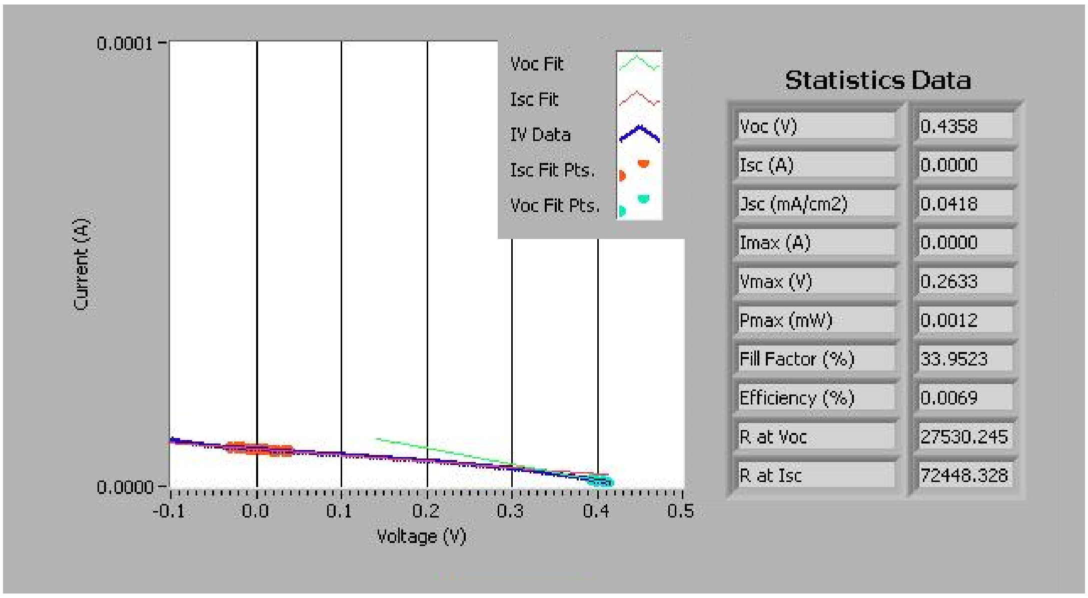

Voc (V)	0.4358
Isc (A)	0.0000
Jsc (mA/cm2)	0.0418
Imax (A)	0.0000
Vmax (V)	0.2633
Pmax (mW)	0.0012
Fill Factor (%)	33.9523
Efficiency (%)	0.0069
R at Voc	27530.245
R at Isc	72448.328

Figure C.9: Silver Nanoparticle-ETS-10 DSSC Cell Test Reverse Biased

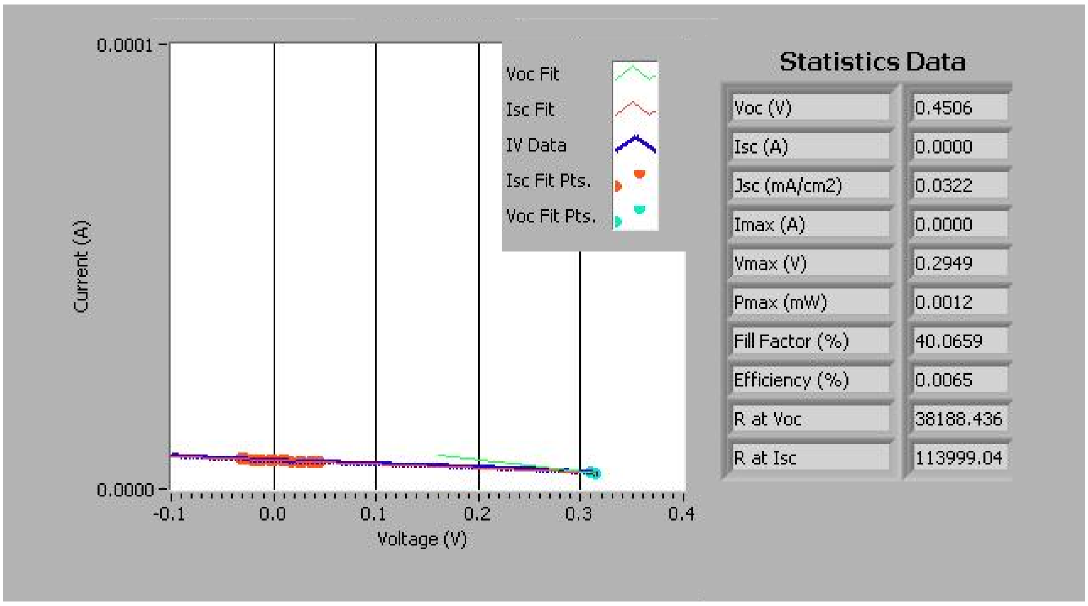

Statistics Data

Voc (V)	0.4506
Isc (A)	0.0000
Jsc (mA/cm2)	0.0322
Imax (A)	0.0000
Vmax (V)	0.2949
Pmax (mW)	0.0012
Fill Factor (%)	40.0659
Efficiency (%)	0.0065
R at Voc	38188.436
R at Isc	113999.04

Figure C.10: Silver Nanoparticle-ETS-10 DSSC Cell Test

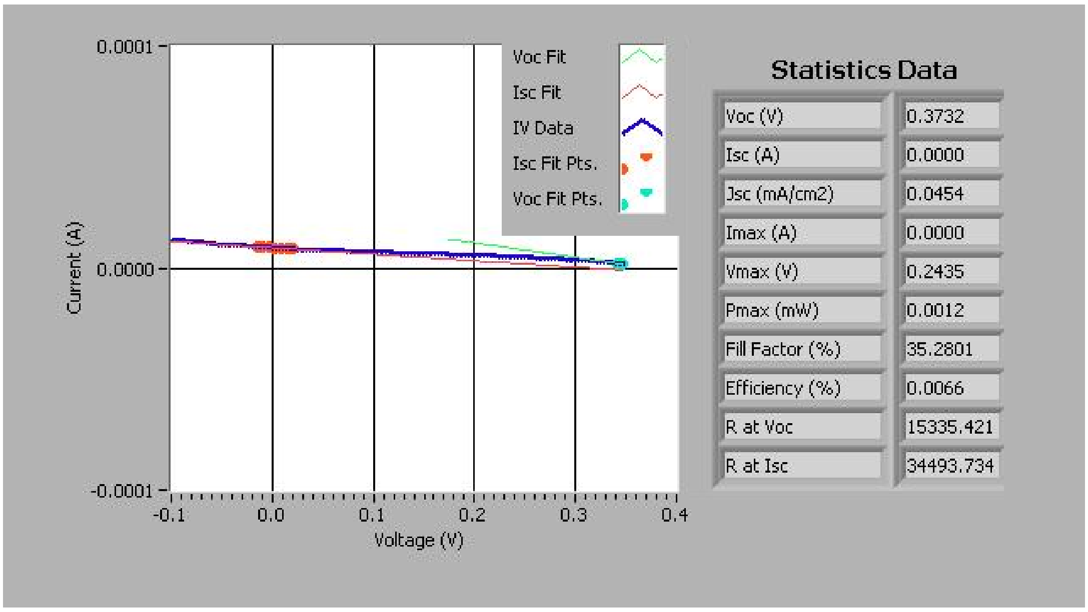

Statistics Data

Voc (V)	0.3732
Isc (A)	0.0000
Jsc (mA/cm2)	0.0454
Imax (A)	0.0000
Vmax (V)	0.2435
Pmax (mW)	0.0012
Fill Factor (%)	35.2801
Efficiency (%)	0.0066
R at Voc	15335.421
R at Isc	34493.734

Figure C.11: Silver Nanoparticle-ETS-10 DSSC Cell Test

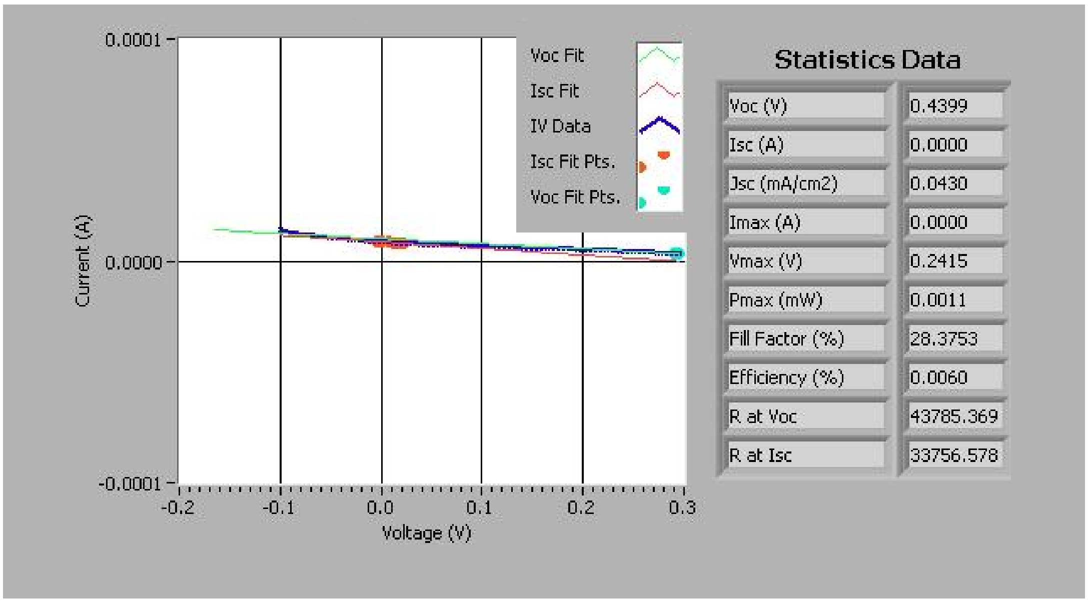

Statistics Data

Voc (V)	0.4399
Isc (A)	0.0000
Jsc (mA/cm2)	0.0430
Imax (A)	0.0000
Vmax (V)	0.2415
Pmax (mW)	0.0011
Fill Factor (%)	28.3753
Efficiency (%)	0.0060
R at Voc	43785.369
R at Isc	33756.578

Figure C.12: Silver Nanoparticle-ETS-10 DSSC Cell Test Reverse Biased